

Universidad de Málaga

Escuela Técnica Superior de Ingeniería de Telecomunicación



TESIS DOCTORAL

THE COMPLEMENTARY STRIP-SLOT: ANALYSIS AND ANTENNA APPLICATIONS

Autor:

ELENA ABDO SÁNCHEZ

Directores:

TERESA MARÍA MARTÍN GUERRERO

CARLOS CAMACHO PEÑALOSA



Publicaciones y
Divulgación Científica

AUTOR: Elena Abdo Sánchez

EDITA: Publicaciones y Divulgación Científica. Universidad de Málaga



Esta obra está sujeta a una licencia Creative Commons:

Reconocimiento - No comercial - SinObraDerivada (cc-by-nc-nd):

[Http://creativecommons.org/licenses/by-nc-nd/3.0/es](http://creativecommons.org/licenses/by-nc-nd/3.0/es)

Cualquier parte de esta obra se puede reproducir sin autorización
pero con el reconocimiento y atribución de los autores.

No se puede hacer uso comercial de la obra y no se puede alterar, transformar o hacer
obras derivadas.

Esta Tesis Doctoral está depositada en el Repositorio Institucional de la Universidad de
Málaga (RIUMA): riuma.uma.es

Abstract

In this Ph.D. thesis, a novel radiating element, the so-called *complementary strip-slot*, has been proposed for avoiding the intrinsic resonant nature of the microstrip-fed slot. The all-pass behaviour of the structure is explained through electromagnetic analysis, and an equivalent circuit is proposed, which is capable not only of explaining its properties but also of offering the required analytical tools to state the design methodology. After a comprehensive study of the element behaviour, its potential for building series-fed arrays with novel functionalities is explored through different antenna configurations: linear travelling-wave, log-periodic and sequentially rotated arrays. It is highlighted that the broad impedance matching of the proposed element brings about an enhancement in performance in the arrays with respect to those based on its narrow-band counterpart. Thus, since this thesis provides a solution for the narrow impedance bandwidth of microstrip radiators, it broadens the horizon of the antennas in this technology to non-resonant elements.

CONTENTS

1	Introduction	1
1.1	Contextual Framework	1
1.2	Genesis	3
1.3	Objectives	5
1.4	Thesis Outline and Contributions	5
2	The Complementary Strip-Slot Element	9
2.1	Geometry Description	11
2.2	Analysis	11
2.2.1	Even-Odd Mode Analysis	12
2.2.2	Equivalent Circuit	15
2.2.3	Radiation	18
2.3	Design for Broad Matching	20
2.4	Results	21
2.4.1	Prototypes	22
2.4.2	Results as Circuit Element	23
2.4.3	Results as Radiation Element	27
2.5	Parametric Study	31
2.6	Conclusion	38
3	Strip-Slot-Based Linear Travelling-Wave Arrays	41
3.1	Full-Space Frequency-Scanning Array	42
3.1.1	Theory Review	43
3.1.2	Linear Array Based on the Strip-Slot Element	44

3.1.3	The Broadside Issue	48
3.2	Electronically Reconfigurable Array	58
3.2.1	Geometry	60
3.2.2	Design Guidelines	61
3.2.3	Design Proposal	65
3.2.4	Results and Discussion	68
3.3	Conclusions	73
4	Strip-Slot-Based Log-Periodic Array	75
4.1	Motivation	75
4.2	Brief Review on Classic Log-Periodic Arrays	77
4.3	Design of the Proposed Log-Periodic Array	78
4.4	Results and Analysis	81
4.5	Radiation Computation Using the Equivalent Circuit	85
4.6	Back-Radiation Reduction	89
4.7	Conclusions	90
5	Strip-Slot-Based Sequentially Rotated Array	93
5.1	Motivation	93
5.2	Multiband Array with Polarisation Agility	96
5.2.1	Design	96
5.2.2	Modes of Operation	97
5.3	Proof of Concept	99
5.3.1	Results	100
5.3.2	Experimental Demonstration	105
5.4	Application: A GNSS Self-Diplexing Dual-Band Antenna	109
5.5	Conclusions	113
6	Conclusions and Outlook	115

6.1	Summary and Conclusions	115
6.2	Original Contributions	117
6.3	Future Work	118
Appendix A Artificial Transmission Lines Based on the Strip-Slot		121
Appendix B Lattice Networks		125
B.1	Basic Properties	125
B.2	Power Dissipation	126
Appendix C Advantages of the Modelling With Lattice Networks		129
C.1	Introduction	129
C.2	Realizability Evaluation	130
C.2.1	Dumbbell-Shaped DGS	131
C.2.2	Microstrip Stepped-Impedance Hairpin Resonator	132
C.3	Use of the Image Impedance	133
C.4	Conclusions	134
Appendix D Floquet's Theorem and Spatial Harmonic Expansion		137
Appendix E Publications Derived From This Thesis		139
Appendix F Summary in Spanish		143
F.1	Introducción	143
F.1.1	Marco contextual	143
F.1.2	Génesis	144
F.1.3	Objetivos	145
F.1.4	Estructura de los contenidos	146
F.2	El elemento strip-slot complementario	147
F.3	Arrays de onda progresiva lineales basados en el elemento strip-slot	149
F.4	Array log-periódico basado en el elemento strip-slot	151

F.5	Array rotado secuencialmente basado en el elemento strip-slot	152
F.6	Conclusiones y líneas futuras	154
F.6.1	Contribuciones originales	154
F.6.2	Líneas futuras	156

Bibliography		159
---------------------	--	------------

LIST OF FIGURES

2.1	Geometry of the structure.	11
2.2	Electric field distributions for the modes of the microstrip-slotline coupling section.	12
2.3	Even- and odd-mode excitations. Relation of Z_M and Z_S with the impedances of the modes.	13
2.4	Coupled subsection.	14
2.5	Equivalent configuration of a pair of coupled lines of Fig. 2.4.	14
2.6	General symmetrical lattice network.	15
2.7	Equivalent circuit for the coupled subsection of Fig. 2.4.	16
2.8	Equivalent circuit comparison for a strip, a slot and the proposed structure.	17
2.9	Equivalent currents along the elements at the resonance frequency of the slot.	19
2.10	Manufactured structure on RO4350B (Prototype 1).	22
2.11	Manufactured structure on GIL 1032 (Prototype 2).	23
2.12	Characteristic impedances and effective permittivities of the modes for Prototype 1.	23
2.13	Lattice impedances extracted from the measured and simulated structure and those from the equivalent circuit for Prototype 1.	25
2.14	Return loss comparison between the manufactured structure and the simulated microstrip-fed slot for Prototype 1.	26
2.15	Resulting image impedance of the manufactured structure (measurement and simulation) for Prototype 1.	26
2.16	Characteristic impedances and effective permittivities of the modes for Prototype 2.	27

2.17	Lattice impedances extracted from the measured and simulated structure and those from the equivalent circuit for Prototype 2.	28
2.18	Return loss comparison between the manufactured structure and the simulated microstrip-fed slot for Prototype 2.	29
2.19	Resulting image impedance of the manufactured structure (measurement and simulation) for Prototype 2.	29
2.20	Comparison of the ratio between the radiated power and the available power in %, computed with the equivalent lattice circuit and by electromagnetic simulation of the isolated elements and the complementary strip-slot (Prototype 2).	30
2.21	Comparison of the ratio between the dissipated power in the load and the available power in % in the complementary strip-slot and in the conventional microstrip-fed slot (Prototype 2).	31
2.22	Normalized radiation patterns comparison for the simulated and measured structure and the simulated slot without the strip in the zx -plane.	32
2.23	Simulated radiation efficiency (Prototype 2).	33
2.24	Characteristic impedances and effective permittivities of the even and odd modes of the coupled section at 5.4 GHz.	34
2.25	Isolines of the image impedance of the coupled section at 5.4 GHz.	35
2.26	Isolines of the return loss of the coupled section at 5.4 GHz.	35
2.27	Isolines of the coupling coefficient k of the coupled section at 5.4 GHz.	36
2.28	Comparison of the return loss for the four designs of Table 2.1.	37
2.29	Comparison of the real part of the image impedance for the four designs of Table 2.1.	37
2.30	Comparison of the phase response for the four designs of Table 2.1.	38
2.31	Comparison of the simulated radiation efficiency of the four designs of Table 2.1.	39
3.1	Photographs of the manufactured travelling-wave array.	45
3.2	Phase constants of the spatial harmonics multiplied for the analysed five-cells structure.	46

3.3	Main beam angle for the analysed five-element array according to (3.2).	46
3.4	Radiation efficiency versus frequency for the analysed five-element array.	47
3.5	Comparison of the $ S_{11} $ of the proposed travelling-wave array between measurement and simulation (with HFSS and ANSYS Designer).	47
3.6	Measured and simulated radiation patterns of the travelling-wave array at different frequencies over the first radiation band.	49
3.7	Measured and simulated radiation patterns of the travelling-wave array at different frequencies over the second radiation band.	50
3.8	Measured maximum gain of the travelling-wave array over the two radiation bands.	51
3.9	Image impedance of the resulting section of a resistive symmetrical lattice network with Z_{im}' with a transmission line section at each port. The total propagation factor is βp .	53
3.10	Comparison of the reflection coefficient for an infinite periodic array with strip-slots for two different pitch values.	54
3.11	Layout of the array with single stub matching network.	55
3.12	Comparison of the simulated $ S_{11} $ between the original array and the array with matching network.	55
3.13	Layouts of the aligned and misaligned strip-slot elements.	56
3.14	Comparison of the simulated $ S_{11} $ of the radiating element with different misalignments.	56
3.15	Comparison of the measured $ S_{11} $ between the aligned and the misaligned strip-slot array.	57
3.16	Comparison of the $ S_{11} $ between measurement and simulations for the misaligned strip-slot array.	57
3.17	Comparison of the simulated radiation efficiency between the aligned and the misaligned strip-slot array.	58
3.18	Schematic of the antenna and the used coordinate system.	60
3.19	Phase shifter unit-cell.	61

3.20	(a) An example of ϕ_t as a function of frequency and varactor capacitance for two phase shifters with different number of cells. (b) θ as a function of frequency and reverse bias voltage for the five frequencies marked in figure (a).	64
3.21	$ S_{11} $ of the radiating element obtained from electromagnetic simulation.	66
3.22	Intrinsic phase shift introduced by the element (without considering the phase of the feed microstrip line), obtained from electromagnetic simulation.	66
3.23	Manufactured antenna.	67
3.24	Main pointing direction, θ , versus the reverse bias voltage.	68
3.25	$ S_{11} $ obtained from the simulation and measurement of the designed array for $V_R = 0.1$ V and $V_R = 3.6$ V.	69
3.26	Normalized simulated and measured radiation patterns obtained when some V_R are applied as the reverse bias voltage for different frequencies: 1.71 GHz, 1.9 GHz and 2.17 GHz, in order to maintain the main beam direction to -30°	70
3.27	Measured normalized radiation patterns in linear scale at 2 GHz for some values of V_R	72
3.28	Normalized simulated radiation patterns in linear scale obtained for the same case as Fig. 3.26 with a reflector plane over the microstrip layer.	73
4.1	Schematic diagram of a log-periodic array.	77
4.2	Layout of the proposed log-periodic array.	81
4.3	Photographs of the manufactured log-periodic array.	81
4.4	$VSWR$ comparison between simulation and measurement.	82
4.5	Magnitude of the voltage drop across the slots at different frequencies.	83
4.6	Measured and simulated radiation patterns of the log-periodic array at different frequencies.	84
4.7	Peak gain comparison between simulation and measurement.	85
4.8	Simulated radiation efficiency of the log-periodic array.	85
4.9	Lattice equivalent circuit of the element i	86

4.10	Phase and magnitude of the voltage drop across the slots of the elements 1, 7 and 15 over frequency.	88
4.11	Computed radiation patterns of the log-periodic array.	89
4.12	Fotography of the proposed log-periodic array with the reflector plane.	90
4.13	Simulated and measured radiation patterns of the proposed array with the reflector plane for different frequencies.	90
5.1	Configuration of the proposed ring array.	96
5.2	Required radius of the proposed ring array for CP at each frequency, in accordance with (5.1). The chosen radius of 12 mm is marked, together with the resulting frequencies of operation.	99
5.3	Layout of a manufactured antenna.	100
5.4	Simulated and measured $ S_{11} $ of the ring array of Fig. 5.3.	101
5.5	Measured and simulated axial ratio at broadside of the ring array of Fig. 5.3 over the three studied frequency bands.	102
5.6	Measured and simulated polarisation ratio for single excitation over the three studied frequency bands.	102
5.7	Measured and simulated radiation patterns in dB at the three studied frequency bands for single excitation in a constant-azimuth plane.	103
5.8	Measurement setup for LP.	104
5.9	Measured polarisation ratio over the three studied frequency bands at broadside and $\phi = 90^\circ$ for dual in-phase excitation.	105
5.10	Measured and simulated radiation patterns in dB over the three studied frequency bands for dual in-phase excitation at a constant-azimuth plane ($\phi = 90^\circ$).	106
5.11	Simulated radiation efficiency over the three studied frequency bands.	107
5.12	Measurement setup.	107
5.13	Transmission coefficients, when two identical proposed antennas are inserted in the setup of Fig. 5.12. P1 and P4 are the same port in the two different antennas, as well as P3 and P2.	108

5.14	Transmission coefficients between the horn antenna and the proposed ring antenna when the two ports P2 and P4 of the ring antenna are combined in-phase (common mode), in anti-phase (differential mode) and not combined (signal at P2 when P4 is terminated by a matched load).	109
5.15	Transmission coefficients between the horn antenna and the proposed ring antenna rotated 90° with respect to Fig. 5.14, when the two ports P2 and P4 of the ring antenna are combined in-phase (common mode), in anti-phase (differential mode) and not combined (signal at P2 when P4 is terminated by a matched load).	110
5.16	Photograph of the manufactured antenna.	111
5.17	$ S_{11} $ comparison between measurement and simulation.	111
5.18	Axial ratio comparison between measurement and simulation at broad-side for the two design bands.	112
5.19	Simulated and measured radiation patterns ($\phi = 0$).	112
A.1	Geometry of the unit-cells under comparison. (a) corresponds to the unit-cell with alternate elements and (b) to the complementary strip-slot.	122
A.2	S-Parameters comparison between the alternate and superimposed strip-slot unit-cells.	123
A.3	Phase factor comparison between the alternate and superimposed strip-slot unit-cells.	123
A.4	S-Parameters comparison between a three-cells structure built with the alternate and the superimposed strip-slot unit-cells.	124
B.1	General symmetrical lattice network.	125
B.2	Terminated symmetrical lattice network.	126
C.1	Network topologies: (a) Lattice section, (b) T-section and (c) II-section.	130
C.2	Layout of the dumbbell-shaped DGS.	131
C.3	Real part of the parallel admittance of the T- and lattice topologies for the dumbbell DGS.	132
C.4	Layout of the microstrip stepped-impedance hairpin resonator.	132

C.5	Series impedance of the Π - and lattice topologies for the hairpin resonator.	133
C.6	Parallel admittances of the T- and lattice topologies for the hairpin resonator.	133
C.7	Magnitude of the lattice image impedance for the dumbbell DGS and the hairpin resonator.	134

Chapter 1: Introduction

The goal of this introductory chapter is to present the topic of this dissertation, firstly by showing the contextual framework in which this work can be included. Next, both the origin and the motivation that have led to the development of this research are explained, paving the way to a subsequent description of the objectives to be reached. Finally, an overview of the structure of the contents is provided, together with an allusion to what can be regarded as the original contributions of this thesis.

1.1 CONTEXTUAL FRAMEWORK

It is indubitable that, in recent years, the world has experienced countless changes that have modified our way of life as well as the means of communication. To a large extent, these improvements have been possible thanks to the rapid development of new communication technologies, especially “wireless”. In spite of the remarkable progress achieved in this area, some challenges still remain unsolved, requiring the effort of the research community as regards the emerging wide bandwidth applications (e.g., medical imaging or wireless communications).

Specifically, the design of the antenna in communication systems is one of the most classic challenges in telecommunication engineering; however, it still requires the attention of researchers since the recently-appeared new services demand the search for novel functionalities, wide bandwidth, high efficiency and directivity, and easy manufacture.

Planar antennas have become one of the most used and studied radiators in recent decades and the best candidates for the new communication services because of their many advantages such as light weight, low cost and profile, compatibility with integrated circuitry, small size and low manufacturing cost. However, the success of these

antennas has been limited by a serious disadvantage, the narrow impedance bandwidth, which restricts their possible applications. Due to the resonant nature of the microstrip-fed slot and patch, the impedance bandwidth of these antennas is insufficient for most current services in communications. Its improvement implies a task that many researchers have tackled and yet have not been solved once and for all. The most successful techniques for improving the impedance bandwidth of microstrip radiators have been the use of impedance matching networks and the introduction of multiple resonators [1, 2]. Both broadening methods have drawbacks, since either the surface area is increased, making it unsuitable as an array element, or stacked structures have to be used, leading to greater costs, complexity and size. Enhancing the impedance bandwidth without any complexity or size cost is an important field of current research in planar antennas.

Another limitation of microstrip antennas is the radiation efficiency, which is low compared to other antennas. This limitation can be overcome through an array topology. The series feeding configuration is a possible solution to excite the array. This type of array has the benefit of simplicity as well as less space on the substrate, lower attenuation losses and lower spurious radiation from the feed lines, compared to corporate feeding. Moreover, if the array is configured as a travelling-wave, the possibility of steering the beam away from the broadside arises as a very interesting characteristic for applications like radar or beamforming in mobile communications. In fact, the appearance of “Composite Right-Left Handed” (CRLH) artificial transmission lines (TLs) in microwave technology found an important application in the design of travelling-wave antennas and has revived interest in them. An artificial TL is a periodic structure, built as the spatial repetition of a unit-cell that synthesizes the characteristics of a TL. The CRLH TLs are inspired by the so-called “Double negative metamaterials” [3] and allow the emulation of some of the properties of these materials, such as backward propagation, with no need for the actual existence of these materials [4].

The different behaviour of the CRLH TLs with respect to the conventional ones has allowed circuit and antenna functionalities to be enhanced in the microwave range. Specifically, the main design parameter is the dispersion diagram achieved with this kind of structure, which results in circuits designed under the “dispersion engineering” concepts. This term refers to the possibility of designing the dispersion diagram of TLs, or simply the phase response, by periodically loading a conventional TL with L and C elements. It has allowed the rediscovery of old circuit and antenna topologies from the point of view of the dispersion diagram, finding novel applications and features. The

review of old topologies with new eyes also included Leaky-Wave Antennas (LWAs), which have been provided with improved frequency-scanning capabilities using these novel concepts [5].

The dispersion relation of an artificial TL can be derived from the phase response of its unit-cell. Therefore, the main challenge in building an artificial TL is to find the unit-cell that is appropriate for the requirements. Consequently the search for novel unit-cells that allow the implementation of planar antennas (specifically, travelling-wave arrays) with a novel or enhanced performance, bearing in mind the requirements of the new emerging services (e.g., wide bandwidth), seems to be an attractive topic for the antenna community. New functionalities can be discovered by fusing the novel concepts of artificial TLs with classic antennas.

1.2 GENESIS

The core of this Ph.D. thesis emerged while searching for a unit-cell to synthesize artificial TLs in planar technology. The idea behind it was to insert elements in the microstrip line to add some capacitance in the series branch and some inductance in the shunt branch in the microstrip incremental equivalent circuit, in order to get multiband right-handed (RH)/left-handed (LH) behaviour in the dispersion diagram of the resulting effectively homogeneous TL [4]. For the required capacitance, defected ground structures (DGSs) appeared as a good solution, since they are slots on the ground plane of the microstrip line and consequently behave as a series impedance. Open-ended stubs were chosen for the parallel branch since they can be modelled as a shunt admittance. Because both are distributed components, they behave as the desired capacitance and inductance at certain frequency bands, at which LH behaviour would be obtained.

The expected behaviour was achieved by loading the microstrip line with alternate DGSs and stubs: RH and LH bands were obtained in the dispersion diagram. However, due to the resulting incremental ladder network equivalent circuit, it led to the appearance of unavoidable stop-bands in the frequency response of the unit-cell.

At this point, a question came up about how close the stubs and the DGSs should be for optimum behaviour. As a first step, electromagnetic simulations varying the distance between the stub and the slot were carried out. Surprisingly, it was discovered that as the elements got closer, the mismatching bands decreased and an extraordin-

arily wide matching was obtained when the elements were completely superimposed. This noteworthy phenomenon did not have an immediate explanation and sparked our interest.

In the world of artificial transmission lines, the resulting unit-cell with the stub and the slot superimposed was of great interest, since the avoidance of the open-stopbands had been an active field of study. As a matter of fact, in 2008 Bongard *et al.* proposed a CRLH unit-cell that did not suffer from these undesired mismatching bands [6, 7]. Instead of implementing a transmission line by reproducing the T-, Π - or ladder-network equivalent circuit, they used a lattice network. With this topology, all-pass behaviour could be achieved when properly designed. Then, the discovered structure could be a simpler alternative to the development of artificial transmission lines with broad matching. In fact, it was found afterwards that the lattice network came up as the natural equivalent circuit of the structure. Then, lattice-network-based artificial transmission lines could be built without the need for the physical implementation of the lattice. Nevertheless, the high radiation intrinsic to the structure under discussion made the idea of building transmission media less convenient and the research then focused on its application as a radiating element.

Motivated by the potential of such a radiating structure, deeper research was carried out with the simplest topology possible, a microstrip-fed rectangular slot with a rectangular stub superimposed on it. The purpose was to explain theoretically its all-pass behaviour and study its possibilities as an antenna element. As a result, this Ph.D. thesis deals with the analysis and applications of this element, what we have called *the complementary strip-slot*, since its broad matching lies in the complementarity between the strip and the slot. Although it emerged almost unexpectedly, its many appealing features encouraged and guided this work. It is implemented in microstrip technology, with a single substrate and no use of vias, thus entailing low cost and easy manufacture. Moreover, it is a radiating structure that overcomes the main problem of microstrip antennas: the narrow impedance bandwidth. In addition, its series feeding configuration and the non-linear phase response makes it really appropriate for the implementation of travelling-wave arrays.

1.3 OBJECTIVES

Since the complementary strip-slot was an unknown structure, the first goal was to analyse its behaviour deeply, providing a solid explanation based on electromagnetic theory and finding an equivalent circuit for its easy modelling. Both the circuit and radiation aspects of the structure had to be characterised. Based on this developed theory, a design methodology for broad matching had to be established.

Once the element was completely characterised, the aim was to explore different array configurations and take advantage of the special features of the basic element to create antennas with enhanced performances. Due to the element series feeding, we focused on travelling-wave arrays.

It is important to point out that a self-imposed requirement was to corroborate the conclusions extracted from theory and electromagnetic simulations with the manufacture of prototypes at each step of the research, in order to prove the concepts with the experimental verification of the designs.

The final object of this research work was to design antennas in planar technology with novel functionalities using the complementary strip-slot element and highlight the potential of this structure as a novel non-resonant microstrip radiator.

1.4 THESIS OUTLINE AND CONTRIBUTIONS

This section provides a brief explanation of the contents of each chapter and highlights the most outstanding contributions of the related work.

Chapter 2 starts with the description of the complementary strip-slot and includes a comprehensive analysis of the structure: the theoretical electromagnetic study, a proposal of its equivalent circuit and a design methodology for achieving broad impedance matching. After that, two different prototypes are designed and built. Moreover, a study of the influence of the geometric parameters of the structure in the performance is provided. The main contribution of this chapter is the structure proposal as a microstrip-fed slot with a non-resonant behaviour and the theoretical tools to understand why this simple element has such a distinctive characteristic. The contribution of the equivalent circuit, which provides an excellent physical insight and explains both its matching and radiation behaviour, is also remarkable.

Once the element is characterised, array applications are explored. Due to the

series feeding of the element, travelling-wave arrays are considered. Hence, **Chapter 3** contains the first and immediate array concept, built by loading the microstrip line with several equal strip-slot elements. With a simple prototype, the scanning capabilities predicted by both array theory and spatial harmonic expansion are verified. Full scanning from backward to forward (including broadside) angles is achieved. Afterwards, a more careful design is carried out in order to include phase-shifters between the elements thus providing the array with electronic beam steering control. Thanks to the broadly matched element, the versatility of steering or maintaining the beam over a wide frequency band can be carried out without the need to modify the radiating element geometry. This is an important contribution to the state-of-the-art proposals.

Following with the array concepts, **Chapter 4** deals with the idea of a log-periodic array based on the complementary strip-slot. The challenge here is to adapt the long-established design methodology in order to explore the concept of a log-periodic array based on a non-resonant element. Although these arrays were conceived to provide wide bandwidth with narrow-band elements, the extended concept with non-resonant elements allows certain variations in the design that can achieve wider bandwidths. A prototype was built to prove the concept. The rethinking of the classic design methodology for wideband elements can be considered a relevant contribution of this work.

Chapter 5 introduces another array structure, in this case, focussing on polarisation. The arrangement of the elements following the sequential rotation technique and the construction of the concept as a circular travelling-wave array with the complementary strip-slots leads to a two-port polarisation agile antenna. The main contribution here is precisely the combination of the series-fed two-port circular antenna with the wideband element, which allows both multiband behaviour and polarisation versatility with such a very simple passive array.

Finally, **Chapter 6** summarises the main results and stresses the most significant contributions derived from this thesis. It concludes with the proposal for guidelines to carry on with this work in the future.

It is worth mentioning that all the content chapters include a specific contextualization and a literature review of the antenna concept dealt with in this part of the dissertation. Since different antenna configurations have been analysed, it has been considered more appropriate to study the state of the art for each particular topology.

In addition, four appendices are included to complete the provided contents. Ap-

pendix A summarises the results when, initially, the complementary strip-slot element was used for building artificial transmission lines. Appendix B reviews the main features of lattice networks and extracts a relevant property on power dissipation independence that can be considered a remarkable contribution of this work. Appendix C also includes some outstanding results on the advantages of modelling symmetric TL discontinuities and components using lattice networks. Appendix D includes a brief description on the Floquet's theorem and the spacial harmonic expansion. The publications derived from this thesis are enumerated in Appendix E. Lastly, Appendix F contains a summary of the thesis in Spanish.

Chapter 2: The Complementary Strip-Slot Element

In spite of their appealing advantages, microstrip antennas present a narrow impedance bandwidth, which restricts their potential applications. Although the problem of impedance bandwidth enhancement for patch antennas has been extensively studied, not much attention has been paid to microstrip-fed slots and two different methods to improve their bandwidth have been proposed: the widening of the slot [8], so that the Q-factor decreases, and the use of multiple resonances [9, 10]. However, when slots are used in a series-fed array configuration, low radiation from each one is desirable and, then, it is expected that they are relatively narrow. In this case, only the use of multiple resonances would be applicable. Some proposals are based on introducing a quarter-wavelength resonator into the microstrip feed line [9] or producing one or more fictitious short points on a single radiating slot [10]. However, the achieved bandwidth hardly reaches 100 % and the feed microstrip line is not terminated by a matched load, which makes its use difficult in a series-fed array. For this reason, although series-fed microstrip slot arrays are employed for some applications [11, 12], the slot narrow bandwidth limits their use. A suitable broadband slot element can extend the applications of this kind of array, for example, to broader log-periodic arrays or multi-band frequency scanning applications.

This chapter is entirely focused on the study of a simple and inexpensive configuration of the microstrip-fed slot that exploits the characteristics of the microstrip-slotline coupling to provide a significantly wide impedance bandwidth (up to 16:1) in a series-fed configuration, appropriate for travelling-wave arrays. The bandwidth enhancement is a consequence of the use of a strip superimposed on the slot that, together with the slot, makes up an all-pass coupled-line topology. The use of an all-pass section as a broadband radiator was also proposed in [13], where the element consisted of a pair of

coupled microstrip lines connected at one end. However, due to the different frequency behaviour of the odd- and even-mode impedances, the bandwidth improvement was limited. The main advantage of the microstrip-slot design over the coupled-microstrip one in [13] is the ability to provide different physical lengths for the even and odd modes, which allows similar electrical lengths to be obtained for both modes, and thus overcome the dispersion problem. Moreover, unlike the structure in [13], the radiator here is a slot on the ground plane of the microstrip.

Coupled slots and strips appear in numerous devices as well as in many heuristic designs for broadband patches; however, there are not many applications that exploit the characteristics of this coupling. Although the problem of strip-slot coupling has been studied for long time [14], only few components (most of them couplers) have come about from it. The use of this coupling for matching a series-fed slot radiator has not been previously reported.

The contribution to the state of the art is therefore a promising technique to broadly match a microstrip-fed slot, with analytical tools to tackle the design, unlike most of the proposals in the literature that combine strips and slots in heuristic designs. Moreover, since the strip-coupled slot modifies the phase and impedance responses of the conventional slot, the structure modelling requires a more sophisticated equivalent circuit than a series impedance and, thus, a more complex but complete equivalent circuit is also provided.

This chapter is then structured as follows. First of all, in Section 2.1, the geometry of the proposed structure is described. A study based on even-odd mode analysis is presented in Section 2.2 to explain the matching capability of the structure. The result of this analysis allows the proposal of an equivalent circuit, which is based on a lattice network and used to provide an explanation of the radiation properties of the structure. Then, the design methodology for achieving broad impedance bandwidth is described in Sec. 2.3. What follows next is the presentation of two prototypes that have been manufactured following these design steps and the discussion of both circuit and radiation results in Sec. 2.4. A brief study of the effect of the structure dimensioning is stated in Sec. 2.5. Finally, 2.6 summarises the main features of the proposed element.

2.1 GEOMETRY DESCRIPTION

The so-called complementary strip-slot structure is detailed in Fig. 2.1. It is composed of a coupled strip-slot section fed by a microstrip line terminated by a matched load. The coupled section consists of a strip conductor and a symmetrically arranged slot etched on the ground plane. The structure presents two symmetry planes: a plane along the propagation axis over the feed microstrip line, which divides the structure into two equal coupled subsections, and another along the coupled section. In Fig. 2.1, w , w_M and w_S stand for the feed microstrip, strip and slot widths, respectively; l_S corresponds to the slot length measured from the symmetry plane to the slot edge and l_M represents the strip length measured from the microstrip edge to the strip edge. Each coupled subsection can be seen as a microstrip-slotline combination, where the slotline is terminated by a short circuit and the microstrip line is terminated by an open circuit. Therefore, the proposed element can also be regarded as a conventional microstrip-fed slot, but incorporating a strip superimposed on the slot. This structure has appealing features such as simplicity, single substrate and no need of vias, which results in low cost. Moreover, the series-fed configuration makes it especially suitable for travelling-wave arrays of series-fed slots.

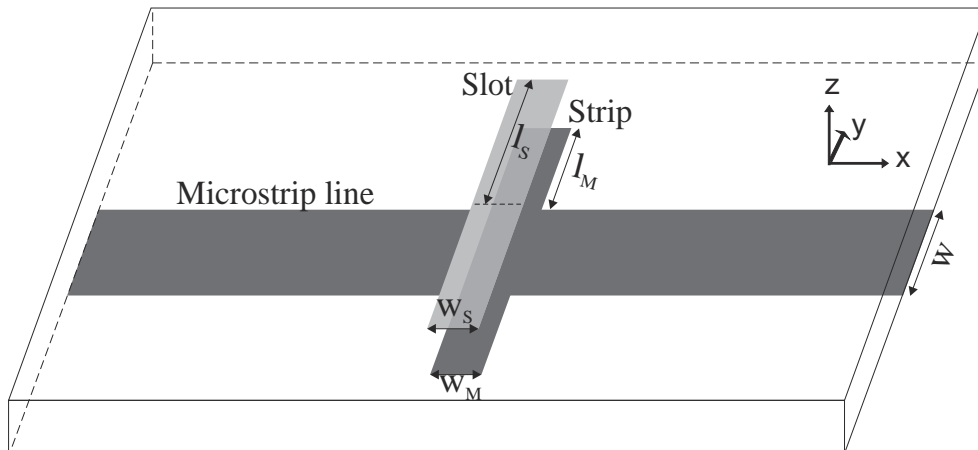


Figure 2.1: Geometry of the structure.

2.2 ANALYSIS

In this section, the structure is analysed from a theoretical point of view. Firstly, an electromagnetic analysis in terms of even and odd modes is carried out, providing a good explanation of the main behaviour characteristics of the element. Moreover,

this analysis allows the extraction of an equivalent circuit, based on a lattice network. Finally, the radiation of the element is studied based on both electromagnetic analysis and the equivalent circuit.

2.2.1 Even-Odd Mode Analysis

The coupled section can be considered as a three-conductor structure with common symmetry plane along the coupled section. Therefore, two quasi-TEM modes propagate in this structure: the even and odd modes. The electric field distribution for these modes is shown in Fig. 2.2 [15]. In the odd mode, the field is to a large extent concentrated in the gap and presents a distribution similar to that in a slotline; therefore, it can be referred to as quasi-slot mode. Likewise, the even mode has a field distribution similar to that of a microstrip line and is referred to as quasi-strip mode. Therefore, when the strip-slot coupling is not strong enough, the even mode is exclusively determined by the strip and the odd mode, by the slot.

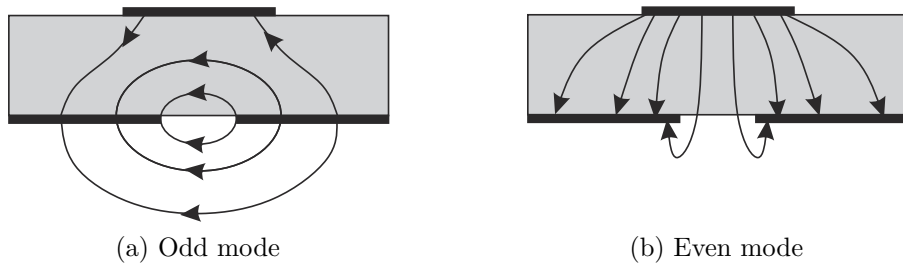


Figure 2.2: Electric field distributions for the modes of the microstrip-slotline coupling section.

Due to the similarity of the field patterns of the even and odd modes with those of the strip and the slot, the parameters defining the modes can be approximated by the following relations [15]:

$$Z_{0e} \approx 2Z_M; \quad \epsilon_{eff,e} \approx \epsilon_{eff,M} \quad (2.1a)$$

$$Z_{0o} \approx \frac{Z_S}{2}; \quad \epsilon_{eff,o} \approx \epsilon_{eff,S} \quad (2.1b)$$

where Z_{0e} and Z_{0o} are the characteristic impedances and θ_e and θ_o , the electrical lengths for the even and odd modes, respectively, and Z_M and Z_S stand for the characteristic impedances and $\epsilon_{eff,M}$ and $\epsilon_{eff,S}$ for the effective permittivities of such a microstrip line and a slotline, respectively. These relations are illustrated in Fig. 2.3. In the even

mode, the symmetry plane corresponds to a magnetic wall, since the electric field has even symmetry about the centre line and no current flows through it. The symmetry plane divides the structure into two identical transmission lines with characteristic impedance Z_{0e} and the same voltage excitation. In the odd mode, the electric field lines have an odd symmetry about the centre line, therefore the symmetry plane behaves as an electric wall and divides the structure into two transmission lines with characteristic impedance Z_{0o} and opposite terminal voltages. If low coupling is assumed, the resulting impedances under these two orthogonal excitations are the characteristic impedances of the microstrip and the slotline modes, Z_M and Z_S , respectively.

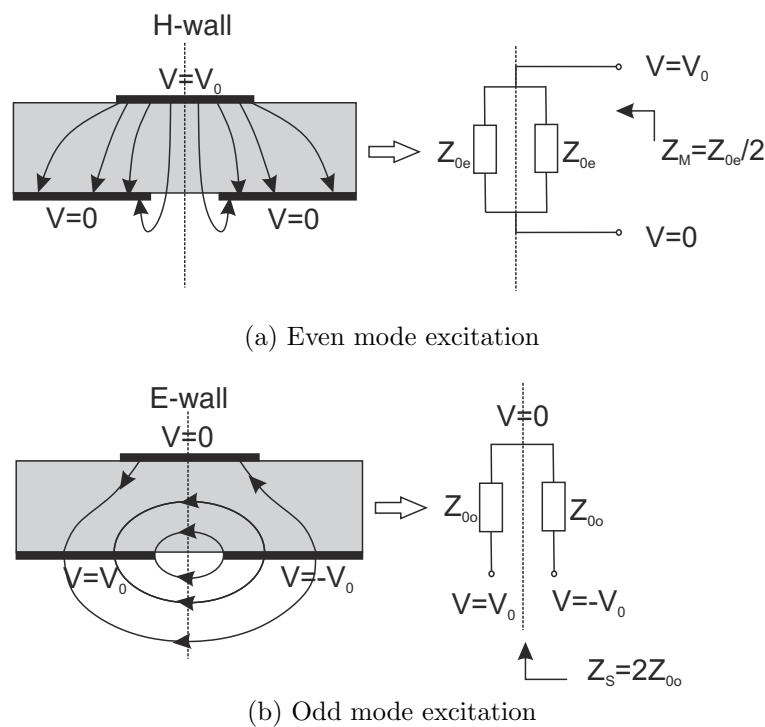


Figure 2.3: Even- and odd-mode excitations. Relation of Z_M and Z_S with the impedances of the modes.

In order to analyse the proposed strip-slot element, a coupling subsection is detailed in Fig. 2.4, where the four ports of the two-coupled-line structure are identified. In the proposed strip-slot configuration, the ports 1 and 2 are transversely fed by the microstrip line and the ports 3 and 4 are connected to each other. Therefore, this coupled subsection can be seen as a pair of coupled lines of the configuration shown in Fig. 2.5. On the one hand, under even excitation, $V_1 = V_2$ and $i_2 = 0$, hence a virtual open circuit is formed in the symmetry plane P_1 and the terminations at ports 3 and 4 act as open circuits for the even mode. On the other hand, $V_1 = -V_2$ under odd excitation, then the symmetry plane is a virtual short circuit and the terminations

at ports 3 and 4 are seen as short circuits by the odd mode. Therefore, the input impedances at ports 1 and 2 for the two modes are as follows:

$$Z_{in}^e = -jZ_{0e} \cot \theta_e \quad (2.2a)$$

$$Z_{in}^o = jZ_{0o} \tan \theta_o. \quad (2.2b)$$

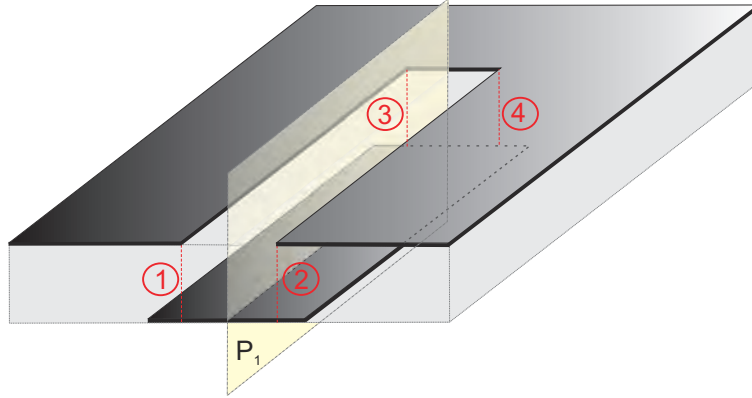


Figure 2.4: Coupled subsection.

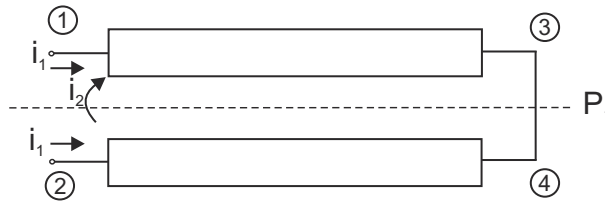


Figure 2.5: Equivalent configuration of a pair of coupled lines for the structure of Fig. 2.4.

The frequency behaviour of a coupled-line network of the topology shown in Fig. 2.5 was derived in [16]. The impedance matrix results in

$$[Z] = \begin{bmatrix} \frac{Z_{in}^e + Z_{in}^o}{2} & \frac{Z_{in}^e - Z_{in}^o}{2} \\ \frac{Z_{in}^e - Z_{in}^o}{2} & \frac{Z_{in}^e + Z_{in}^o}{2} \end{bmatrix} \quad (2.3)$$

and the image impedance,

$$Z_{im} = \sqrt{Z_e Z_o} = \sqrt{Z_{0e} Z_{0o} \cot \theta_e \tan \theta_o}. \quad (2.4)$$

It is evident that when the electrical lengths of both modes are equal ($\theta_e = \theta_o$, the stub complementary to the slot), the image impedance gets frequency independent and the coupling section can behave as an all-pass structure. This is the principle of the

broadband matching in the complementary strip-slot, which will be detailed in Sec. 2.3.

In addition, the phase factor (i.e. the phase of S_{21} provided the circuit is loaded by Z_{im}) when the electrical lengths for both modes are equal ($\theta = \theta_e = \theta_o$) is given by

$$\cos \phi = \frac{\frac{Z_{0e}}{Z_{0o}} - \tan^2 \theta}{\frac{Z_{0e}}{Z_{0o}} + \tan^2 \theta}. \quad (2.5)$$

2.2.2 Equivalent Circuit

Recently, alternative lattice equivalent circuits have been proposed for coupled-line sections, with the advantage of wideband validity and the use of no approximations [17]. These equivalent circuits consist of lattice networks with branches that are made up of realizable transmission line sections with the parameters of either the odd mode or the even mode, thus allowing the modelling of the dispersion due to the different phase velocities of even and odd modes.

Lattice topologies have long been used in communications systems and their main properties are summarised in Appendix B. The network topology of a symmetrical lattice is reproduced in Fig. 2.6. They have the advantage with respect to T- and Π -topologies that they can exhibit a frequency-independent image impedance, Z_{im} , under certain conditions. The image impedance of a symmetrical lattice network is given by [18]

$$Z_{im}(w) = \sqrt{Z_a(w)Z_b(w)} \quad (2.6)$$

where $Z_a(w)$ stands for the series impedance and $Z_b(w)$, for the cross impedance, as Fig. 2.6 shows.

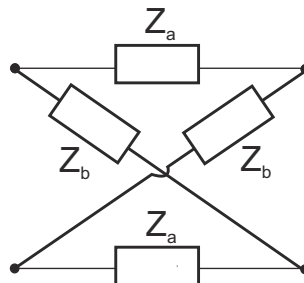


Figure 2.6: General symmetrical lattice network.

According to the coupled-section termination of the proposed structure and its resulting impedance matrix (2.3), the corresponding lattice equivalent circuit is the one

presented in Fig. 2.7. In this case, $Z_a(w)$ corresponds to (2.2b) and $Z_b(w)$, to (2.2a), thus leading to the same expression of the image impedance reached by the even-odd mode analysis (2.4). Therefore, the use of a lattice topology for the equivalent circuit of the coupled subsection provides an excellent physical understanding about how the even and odd modes are combined. The equivalent circuit of the total coupled section is simply the parallel connection of two equal coupled subsections.

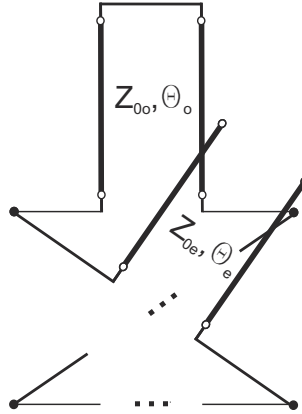


Figure 2.7: Equivalent circuit for the coupled subsection of Fig. 2.4.

Moreover, due to the field distributions of the even and odd modes, almost similar, as aforementioned, to the microstrip and slotline modes, respectively, it can be assumed that the series branch is exclusively determined by the slot geometry and the cross branch by the strip one. Hence, the equivalent circuit does not only include the matching capability of the structure but also the physical independence of the modes (different branches in the lattice topology). Fig. 2.8 illustrates this independence clearer. Each row of the figure represents simple equivalent circuits for a microstrip-fed slot, a microstrip-fed strip and the proposed structure. It has to be pointed out that these equivalent networks model only the element, but neither the feed microstrip nor the transition from the microstrip to the element. Firstly, it is shown the general equivalent circuit for each structure. In addition, the equivalent lattice network for each of them is detailed in the third column as well as the lattice equivalent network using transmission lines in the last column.

A microstrip-fed slot behaves as a series impedance, which can be represented using a lattice topology as two impedances of half value. A simple equivalent circuit for the centred-fed slot of Fig. 2.8 is the parallel connection of two equal slotlines terminated by short circuits. This parallel connection, when represented as a lattice network, results in the circuit of the last column of Fig. 2.8. Likewise, a microstrip-fed strip behaves as a parallel admittance and a simple equivalent circuit using transmission lines

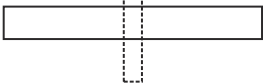
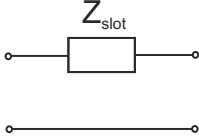
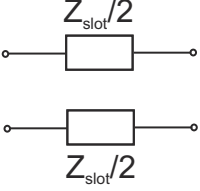
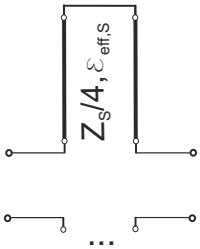
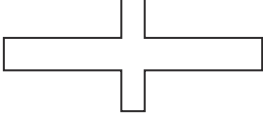
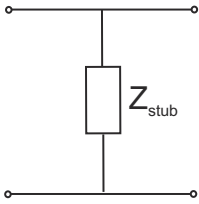
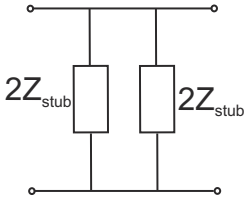
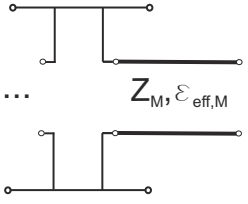
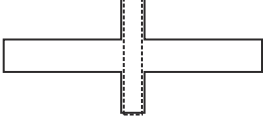
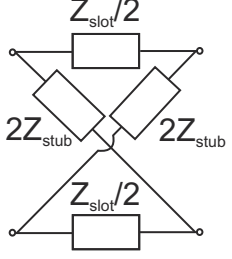
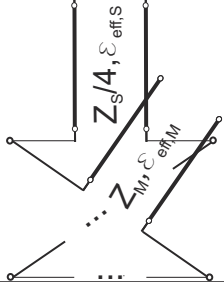
	General equivalent circuit	Equivalent lattice network	Equivalent lattice using TLs
<p>SLOT</p> 			
<p>STRIP</p> 			
<p>PROPOSED STRUCTURE</p> 	<p>—</p>		

Figure 2.8: Equivalent circuit comparison for a microstrip-fed strip, for a microstrip-fed slot and for the proposed structure.

could be two parallel microstrip lines terminated by open circuit. For the proposed structure, it is shown that the equivalent circuit results in a lattice topology, which is the combination of the equivalent lattice networks of the two elements that make up the proposed structure. Thus, the branches are determined by the impedances of the slot and the strip independently, leading to the equivalent circuit shown in the last column. The series branch is the corresponding slotline terminated by short circuit and the cross branch is the corresponding microstrip line terminated by open circuit. In accordance with relations (2.1a) and (2.1b), this equivalent circuit is the same as the resulting parallel connection of two coupled subsections with the equivalent circuit shown in Fig. 2.7, as expected.

A more problematic issue is the consideration of the losses in the equivalent circuit. Most of the losses in the proposed structure comes from radiation. As will be seen in 2.2.3, the radiation losses can be mainly attributed to the slot, therefore, it may be reasonable to neglect the losses of the cross branches of the lattice network. However,

the radiation from the slot deserves the insertion of the losses into the series branches of the equivalent lattice network. Some literature can be found regarding the modelling of the losses in a microstrip-fed slot. The first transmission line models considered the radiation of the slot as an experimentally determined resistance located at the centre of the slot, in parallel with a perfect slotline [19]. Later on, the model as a lossy transmission line was introduced and a theoretical derivation of the loss-per-unit length was proposed [20]. However, there is still not a closed solution for the problem and very recently an improvement of the previous model was published [21]. Anyway, these theoretical models are rather complex and, for the aim of this thesis, a simpler equivalent model was preferred. As described in Section 2.3, the design for broad matching can be carried out neglecting the losses completely. When the equivalent circuit must have been used for modelling the structure, the losses have been estimated according to empirical or simulated results.

2.2.3 Radiation

Since the strip-slot structure is proposed as a matched series-fed slot radiator, it is required to analyse how the strip modifies the radiation properties of the slot, especially in the zx -plane (see axes in Fig. 2.1), along which the potential series-fed array would be built. It can be assumed that the strip element essentially contributes to the $-z$ semispace radiation and the radiation into the $+z$ semispace is mainly due to the slot, which radiates into the whole space. Fig. 2.9 shows the equivalent magnetic current \vec{M} and the equivalent electric current \vec{J} along the slot and the strip, respectively, obtained with the *Field Calculator* of ANSYS HFSS [22]. They are computed as $\vec{M} = -\vec{n} \times \vec{E}$ and $\vec{J} = -\vec{n} \times \vec{H}$, where \vec{n} is a vector perpendicular to the surface of the slot/strip. It can be observed that, because of the way the strip is fed, the current along it is not appropriate for radiation purposes (opposite directions in the two subsections) and its contribution to both the $+z$ and $-z$ semispaces is less than the slot one, which is excited in a better manner for radiation. Consequently, it is also expected that the radiation pattern is similar to that of the slot although slightly altered by the strip. Nevertheless, it is unclear how much the presence of the stub modifies the radiation of the slot. This issue is addressed next.

If the lattice equivalent circuit of the strip-slot element is considered and low coupling is assumed, the series branch of the lattice network has the impedance of the slot and the cross branch, that of the strip, as shown in Fig. 2.8. This identification of

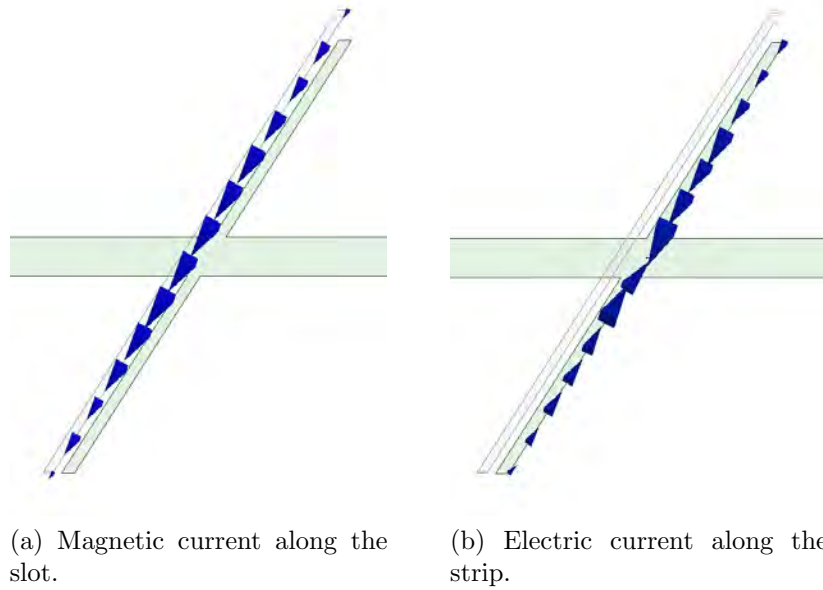


Figure 2.9: Equivalent currents along the elements at the resonance frequency of the slot.

the lattice branches with physical elements of the structure is rather important, since it allows the understanding of the radiation thanks to a relevant circuit property of symmetrical lattice networks, detailed in Section B.2.

If the dielectric and conductor losses are considered negligible, the power radiated by the complementary strip-slot must be the total dissipated power in its equivalent lattice network:

$$P_{rad} = 2(P_a + P_b). \quad (2.7)$$

In Section B.2, it has been proven that, in a symmetrical lattice network loaded with the same impedance as the generator ($Z_g = Z_L$), the power dissipated in the impedance of the series branch P_a is independent of the impedance of the cross branch, Z_b , and vice versa. Since the complementary strip-slot is excited by a microstrip line and terminated in a matched load, the condition $Z_L = Z_g$ is fulfilled. Then, this means that the dissipated power in the series branch of the complementary strip-slot lattice network is the dissipated power in a slot when the strip is not present (i.e. a conventional microstrip-fed slot). Likewise, P_b can be obtained from the computation of a microstrip centre-fed stub without the slot on the ground plane. Consequently, the radiation properties of the complementary strip-slot can be deduced from those of its elements separately. In fact, the microstrip-fed slot and the microstrip centre-fed stub are the resulting structures when odd and even excitations are applied. It is well

known that a microstrip centre-fed stub does not radiate efficiently due to the current distribution on its surface. On the contrary, a microstrip-fed slot is a good radiator. Therefore, it is expected that the radiation of the complementary strip-slot is similar to that of the conventional microstrip-fed slot, except for the small contribution of the stub, as concluded from the observation of the equivalent magnetic and electric currents.

2.3 DESIGN FOR BROAD MATCHING

Due to the resulting image impedance of a coupled subsection in (2.4), impedance matching of the total coupled structure (parallel connection of two subsections) can be easily achieved by fulfilling the following relations:

$$\theta_e = \theta_o \quad (2.8a)$$

$$\frac{1}{2}\sqrt{Z_{0e}Z_{0o}} = Z_0 \quad (2.8b)$$

where Z_0 stands for the characteristic impedance of the microstrip feed line.

Taking into account (2.1a) and (2.1b), the conditions (2.8a) and (2.8b) can be written in terms of the transmission line parameters of the equivalent circuit of Fig. 2.8:

$$\theta_M = \theta_S \quad (2.9a)$$

$$\frac{1}{2}\sqrt{Z_M Z_S} = Z_0. \quad (2.9b)$$

If losses are considered negligible, (2.8a) can be expressed as

$$\sqrt{\epsilon_{eff,M}} \cdot l_M = \sqrt{\epsilon_{eff,S}} \cdot l_S. \quad (2.10)$$

Consequently, for a good matching, (2.9b) and (2.10) must be satisfied simultaneously. There are four geometrical variables (w_S , w_M , l_S and l_M) to achieve the design. Two of these variables have to be used to achieve impedance matching, the other two provide two degrees of freedom in the design, which can be used to adjust the phase factor at a single frequency and the ratio $Z_{0,e}/Z_{0,o}$, which determines both the frequency dependence of the phase factor (2.5) and the amount of radiation, as will be

shown in Section 2.5.

Therefore, the design methodology can be reduced to a few steps. Due to the frequency dispersion inherent in the parameters of the elements, relations (2.9b) and (2.10) can be exactly fulfilled at only one frequency. Thus, firstly, it is necessary to select the design frequency, at which the design will be carried out. For simplicity in the posterior adjustment of the elements' lengths, this frequency will coincide to the resonance frequency, f_r , of a radiating slot with the proposed dimensions (frequency at which its length is quarter wavelength). For that frequency, it is possible to analyse the characteristic impedances of the modes, or Z_M and Z_S , as a function of the strip and slot widths using, for example, HFSS, and, accordingly, choose a pair of values for w_M and w_S that satisfies condition (2.9b). Infinite combinations of w_M and w_S can fulfil this equation; however, depending on the selected values, the performance of the radiating element might change. After matching the image impedance of the structure to the characteristic impedance of the feed microstrip line at f_r , it is necessary to achieve wideband matching. With this purpose, l_S must be picked out such that the slot resonates at f_r and then the length of the strip l_M must be adjusted to fulfil condition (2.10), which is equivalent to make the strip resonate at f_r , as well. Although $\epsilon_{eff,M}$ and $\epsilon_{eff,S}$ present different frequency dispersion, it can be considered that (2.10) is approximately satisfied over a wide frequency range due to the slow dispersion of both terms. Results will confirm this hypothesis.

It is worth pointing out here that an important advantage of the proposed structure is the almost independent control of the design variables. The even and odd modes can be controlled separately by adjusting the strip and slot widths and lengths, thus making possible not only the wideband impedance matching behaviour but also the choice of the resonance frequency of the slot or the amount of radiation, by choosing the pair of w_S and w_M .

2.4 RESULTS

In this section, the two manufactured prototypes are introduced in order to show the experimental results that have been obtained for each of them as well as comparisons with simulations. Circuit results as a two-port structure are shown for both prototypes and radiation results, for Prototype 2.

2.4.1 Prototypes

In order to verify the behaviour of the structure experimentally, two prototypes were manufactured and measured:

- Prototype 1:** A design for the proposed structure has been carried out on RO4350B substrate, with $\epsilon_r=3.66$ and 30 mil of height. A picture of the fabricated structure is shown in Fig. 2.10. The resonance frequency has been fixed at $f_r=5.4$ GHz and the width of the feed microstrip line has been set to 1.67 mm for $50\ \Omega$ -impedance. Accordingly, the chosen pair of strip and slot widths that satisfies condition (2.9a) is $w_M=0.3$ mm and $w_S=0.3$ mm. The slot and strip lengths have been separately adjusted to make each one resonate at f_r . The resulting lengths are $l_M=8.6$ mm and $l_S=10.2$ mm. A tapered transition between the connector and the $50\ \Omega$ -microstrip line was introduced in order to use the TRL calibration kit designed for other purposes. As will be seen in the results, this transition caused some problems at high frequencies. For this reason, Prototype 2 was manufactured.

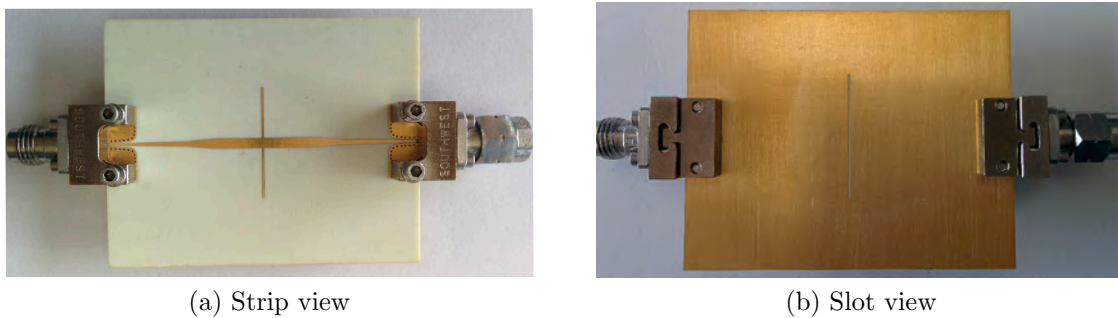


Figure 2.10: Manufactured structure on RO4350B (Prototype 1).

- Prototype 2:** Another design was manufactured on GIL 1032 substrate, with $\epsilon_r=3.2$ and 30 mil of height. As done for the Prototype 1, the resonance frequency was also fixed at $f_r=5.4$ GHz and the width of the feed microstrip line, set to 1.84 mm for $50\ \Omega$ -impedance. The chosen width pair in this case for fulfilling condition (2.9a) were $w_M=0.61$ mm and $w_S=0.47$ mm. The resulting lengths were $l_M=9.18$ mm and $l_S=10.76$ mm. A photograph of this prototype can be observed in Fig. 2.11.

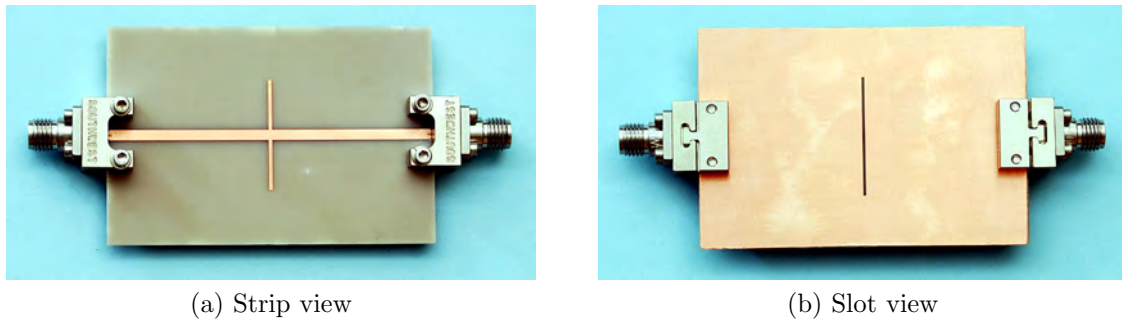


Figure 2.11: Manufactured structure on GIL 1032 (Prototype 2).

2.4.2 Results as Circuit Element

This section collects the circuit results obtained from measurements, simulations and theory for the previously described prototypes.

Prototype 1

For these dimensions, Fig. 2.12 shows the simulated characteristic impedance and effective permittivity for the even and odd modes of the manufactured structure, obtained with CST Studio [23]. A slight frequency dispersion of both parameters can be observed in the figure.

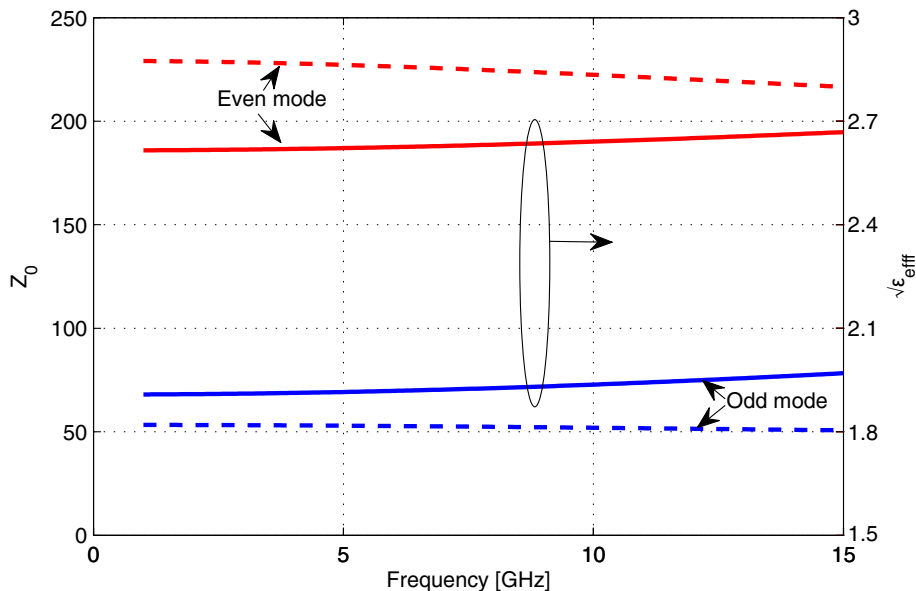


Figure 2.12: Simulated characteristic impedances and effective permittivities of the modes for Prototype 1.

In order to prove the validity of the proposed equivalent circuit, Fig. 2.13 shows

the resulting lattice impedances, Z_a and Z_b , extracted from the measured structure, in comparison to the modelled impedances with the equivalent circuit of Fig. 2.8 and the extracted impedances from electromagnetic simulation with HFSS. The results have been obtained using the symmetry plane of Fig.2.4 as reference plane for ports 1 and 2. The values shown in Fig. 2.12 have been used for the equivalent circuit. The losses have been only included in the series branch as a loss per unit length extracted from the conversion of the simulated S-Parameters to the impedances of the equivalent lattice network. Good agreement is noticed among the simulation, the measurement and the equivalent circuit, except for the measurement of the series impedance Z_a at high frequencies. This might be attributed to the transition that the microstrip line has from the connector, and to the calibration kit, which was not designed for such broad bandwidth. Moreover, a small shift can be observed between the equivalent circuit and the simulation and measurement curves. Since the lengths of the transmission lines modelling the even and odd modes according to Fig. 2.7 have been fixed to l_M and l_S , respectively, the slot short-end effect and the microstrip open-end effect have not been considered. Anyway, the proposed equivalent circuit, which simply consists of a lattice topology with transmission lines, can properly model the behaviour of the structure over the studied bandwidth. Consequently, it can be deduced that the effect of the parasitics of the transition between the feed microstrip line and the coupled section is not noticeable over this range. Nonetheless, it is expected that these parasitics become more pronounced at higher frequencies, thus being required their modelling.

If the design has been properly accomplished, the frequency-dependent response of the series-fed slot element must become flatter, thanks to the matching strip element. This behaviour is shown in Fig. 2.14, where the return losses of the proposed structure are detailed, comparing electromagnetic simulation with HFSS, measurement and equivalent circuit. The simulated return losses for the series-fed slot element without the strip (conventional slot) are also shown, thus highlighting the matching effect of the strip. The placement of the strip on the top layer of the series-fed slot enhances significantly the impedance bandwidth, compensating the resonant behaviour. In this case, the impedance bandwidth of the proposed structure easily reaches 15 GHz. It is proven then that good matching can be achieved with the previously detailed design methodology, which neglect losses.

The resulting image impedance, according to (2.6), is shown in Fig. 2.15. A strictly constant behaviour is not achieved since the design is carried out at one frequency and the parameters defining the modes present frequency dispersion. In addition, losses are

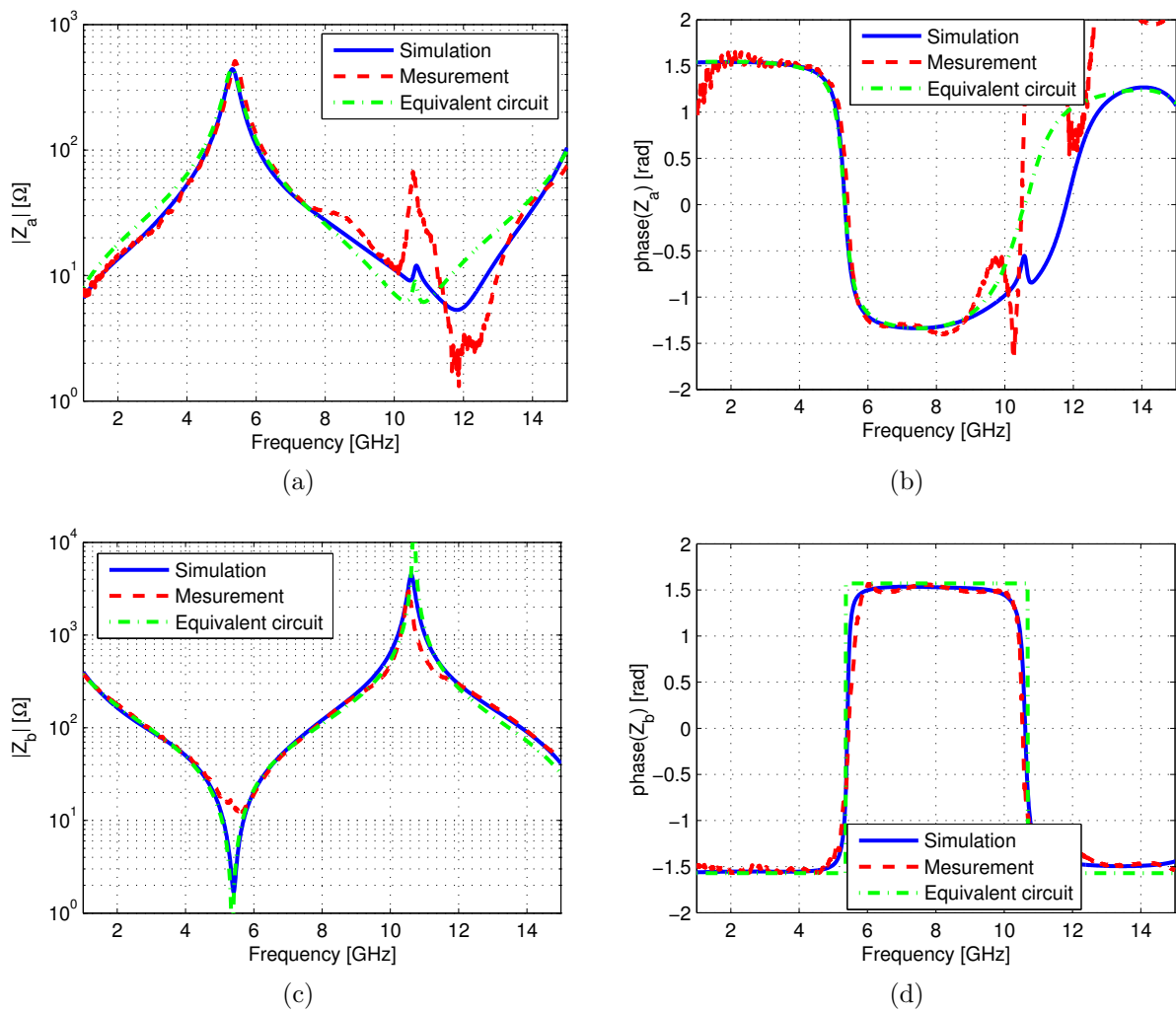


Figure 2.13: Magnitude and phase of the lattice impedances extracted from the measured and simulated structure and those from the equivalent circuit for Prototype 1.

involved. In spite of these effects not considered in the design, the values of the Z_{im} are around the $50\ \Omega$ -level. The highest deviation occurs around the resonance frequencies of the strip and the slot, as expected, since the lattice impedances have an asymptotic behaviour at these frequencies.

Prototype 2

For the prototype on GIL 1032, similar results to those of Prototype 1 have been obtained. Likewise, in Fig. 2.16, the simulated characteristic impedance and effective permittivity for the even and odd modes for this case show a similar behaviour to that of Fig. 2.12, for the other substrate. A slight frequency dispersion of both parameters

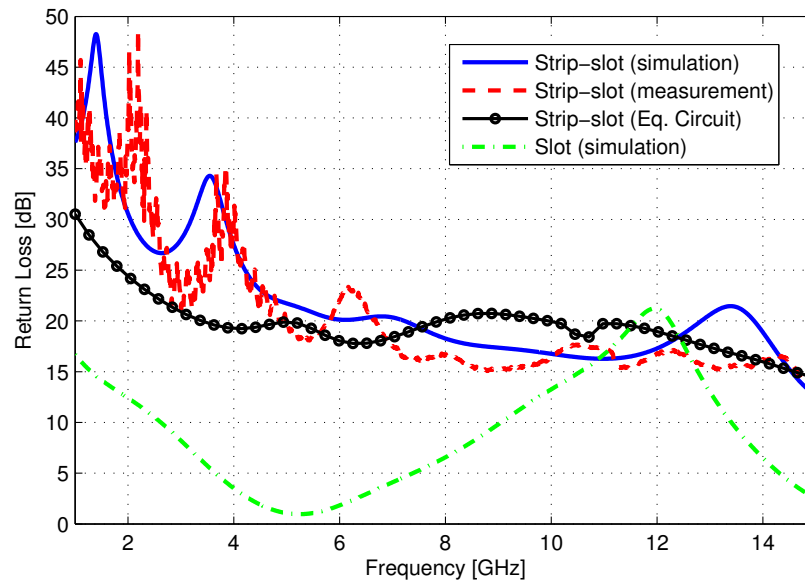


Figure 2.14: Return loss comparison between the manufactured structure (measurement and simulation) and the simulated microstrip-fed slot for Prototype 1.

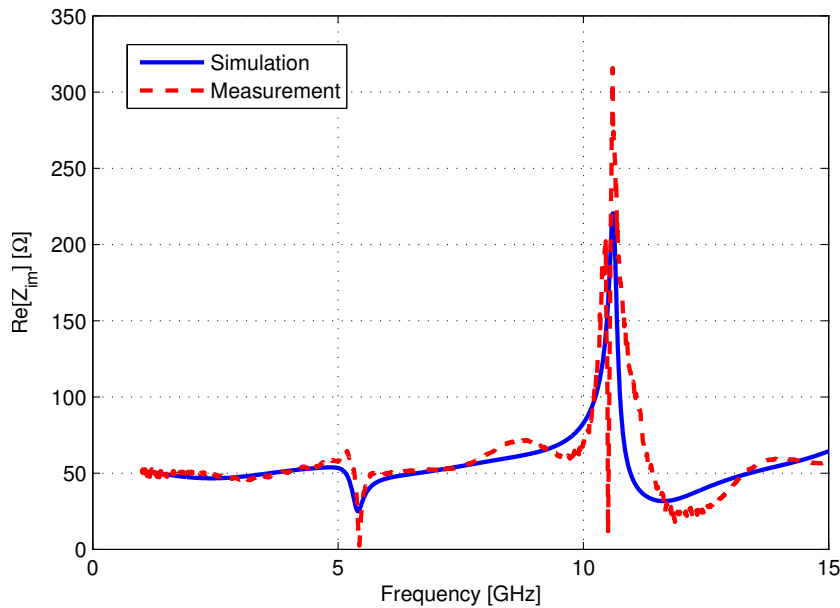


Figure 2.15: Resulting image impedance of the manufactured structure (measurement and simulation) for Prototype 1.

can be also observed.

The resulting lattice impedances for this case are shown in Fig. 2.17. Good agreement is also noticed here among the simulation, the measurement and the equivalent circuit, although again a small shift between the equivalent circuit and the other two curves can be observed. However, in this case, the slot short-end and the microstrip open-end effects seem to be less pronounced.

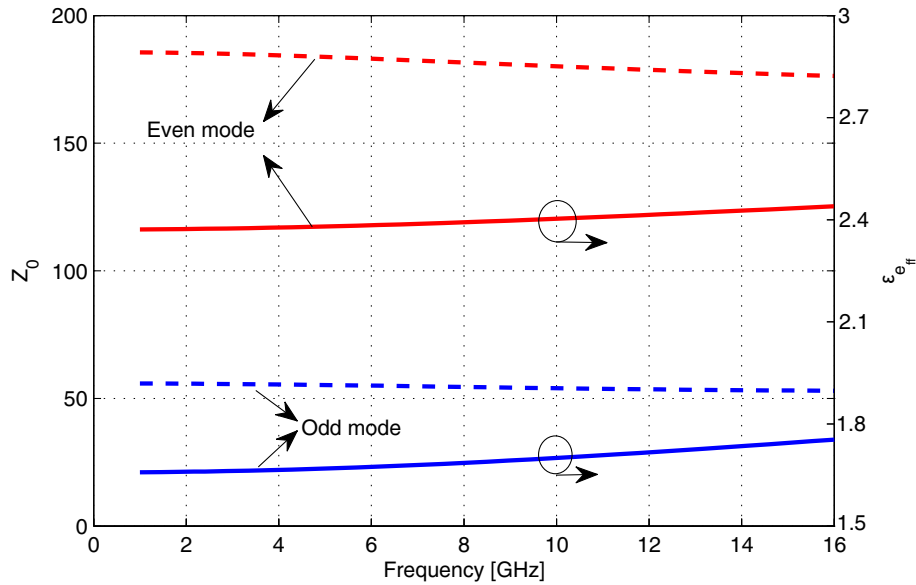


Figure 2.16: Simulated characteristic impedances and effective permittivities of the modes for Prototype 2.

Fig. 2.18 shows the comparison between the return losses of the proposed structure from the HFSS electromagnetic simulation, the measurement and the equivalent circuit and those for the series-fed slot element without the strip. The matching effect of the strip is also noticeable here. The resulting image impedance is shown in Fig. 2.19.

2.4.3 Results as Radiation Element

First of all, the validation of the statement in 2.2.3 is tackled. According to it, the power dissipated in the series branch of the equivalent lattice network (associated to the slot) is independent of the cross branch (associated to the strip) and viceversa. This would mean that the power dissipated in the series branch can be obtained from the microstrip-fed slot (without the stub) and the power dissipated in the cross branch, by the microstrip-fed stub (without the slot). With this purpose, Fig. 2.20 compares the dissipated powers in the two branches of the equivalent lattice network of the complementary strip-slot of Prototype 2, obtained from (B.8), with those obtained from the electromagnetic simulation of the isolated elements. The equivalent lattice impedances are calculated by converting the S-Parameters from the electromagnetic simulation of the structure (with HFSS) to Z-Parameters and then to Z_a and Z_b , as done for Fig. 2.17. The power dissipated in the series branches ($2P_a$) is compared to the simulated radiated power in the corresponding microstrip-fed slot and the power

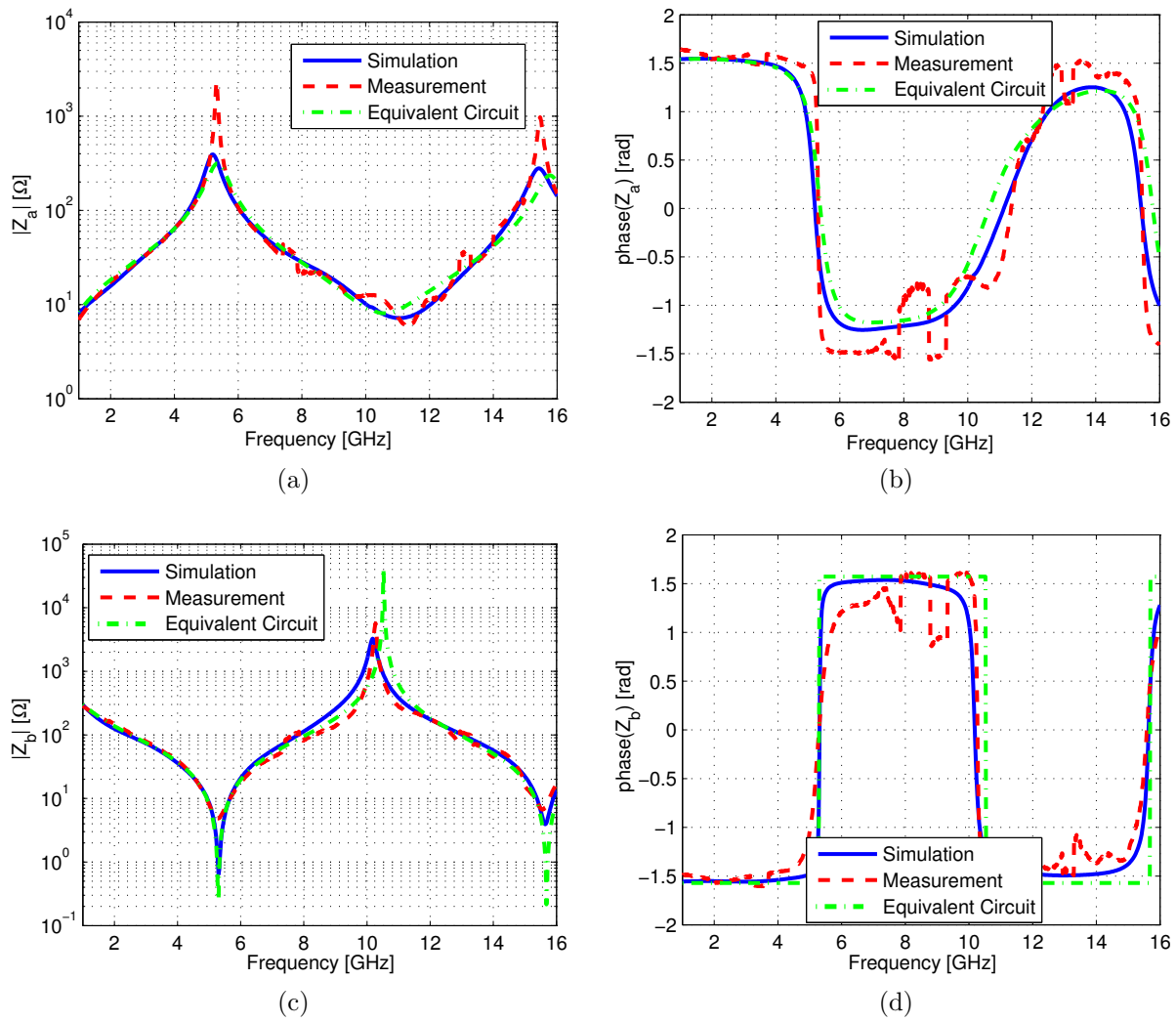


Figure 2.17: Magnitude and phase of the lattice impedances extracted from the measured and simulated structure and those from the equivalent circuit for Prototype 2.

dissipated in the cross branches ($2P_b$) is compared to the simulated radiated power in the corresponding microstrip centre-fed stub. Finally, the total dissipated power in the lattice network, $2(P_a + P_b)$, is compared to the simulated radiated power in the complementary strip-slot. Therefore, three different full-wave models have been used for the simulation. The results confirm the capability of the equivalent circuit to explain the radiation properties of the complementary strip-slot as the sum of the radiated powers by the microstrip centre-fed stub (without the slot) and by the microstrip-fed slot (without the stub) and the power independence property of the symmetrical lattice network. Moreover, the contribution of the stub is much smaller than that of the slot; therefore, the complementary strip-slot radiates essentially as a conventional slot, as predicted.

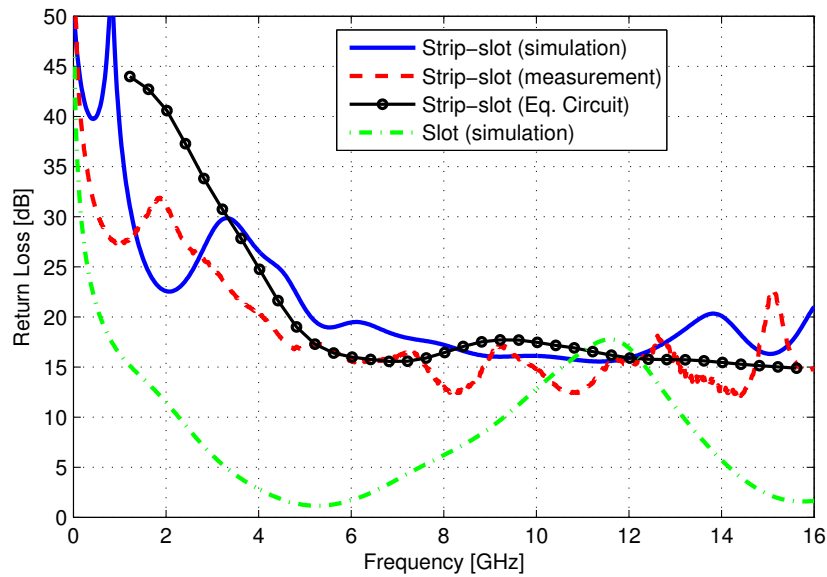


Figure 2.18: Return loss comparison between the manufactured structure (measurement and simulation) and the simulated microstrip-fed slot for Prototype 2.

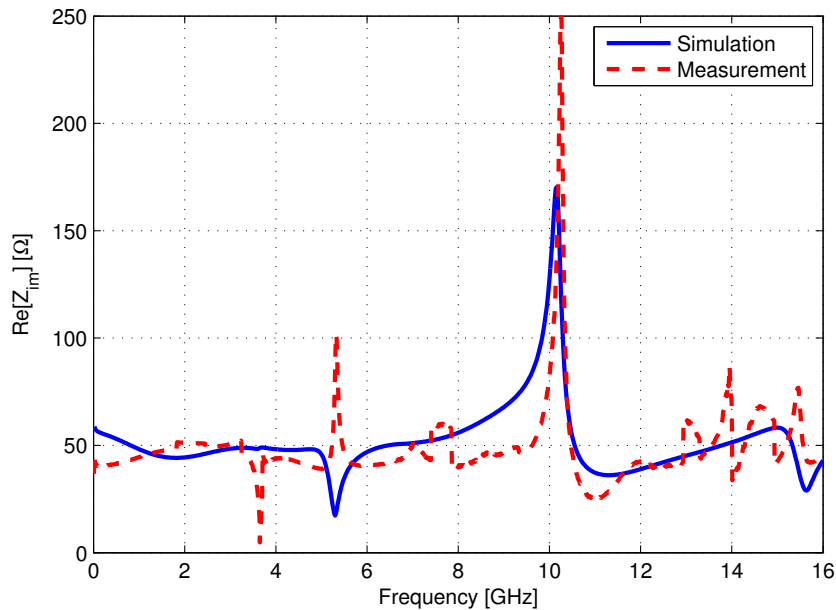


Figure 2.19: Resulting image impedance of the manufactured structure (measurement and simulation) for Prototype 2.

Although it is proven that the complementary strip-slot radiates essentially the same percentage of power (with respect to the available power) as a microstrip-fed slot without the stub, there is a remarkable difference as regards the rest of the power that is not radiated. Fig. 2.21 shows a comparison of the power dissipated in the load Z_L in the microstrip-fed slot and in the complementary strip-slot. It is shown that, although both structures radiate practically the same amount of power (Fig. 2.20), the strip-

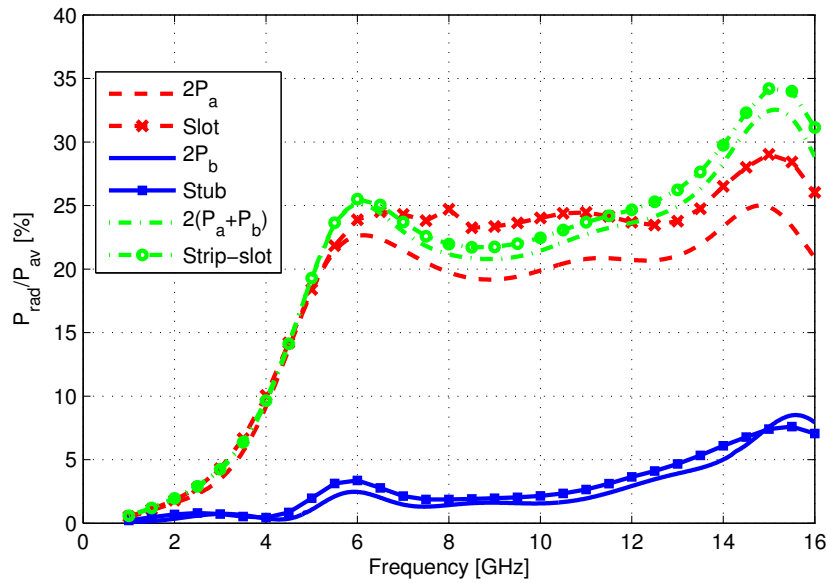


Figure 2.20: Comparison of the ratio between the radiated power and the available power in %, computed with the equivalent lattice circuit and by electromagnetic simulation of the isolated elements (conventional microstrip-fed slot and microstrip centre-fed stub) and the complementary strip-slot (Prototype 2).

slot transmits the rest of the power to the load over the whole bandwidth, whereas the slot has a resonant behaviour and there are frequencies at which it reflects the power instead of transmitting it. This can be easily understood with the equivalent circuits of both structures (Fig. 2.8): the slot equivalent circuit has only a series impedance whereas the strip-slot one is a lattice network, whose series branch is the impedance of the slot. The dissipated power in the slot does not change by the fact of adding the stub (cross branch in the lattice network), but the impedance does, and so does the matching.

In Fig. 2.22, the radiation diagrams of Prototype 2 (measured ¹ and simulated with HFSS) in the zx -plane are compared with the simulated microstrip-fed slot (proposed structure without the strip) for nine different frequencies over the studied bandwidth. Quite good agreement between the measurement and simulation is observed. Furthermore, the radiation pattern of the structure is similar to that obtained without the strip, thus confirming that the strip does not introduce any significant perturbation in the radiation pattern of the slot, especially in its corresponding semispace ($+z$), and just acts as a mere matching element, as predicted. Therefore, for the purposes of radiation into the $+z$ semispace the strip-slot is similar to a conventional slot. Then,

¹The radiation measurements were taken in the anechoic chamber of the Laboratorio de Ensayos y Homologación de Antenas, Universidad Politécnica de Madrid, Madrid (Spain).

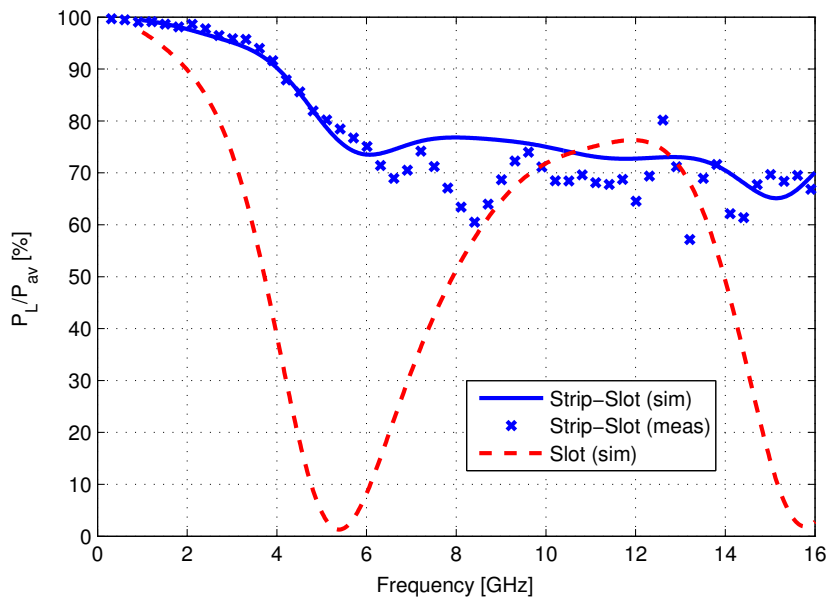


Figure 2.21: Comparison of the ratio between the dissipated power in the load and the available power in % in the complementary strip-slot and in the conventional microstrip-fed slot (Prototype 2).

the polarisation of the field radiated by the complementary strip-slot element is the same as the conventional microstrip-fed slot: it is linearly polarised and has horizontal polarisation when the plane of the antenna is perpendicular to the ground.

Regarding radiation efficiency (ratio between the radiated power and the accepted power), Fig. 2.23 shows that the element starts radiating efficiently from the resonance frequency associated to the slot on (5.4 GHz in this case). Below this frequency, the lower the frequency, the less efficient the structure becomes, as is the case of the conventional slot. However, unlike the conventional slot, almost constant behaviour of the radiation efficiency is obtained over broad bandwidth, which is highly desirable in broadband applications and is a consequence of the wide matching. Since both the slot and the strip-slot radiate almost the same amount of power, the difference in the efficiency is attributed to the matching (accepted power). In the strip-slot, around 25% of efficiency is achieved above the resonance frequency with this prototype; however, this value depends on the geometry of the element as shown in Section 2.5.

2.5 PARAMETRIC STUDY

As highlighted in Section 2.3, infinite combinations of w_M and w_S can fulfil condition (2.8b) at the design frequency f_r . Therefore, the objective of this section is the compar-

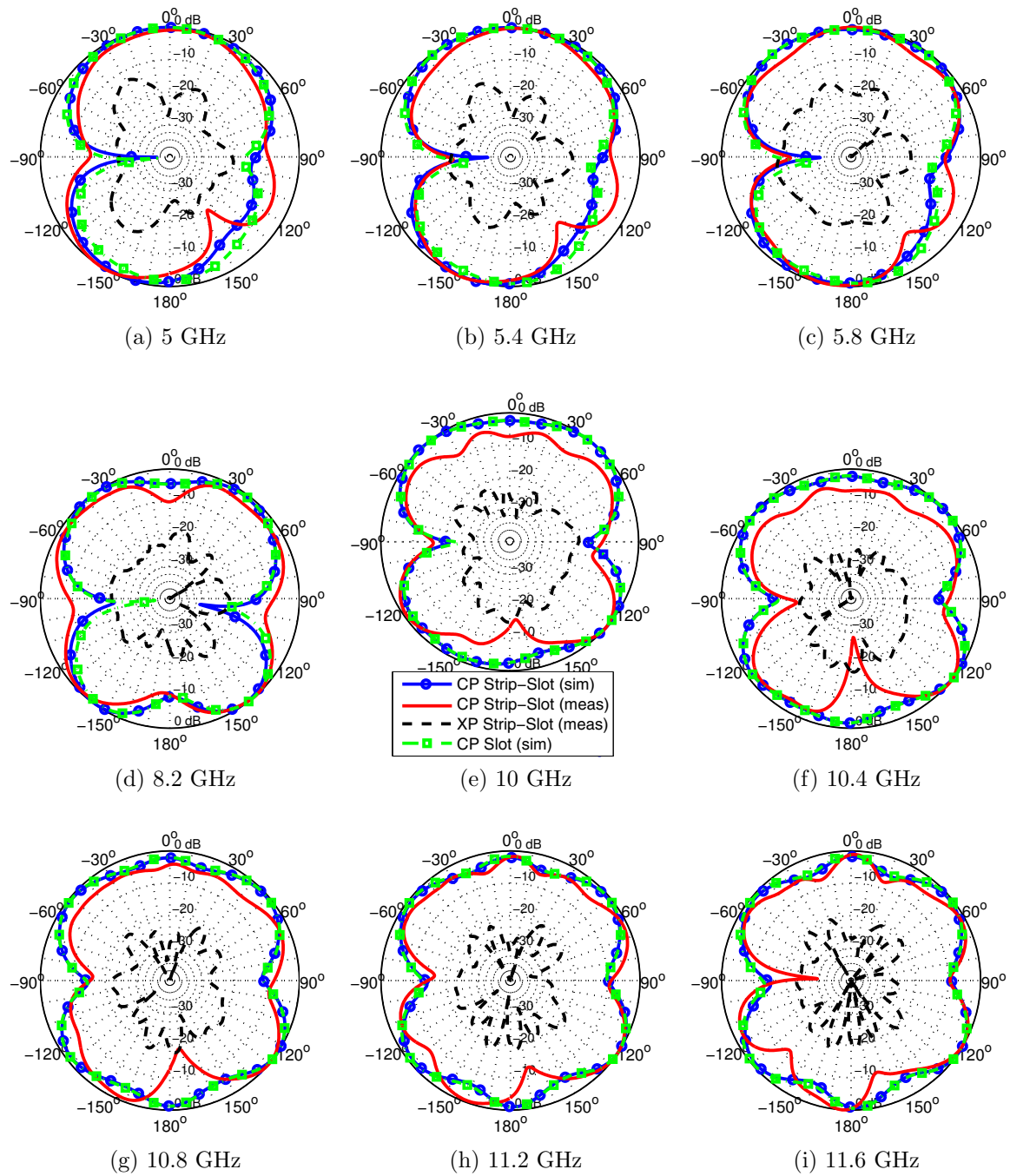


Figure 2.22: Normalized radiation patterns comparison for the simulated and measured structure and the simulated slot without the strip in the zx -plane (see axes of Fig. 2.1). The direction of the load corresponds to 90° .

ison of four different designs at the same design frequency, using different dimensions of the slot and strip.

Keeping the design frequency f_r to 5.4 GHz, it is possible to obtain the characteristic impedances, as well as the effective permittivities, of the even and odd modes of the

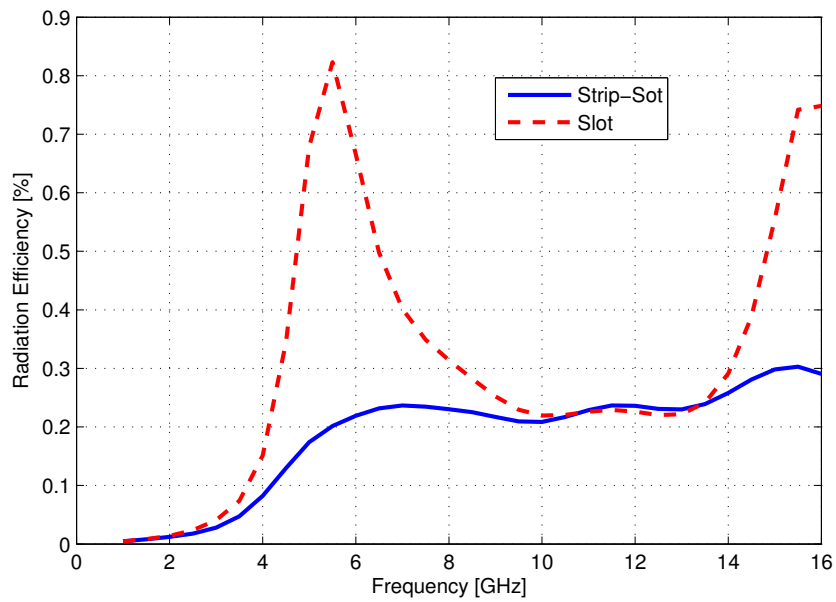


Figure 2.23: Simulated radiation efficiency (Prototype 2).

coupled section as a function of w_M and w_S using, for example, HFSS. The result of this analysis for the substrate of Prototype 2 at 5.4 GHz is detailed in Fig. 2.24. It can be observed from these figures that, for the even mode, an increase of the slot width leads to an increase in the characteristic impedance and a decrease in the effective permittivity. On the other hand, for the odd mode, an increase in the strip width makes the characteristic impedance lower and the effective permittivity higher, although this effect is less pronounced than in the previous case, since this mode is mainly confined around the slot. Moreover, the slopes of the curves give information on the deviation of the even and odd modes from the ideal assumption of microstrip and slotline modes, respectively, according to (2.1a) and (2.1b). It can be concluded that it would be a reasonably good approximation for the impedances for widths up to around 0.4 mm.

Besides the chosen dimensions for the manufactured design, infinite pair of widths can fulfil condition (2.8b), as aforementioned. From the modes impedances shown in Fig. 2.24a and 2.24b, it is straightforward to obtain both the theoretical image impedance and return losses for different dimensions, where the return loss is calculated as $-20\log((Z_{im} - Z_0)/(Z_{im} + Z_0))$, $Z_{im} = 1/2\sqrt{Z_{0,o}Z_{0,e}}$ and Z_0 stands for the characteristic impedance of the feed microstrip line ($50\ \Omega$). The isolines of these two magnitudes are detailed in Figs. 2.25 and 2.26 as a function of w_S and w_M . It is clear that a wide range of widths leads to a reasonably good matching for this substrate. For instance, for $w_S=1\text{ mm}$, w_M can range from 0.4 to 1.7 mm for a return loss better than 20 dB.

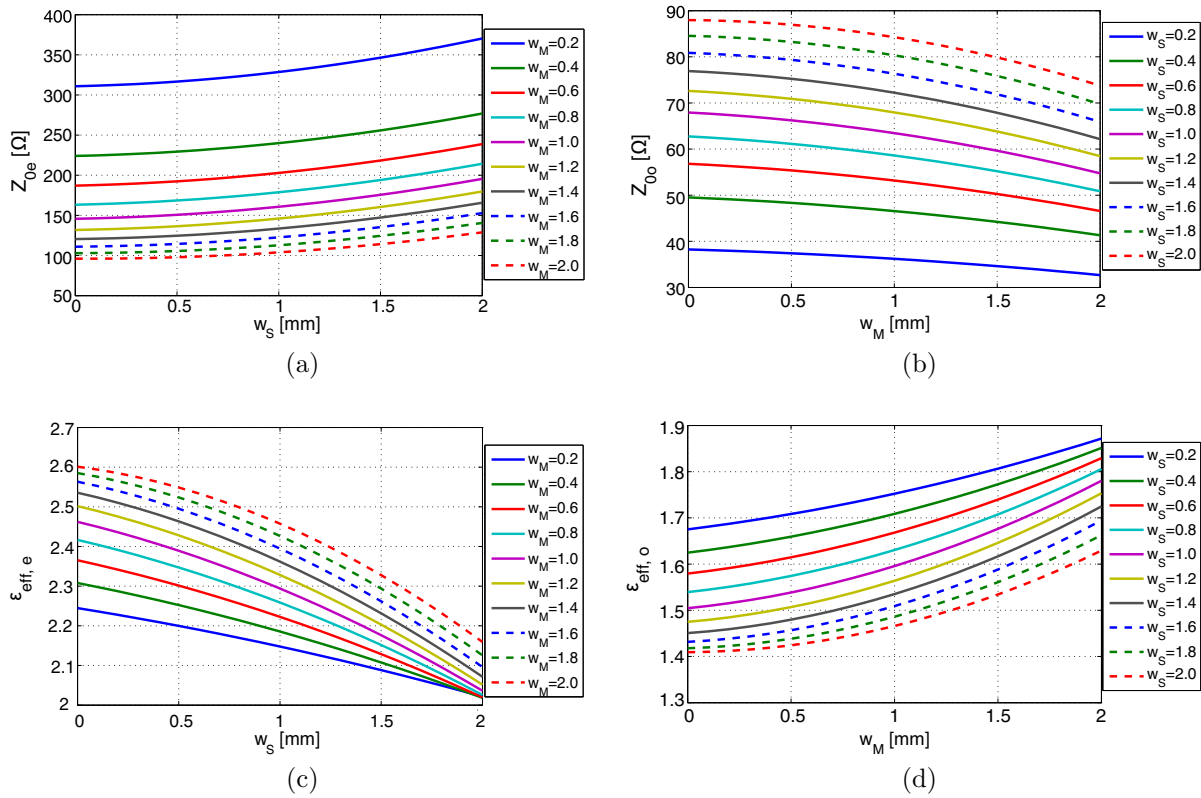


Figure 2.24: Characteristic impedances and effective permittivities of the even and odd modes of the coupled section at 5.4 GHz.

This fact means that the structure is quite robust with regard to dimensioning, an important advantage for design and fabrication. Moreover, the widths (and, hence, $Z_{0,e}/Z_{0,o}$) can be chosen also regarding the phase dependence on frequency, according to (2.5), or the radiation efficiency requirements. Once the widths have been chosen, the element lengths l_S and l_M have to be adjusted to fulfil (2.8a), for which another degree of freedom is available, which allows the phase to be set at a single frequency.

Fig. 2.27 shows the isolines of the coupling coefficient of the coupled section, $k = \frac{Z_{0e} - Z_{0o}}{Z_{0e} + Z_{0o}}$, as a function of w_S and w_M . It can be observed that, for constant return losses, different coupling coefficients can be obtained by choosing different pairs of widths. In fact, for an isoline of 50Ω -image impedance, the coupling coefficient can vary between 0 and 1. This factor is closely related with the phase response in (2.5); therefore, the phase response can be controlled independently of the return losses.

In order to compare with HFSS how an increase in the widths affects the performance, four different pairs of widths that achieve good impedance matching have been chosen and are shown in Table 2.1. The strip and slot lengths have been selected to resonate at f_r , that is, setting the phase factor at f_r to 180° , as carried out in the man-

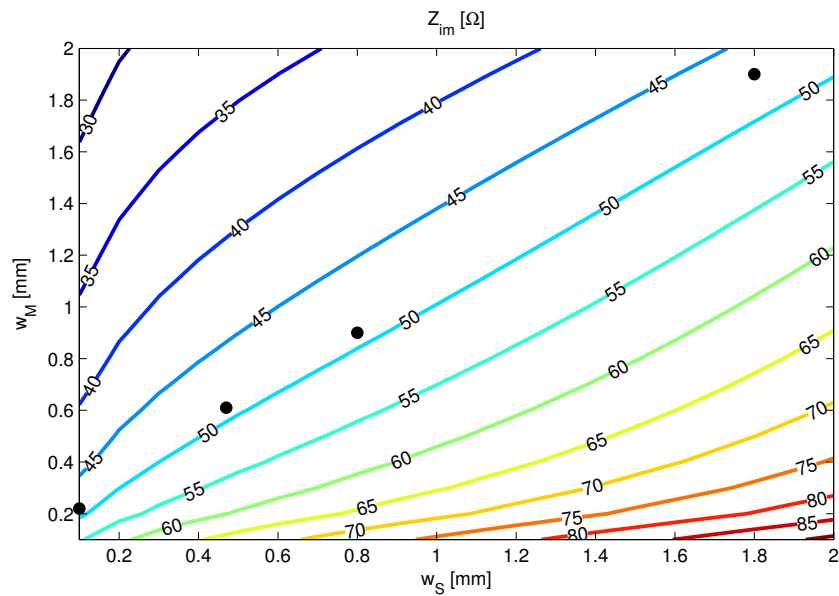


Figure 2.25: Isolines of the image impedance of the coupled section at 5.4 GHz. The designs of Table 2.1 are marked with black dots.

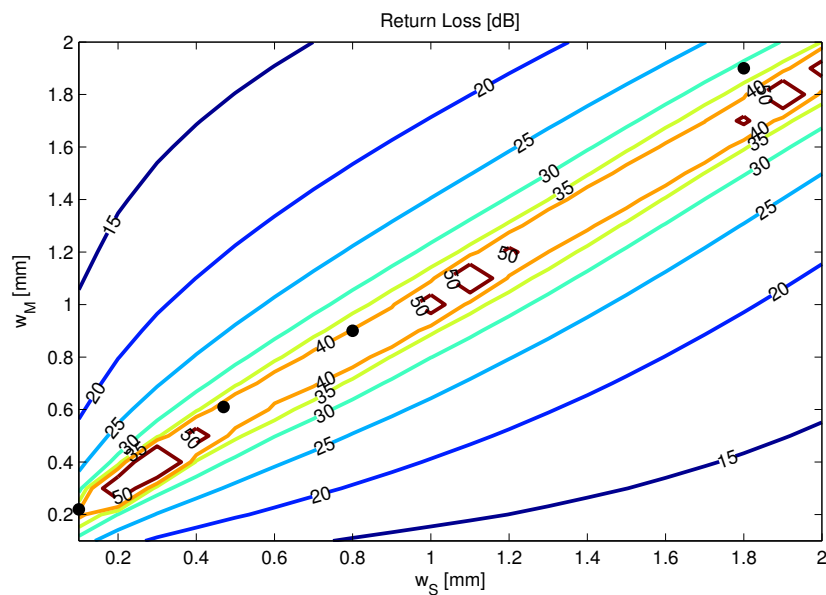


Figure 2.26: Isolines of the return loss of the coupled section at 5.4 GHz. The designs of Table 2.1 are marked with black dots.

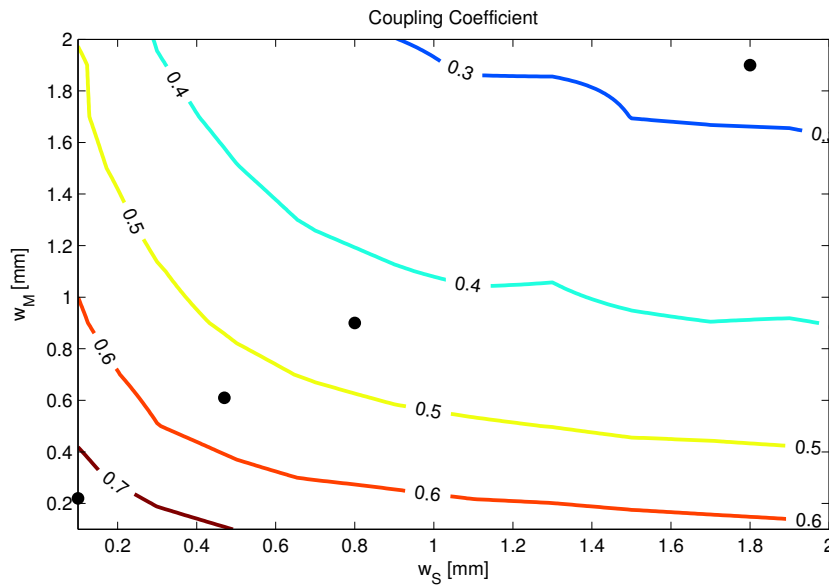


Figure 2.27: Isolines of the coupling coefficient k of the coupled section at 5.4 GHz. The designs of Table 2.1 are marked with black dots.

ufactured design, so that (2.10) is satisfied. Design 2 corresponds to the manufactured structure (Prototype 2). The four designs are also marked in Figs. 2.25, 2.26 and 2.27 with black dots.

Table 2.1: Dimensions of different designs for comparison.

	w_M	w_S	l_M	l_S
Design 1	0.22 mm	0.10 mm	9.13 mm	10.45 mm
Design 2	0.61 mm	0.47 mm	9.18 mm	10.76 mm
Design 3	0.90 mm	0.80 mm	9.04 mm	10.86 mm
Design 4	1.90 mm	1.80 mm	8.72 mm	9.99 mm

In Fig. 2.28, the return losses for the designs in Table 2.1 are compared. It is clear that broad impedance bandwidth can be achieved independently of the dimensions of the elements provided that the design methodology is followed. Therefore, a powerful characteristic of the proposed structure is the maintenance of the broad bandwidth behaviour for different element widths, thus providing an important degree of freedom in the design, which might be used for adjusting the phase of the elements in an array configuration or the amount of radiation.

The image impedances of the designs of Table 2.1 are detailed in Fig. 2.29. Similar behaviour have been obtained for the four designs. It must be clarified that, for the Design 4, the resonance frequency f_r has not been obtained at 5.4 GHz, that is why

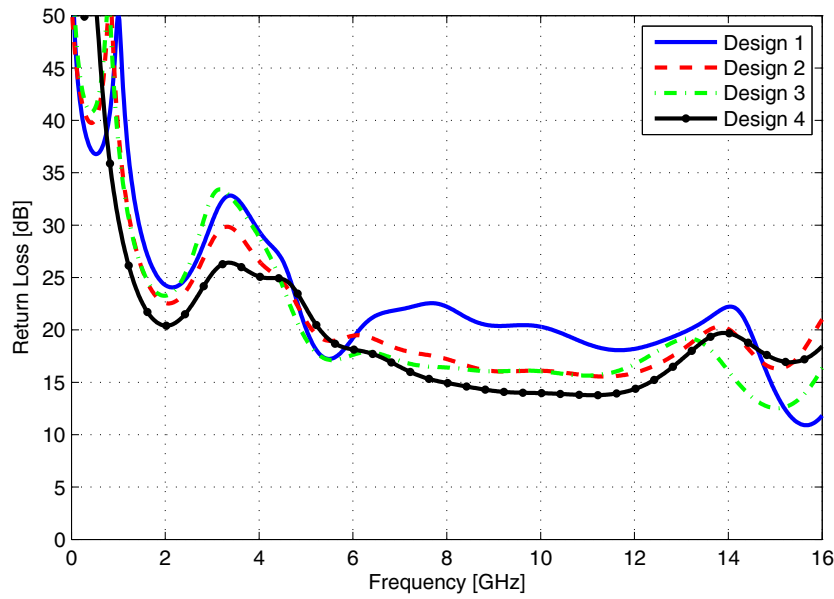


Figure 2.28: Comparison of the return loss for the four designs of Table 2.1.

there is a shift with respect to the rest of the curves. The strip and slot are made resonant at f_r by making $l_S = l_M = \lambda/4$. When the widths increase, the need of a length correction, due to the slot and strip end and junction effects, is higher. However, the perfect tuning of the resonance frequency has not been the purpose here. For that reason, this correction has not been carried out and is the main cause of the shift among the curves.

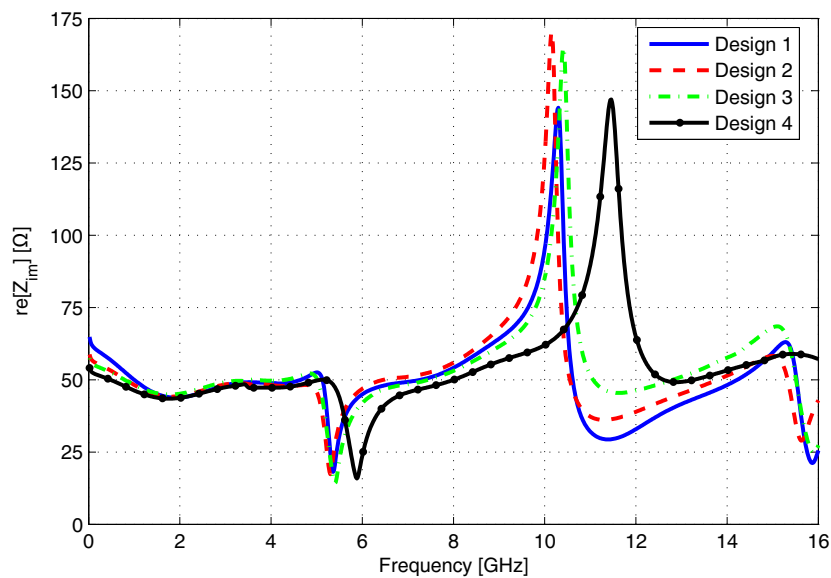


Figure 2.29: Comparison of the real part of the image impedance for the four designs of Table 2.1.

Although the change in the dimensions of the structure does not modify the broad

impedance matching behaviour when correctly designed, it does modify the phase response and the amount of losses (specifically, radiation losses). Fig. 2.30 shows the phase of the S_{21} for the four analysed designs. The wider the elements are, the higher the coupling coefficient is and then, the more linear the phase response of the corresponding coupled section is, which agrees with (2.5).

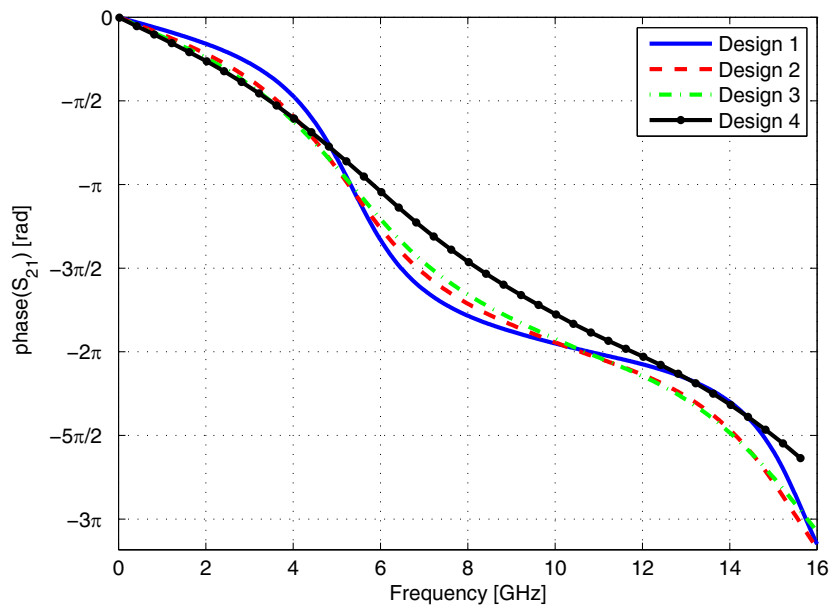


Figure 2.30: Comparison of the phase response for the four designs of Table 2.1.

Fig. 2.31 shows the simulated radiation efficiency for the four designs of Table 2.1. As the widths of the strip and slot are made higher, an interesting increase in the radiation efficiency can be observed between the two frequencies at which the slot length is $\lambda/2$ and $3\lambda/2$, which are also the frequencies at which the phase factor is fixed for all the designs (Fig. 2.30). Therefore, it is highlighted that the strip-slot element is not only able to provide broadband matching but also allows the control of the radiation efficiency or the phase response, which is an important feature for building competitive series-fed arrays in which certain flexibility in the magnitude and in the phase of the excitations is essential.

2.6 CONCLUSION

In this chapter, the so-called complementary strip-slot has been introduced as an alternative to the narrow-band conventional microstrip-fed slot. The proposed structure is a novel planar broadband series-fed radiating element based on the microstrip-slotline

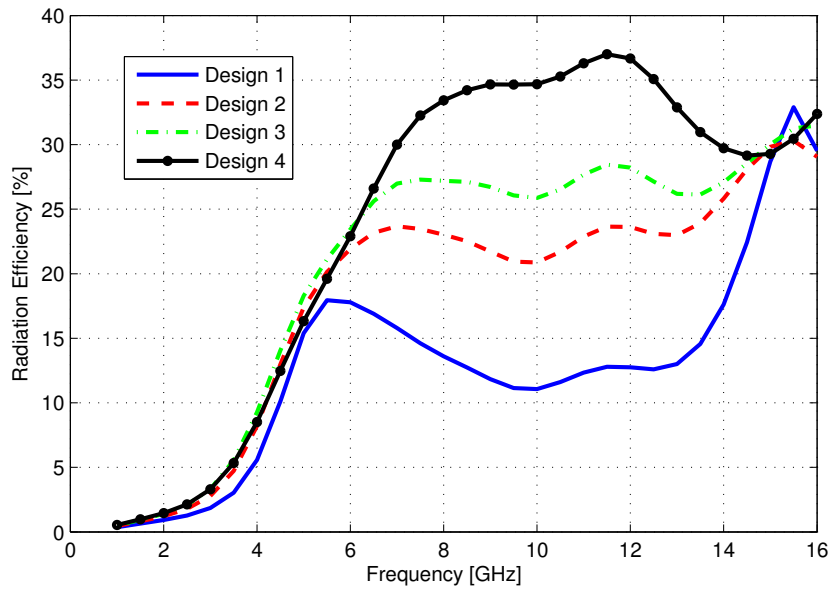


Figure 2.31: Comparison of the simulated radiation efficiency of the four designs of Table 2.1.

coupling and modifies the geometry of the conventional slot with the use of a strip superimposed on it. Therefore, it is easy to manufacture and quite inexpensive.

The bandwidth enhancement is achieved thanks to the resulting coupled-line configuration. However, it is because of the properties of the strip-slot coupling that it is possible to design the parameters of both modes independently and achieve broadband matching with a very simple design and easy adjustment. Since the range of widths for obtaining good impedance bandwidth is quite broad, the structure is robust as regards dimensioning. A lattice-based equivalent circuit has been proposed, which is able to both model the impedance and phase responses of the structure properly, thus allowing a useful pre-design, and predict the radiation properties.

The design methodology has been established based on closed-form formulas and validated with manufactured designs, in which it is important to mention that no further optimisation has been performed. The measurements show good agreement with simulation and theory and proves an impedance bandwidth that, in the manufactured prototypes, can easily reach 16 GHz from DC, which corresponds to around the triple of the resonance frequency associated to the slot. Experimental and simulated radiation results show that the strip practically does not modify the slot radiation pattern and just acts as a mere matching element. Moreover, certain control in the phase response and the radiation efficiency with the geometry is possible without compromising the good matching.

The structure simplicity, versatility and feeding configuration makes it especially suitable for series-fed arrays. Since the structure is just a matched microstrip-fed slot, it allows the design of slot arrays for additional applications, traditionally unfeasible due to the element's narrow bandwidth. Although the effective bandwidth of the array will be determined by other parameters, feeding networks, etc.; the availability of a broadly matched element is a relevant advantage to design arrays with extended features.

Chapter 3: Strip-Slot-Based Linear Travelling-Wave Arrays

The availability of a novel radiating element suggests its immediate application in building arrays. One-dimensional microstrip arrays have been widely used as they are easy to mount on surfaces and to integrate with active devices and have light weight and low cost. Series feeding has several advantages with respect to corporate feeding such as their small size, simplicity and less spurious radiation from the feed lines. Moreover, for beam steering, this feeding topology is more attractive, due to the cumulative phase shift between the elements, which contributes to setting the required phase shifts.

Since the complementary strip-slot has a series feeding structure and is in microstrip technology, the implementation of planar travelling-wave arrays (TWAs) using this element is straightforward by loading a microstrip line with several strip-slots. This is the topic dealt with in this chapter. The goal is to highlight the versatility of the array and the design simplicity provided by the broad impedance matching of the basic element.

There are different categories in TWAs. Those in which the power is radiated gradually (either in a continuous or a discrete way) along the guiding structure are known as Leaky-Wave Antennas (LWAs). The array with complementary strip-slot elements can be then regarded as a LWA, since the radiation takes place discretely along the microstrip feed line. On the other hand, it can be also considered a linear phased array, in which the excitation of the array elements comes from the wave travelling along the microstrip line. In fact, a LWA radiates in a similar way as a linear array, creating a fan beam at an angle, making it possible to scan the beam by controlling the phase progression between the elements. LWAs are associated with frequency scanning whereas phased arrays are mostly used for electronic scanning. In this chapter, both points of view and applications are considered.

Two arrays are presented as proofs of concept: Section 3.1 deals with the study of a simple travelling-wave array built as the concatenation of several equal radiating elements, in order to show how the array performance can be predicted with the available theory and prove full-space frequency scanning capability, and Section 3.2 analyses the performance of a similar array that has been modified to incorporate phase shifters between the elements and carefully designed to allow electronic reconfigurability.

3.1 FULL-SPACE FREQUENCY-SCANNING ARRAY

Leaky-wave antennas (LWAs) have features such as frequency-scanning that have already been proven and extensively used in radar, MIMO, RFID systems, etc. Although the first examples of LWAs in planar technology were proposed in the literature many years ago [24, 25], the field of LWAs in this technology has been little developed until very recently. The limited applicability of these LWAs was due to a special phenomenon that takes place at broadside, traditionally known as *open-stopband* [26], which leads to a significant drop in the radiation power and an increase in the reflection coefficient. The experienced problem for this narrow angular region made LWAs unsuitable for continuous scanning from backward to forward, until the appearance of the CRLH LWA [4], which overcomes this drawback. In recent years, thanks to the intensive research into metamaterials, LWAs have experienced a renewed interest and many examples of LWAs in planar technology have arisen [27]. The broadside issue has been studied deeply and recent advances show that continuous scanning is achievable, not only for the CRLH LWA (Section 3.1.3). The connection between metamaterials and LWAs is consequence of the periodicity of both structures and the common interest in the phase constant, which is the key parameter in both fields. In fact, artificial transmission lines that had significant radiation losses have been considered as LWAs. Since the complementary strip-slot was initially conceived as unit-cell for artificial transmission lines, the application of the strip-slot in building a LWA is doubly justified.

On the other hand, in the few examples of microstrip series-fed slot linear arrays that appear in the literature, single-frequency shaped-beam, instead of frequency-scanning, has been pursued [11, 12], due to the bandwidth limitation imposed by the resonant nature of the slots. Since the complementary strip-slot overcomes this drawback, a microstrip-fed slot array with frequency scanning performance based on this element

results interesting from a research point of view.

In this section, a TWA, built as the concatenation of several strip-slot elements, is analysed. The goal is to use the method of analysis of LWAs to predict the behaviour of the array. For this purpose, the LWA theory is briefly reviewed first. Then, the capabilities of the array built with the complementary strip-slot element are explored. Special attention is paid to the radiation at broadside, in order to achieve full-space frequency scanning.

3.1.1 Theory Review

Leaky waves are travelling waves that leak out power gradually as they propagate along a waveguiding structure. This leakage takes place when the wave is faster than the velocity of light ($v_p > c$ or $\beta < k_0$, where k_0 is the free space wavenumber and β is the phase constant of the waveguiding structure). The region of the dispersion diagram where the condition $-k_0 < \beta < k_0$ is satisfied is called the *radiation cone* or *radiation region*. Therefore, it can be stated that a leaky-wave structure is any waveguiding structure whose dispersion curve penetrates the radiation region.

There are two categories of leaky-wave structures: uniform and periodic. Uniform leaky-wave structures maintain the cross section invariant along the direction of propagation and radiation happens due to its dominant mode, which is a fast wave. In these antennas, since β is positive, only forward angles can be obtained. On the other hand, periodic leaky-wave antennas consist of a slow-wave transmission line that has been periodically loaded by a discontinuity. Thanks to this periodicity the modal field takes the form of a Floquet-wave expansion in terms of the space harmonics (see Appendix D for a more detailed explanation). The structure will then leak power when one of the space harmonics is within the fast-wave region, where β_m is the phase constant of the harmonic m given by

$$\beta_m = \beta_0 + \frac{2\pi}{p}m \quad m = 0, \pm 1, \pm 2, \dots \quad (3.1)$$

where β_0 stands for the fundamental phase constant and p for the pitch of the structure.

In case of radiation, β determines the angle θ_{MB} of the main beam measured from

broadside following the simple relationship

$$\theta_{MB} \approx \arcsin(\beta/k_0), \quad (3.2)$$

which coincides with that derived by applying array theory. This formula is an approximation for small α (leakage factor) and assumes isotropic radiating elements. It is evident that in a structure with frequency dispersion (β is a nonlinear function of frequency), the pointing angle changes with frequency and frequency scanning is possible.

In the case of periodic leaky-wave antennas, the dominant mode is a slow wave, but backward radiation can be achieved, in addition to forward, using a negative space harmonic (usually the $m = -1$). However, as previously stated, a phenomenon caused by the coupling of spatial harmonics occurs at broadside, which traditionally prevented the radiation in this angular region. Recent advances have overcome this limitation, as will be detailed in Section 3.1.3.

3.1.2 Linear Array Based on the Strip-Slot Element

A microstrip line periodically loaded by strip-slot elements is proposed here as a TWA with scanning capabilities. An analysis of a microstrip loaded by five strip-slot elements with the geometry of Prototype 2 (see Section 2.4.1) separated by $p = 10$ mm and terminated by matched load is carried out next using full-wave electromagnetic simulations and measurements. Although the Floquet theory is stated for infinite periodic structures, it has been applied here, since the knowledge of the dispersion curves in these TWAs allows an easy determination of the number of radiating beams and of their respective angles of radiation. Only five elements have been cascaded, since the radiation efficiency of a single element is around 25 %. Fig. 3.1 shows the manufactured array.

The distance between elements p determines the phase constant of the unit-cell and, then, the radiation performance. Therefore, for the selection of the pitch p , several considerations have been taken into account. Firstly, the purpose was to achieve full scanning, from backward to forward angles, with a single beam. Therefore, it was assured that only one space harmonic was within the radiation region at a frequency. Secondly, to guarantee high radiation efficiency, the frequency at which the first space harmonic crosses the air line has been set above the resonance frequency of

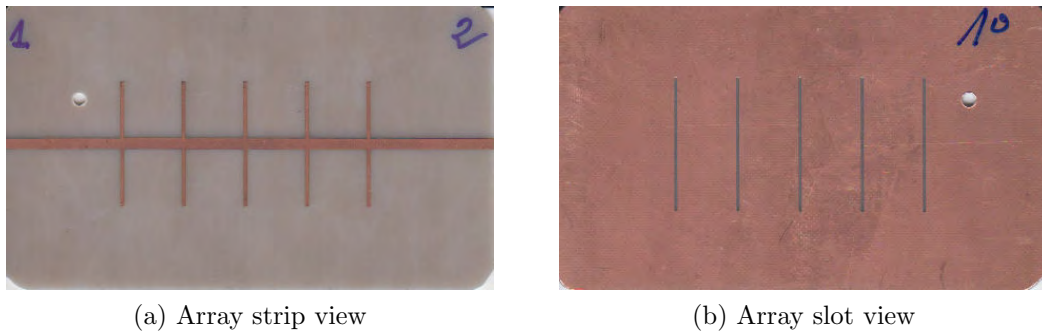


Figure 3.1: Photographs of the manufactured travelling-wave array.

the slot, from which the element starts radiating efficiently. And, finally, the broadside direction has been set so that it does not coincide with the frequencies at which the image impedance of a single element (without transmission line sections) has an asymptotic behaviour (see Fig. 2.19), which is around the resonance frequencies of the slots (5.4 GHz for this element). This last condition will be justified in Section 3.1.3.

It must be pointed out that the availability of a broadband radiating element makes the design very flexible and allows certain design decisions that are not possible with a resonant element. In the proposed array, the radiating element is first designed and then the pitch is chosen for the best performance. With a resonant element, the pitch cannot be selected independently of the element, since its impedance bandwidth must coincide with the radiation band of interest.

The resulting phase constants of the different spatial harmonics (according to D.6) multiplied by the structure pitch p are shown in Fig. 3.2, together with the air line (k_0p). It can be observed that, over the 1-16 GHz range, two spatial harmonics enter the fast wave region, limited by the air line: harmonics $m = -1$ and $m = -2$. Moreover, only one spatial harmonic is within the radiation region at a frequency, therefore, single beam radiation is expected. For these harmonics, the main beam angles, according to (3.2) are depicted in Fig. 3.3. It is highlighted that the main angle theoretically scans from backfire ($\theta_{MB} = -90^\circ$) to endfire ($\theta_{MB} = 90^\circ$), due to the dispersive nature of the phase constant. The broadside direction corresponds to 6.2 and 14.1 GHz. Therefore, there are two bands with beam scanning.

In order to check that the array radiates in the predicted bands, Fig. 3.4 shows the simulated radiation efficiency with HFSS for the whole bandwidth studied. It can be observed that the bands at which the spatial harmonics are within the fast wave region correspond to higher radiation efficiencies, thus confirming the prediction. Moreover, it

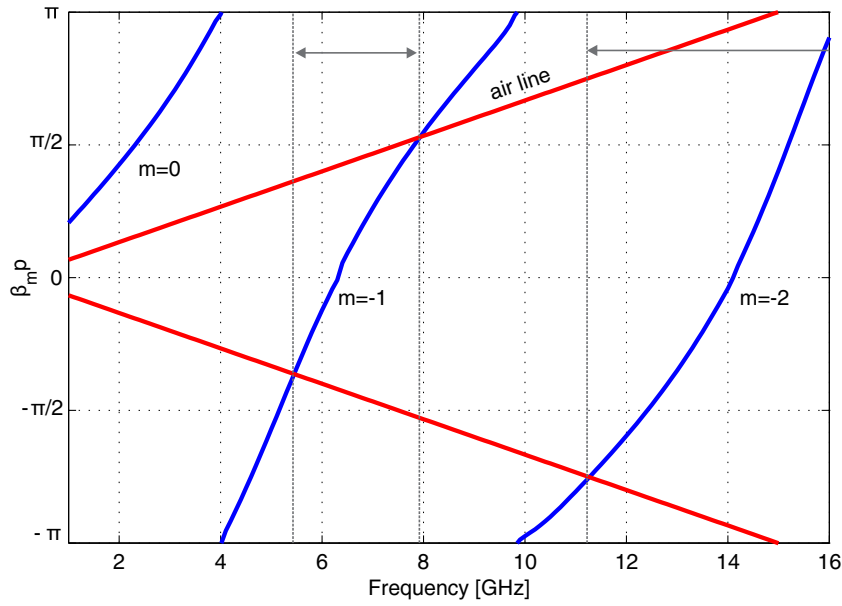


Figure 3.2: Phase constants of the spatial harmonics multiplied by the structure pitch p for the analysed five-element array. The air line is depicted as a red line, as well.

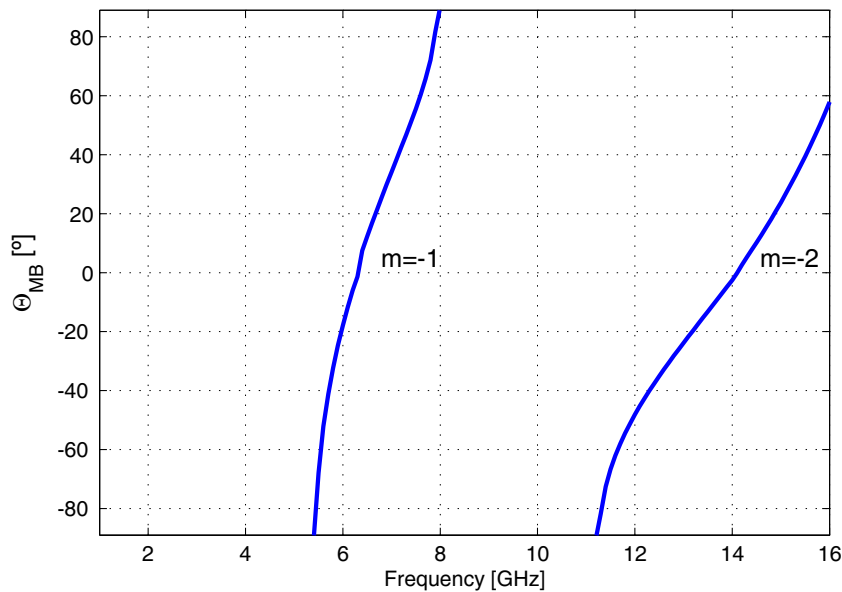


Figure 3.3: Main beam angle for the analysed five-element array according to (3.2).

can be seen that the radiation efficiency drops a small quantity at broadside, attributed to the open-stopband effect, but it still remains high. This means that in this structure, the broadside effect is not so critical as in other structures, thanks to the topology and good matching of the unit-cell.

Fig. 3.5 shows the reflection coefficient comparison between the measurement and the simulations (with HFSS and ANSYS Designer) of the manufactured array. Good agreement is obtained between the three curves. In the radiating bands, the structure

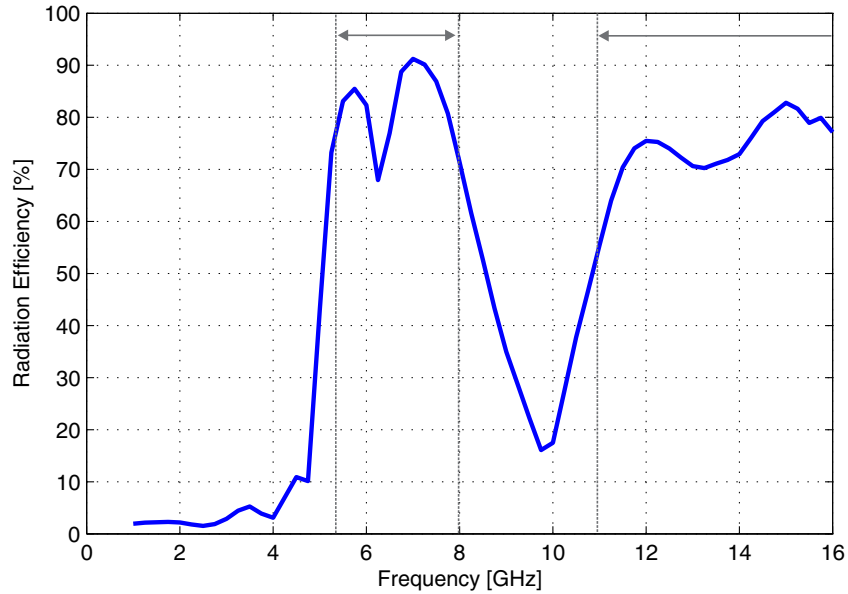


Figure 3.4: Radiation efficiency versus frequency for the analysed five-element array.

is well-matched, except for the maximum in the $|S_{11}|$ found at broadside, as expected. The multiband behaviour is possible thanks to the broad matching of the element.

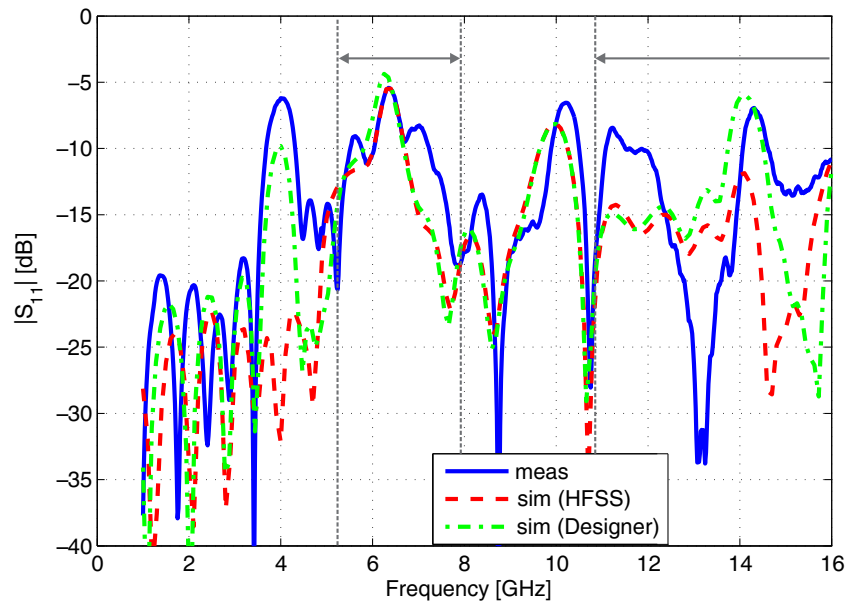


Figure 3.5: Comparison of the $|S_{11}|$ of the proposed travelling-wave array between measurement and simulation (with HFSS and ANSYS Designer).

In order to verify whether the array carries out the predicted frequency scanning, Fig. 3.6 shows the radiation patterns (measurement¹ and simulation) in the plane longitudinal to the microstrip (xz -plane) obtained for the array at different frequencies

¹The radiation measurements were taken in the anechoic chamber of the Laboratorio de Ensayos y Homologación de Antenas, Universidad Politécnica de Madrid, Madrid (Spain).

within the radiation band of the spatial harmonic $m = -1$ (from 5.5 to 7.9 GHz, approximately). Excellent agreement is obtained between the simulations and measurements. The scanning behaviour can be observed, where the main beam goes from backward to forward directions in both half-spaces, although more radiation goes into the slot half-space, as so radiates the element. The broadside direction corresponds to around 6.3 GHz, as predicted in Fig. 3.3. No beam degradation is found at broadside, unlike in most LWAs, which also confirms that the open-stopband effect is not so critical in this antenna. Since the proposed element is not isotropic, a noticeable shift between the direction of the beams obtained with electromagnetic simulation and those predicted in Fig. 3.3 with (3.2) is observed. This difference is more emphasized for angles near backfire and endfire, where the element barely radiates. The slight modification in the beam shape for 6.7 GHz can be also attributed to the combination of the array factor and the radiation pattern of the element, which is not frequency-independent either.

Likewise, Fig. 3.7 shows the obtained radiation patterns at frequencies within the radiation band corresponding to the spatial harmonic $m = -2$ (which goes from 11.3 GHz to further than 16 GHz). The frequency scanning at these upper frequencies is also observable, where $f=14.2$ GHz corresponds to broadside, as Fig. 3.3 also indicates. In this case, more radiation goes into the strip half-space and the beamwidth is smaller, as it must be for higher frequencies.

Fig. 3.8 shows the measured maximum gain over the two radiating bands. The obtained values for gain are reasonable for an array of only five elements. This gain could be increased if a longer array were built.

3.1.3 The Broadside Issue

The phenomenon of the open-stopband at broadside has been extensively studied in the literature, especially in recent years [27]. This effect occurs due to the coupling of a pair of spatial harmonics in the radiating region. Techniques based on circuit theory have recently been proposed to overcome this limitation [28, 29]. Therefore, in this subsection, the broadside problem is tackled from a circuit point of view.

For broadside radiation, $\beta p = 2\pi$ is required, which makes all the reflections from the discontinuities (radiating elements) be added in phase to the source. As a consequence, mismatching is obtained, which degrades the radiation performance. In an infinite periodic structure with a symmetrical cell, the input impedance of the antenna

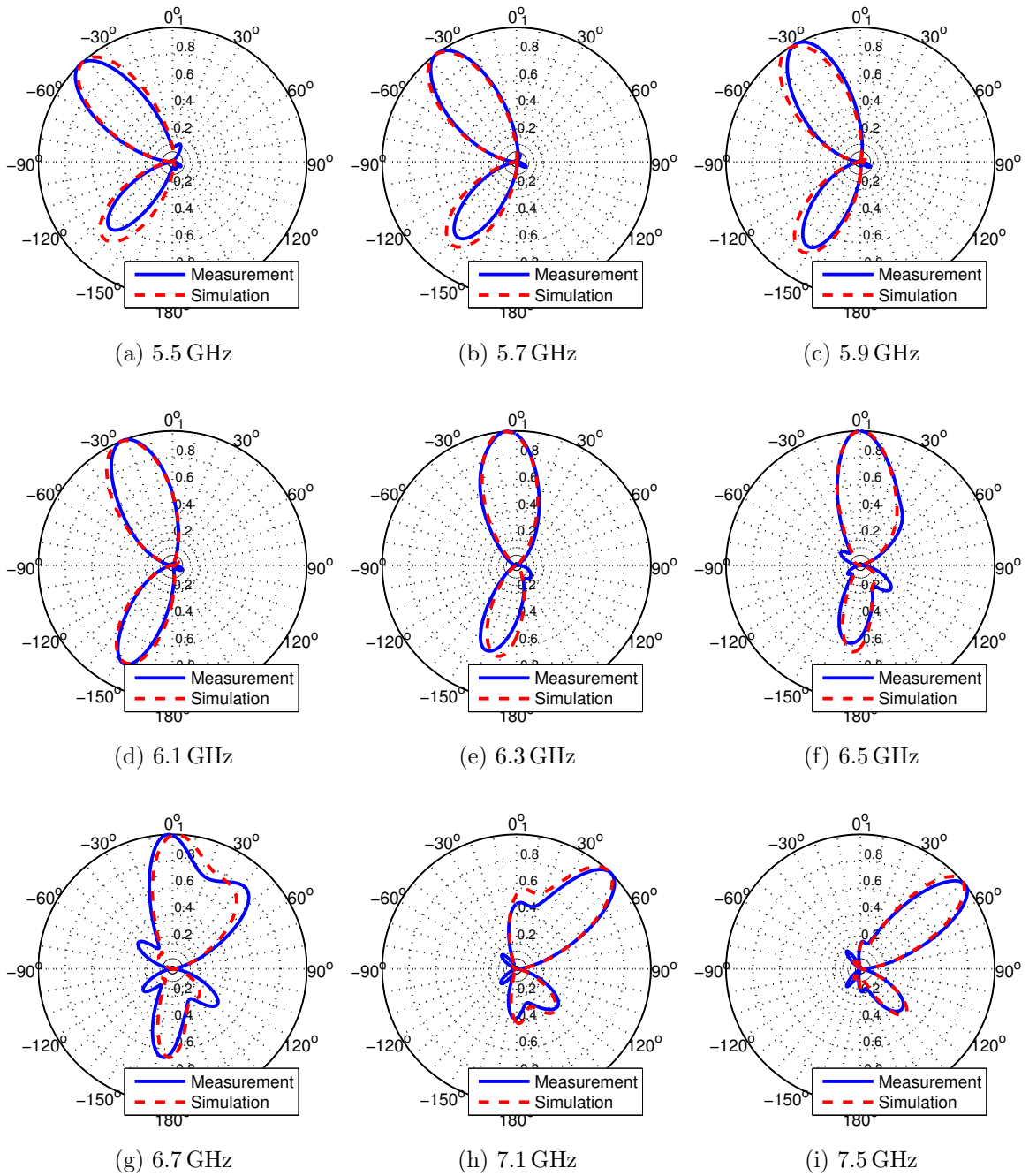


Figure 3.6: Measured and simulated radiation patterns of the travelling-wave array at different frequencies over the first radiation band.

at the source is the image impedance of the unit-cell. Therefore, the input reflection coefficient of the antenna is given by

$$\Gamma_{in} = \frac{Z_{im} - Z_0}{Z_{im} + Z_0}. \quad (3.3)$$

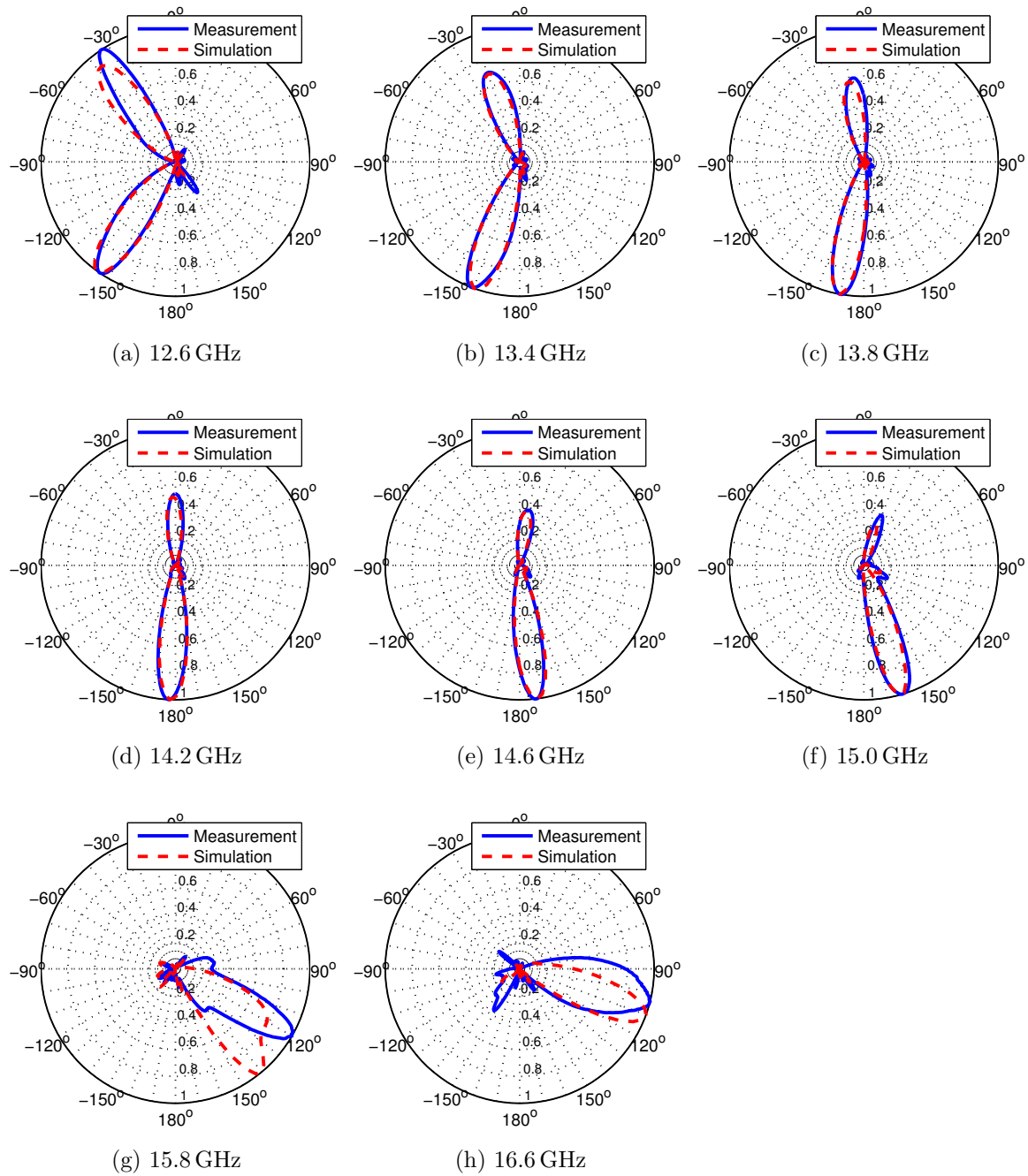


Figure 3.7: Measured and simulated radiation patterns of the travelling-wave array at different frequencies over the second radiation band.

Then, the proposed techniques to mitigate the broadside effect consist in matching Z_{im} to Z_0 at broadside.

In [29], the authors proposed an equivalent circuit for an arbitrary unit-cell of leaky-wave antennas consisting of a lattice network with a series LC-resonator in the series branch and a shunt LC-resonator in the cross branch. From it, two conditions

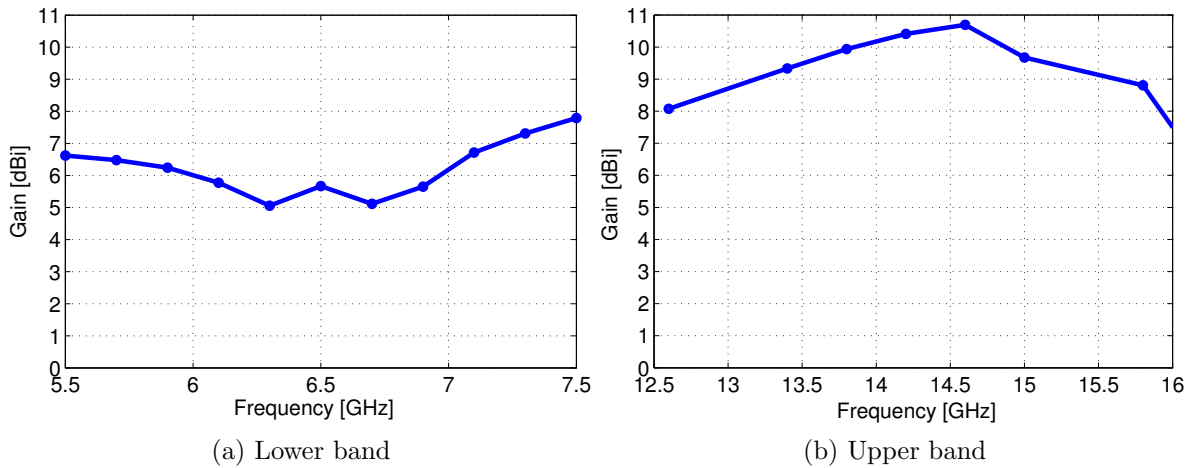


Figure 3.8: Measured maximum gain of the travelling-wave array over the two radiation bands.

were extracted for good radiation at broadside: frequency balancing and Q-balancing. Frequency-balancing is required for achieving a frequency-constant image impedance when losses are considered negligible. Then, frequency balancing means making the resonance frequencies of the two resonators equal. Q-balancing pursues the same objective, but takes losses into account.

If the immittances of the lattice network Z_a (series branch) and Y_b (cross branch) are defined as follows:

$$Z_a = R + jX \quad (3.4a)$$

$$Y_b = G + jK \quad (3.4b)$$

and it is known that the propagation factor of a lattice is given by

$$\gamma p = \operatorname{acosh} \left(\frac{1 + Z_a Y_b}{1 - Z_a Y_b} \right) \quad (3.5)$$

then, it is straightforward to check that for broadside $X = 0$ and $K = 0$ or, equivalently, $Z_a = R$ and $Y_b = G$ and then

$$Z_{im} = \sqrt{\frac{R}{G}} \quad (3.6)$$

which forces the losses to be controlled to obtain good matching at broadside.

At the frequency at which $X \rightarrow \infty$ and $K \rightarrow \infty$, the image impedance is given by

$$Z_{im} = \sqrt{\frac{X}{K}} \quad (3.7)$$

which, due to the frequency-balancing condition, is frequency-independent and must set the required impedance level for good matching.

From 3.6 and 3.7, it can be concluded that the condition for good matching is that

$$\frac{R}{G} = \frac{X}{K} \text{ or } \frac{R}{X} = \frac{G}{K} \quad (3.8)$$

which was called the Q-balancing condition [29].

However, all the previous statements are valid only because the broadside ($\beta p = 2\pi n$) coincides with $X = 0$ and $K = 0$ in the proposed equivalent circuit. In the case of the antenna with strip-slots, the unit-cell is the concatenation of the microstrip line sections with the strip-slot (modelled itself as a lattice network). Therefore, the interconnecting microstrip sections add phase to that provided by the lattice network. Consequently, the image impedance of the total unit-cell will differ from that shown in Fig. 2.19, which corresponds to the strip-slot with coincident reference planes (i.e. without taking into account the microstrip line sections). Accordingly, in this case, the phase constant of the total unit-cell will be 2π when the contribution of the microstrip sections together with the lattice network is 2π , which will generally not coincide with a propagation factor $\gamma = 0$ in the lattice. As a result, the image impedance of the total unit-cell at broadside will not depend exclusively on the losses of the lattice branches, as in the previous case, which might make the matching easier.

In order to see how the microstrip line sections modify the image impedance of a two-port circuit, Fig. 3.9 shows the Z_{im} of a purely-resistive symmetrical lattice network with image impedance Z_{im}' surrounded by two microstrip accessing sections. βp stands for the propagation factor of the total unit-cell. It can be observed that the image impedance of the total unit-cell depends on the propagation factor, with the worse case for the corresponding reflection coefficient when $\beta p = n\pi$. It is then important to match the image impedance of the unit-cell at the frequency when $\beta p = 2\pi$, if good matching is desired at broadside. For this purpose, the selection of the pitch p is important, since the broadside frequency depends on p and the image impedance of the strip-slot is also frequency-dependent. If it were possible to cascade the strip-slot elements without microstrip line sections ($p = 0$), the broadside frequency would correspond to the second resonance frequency of the slot (around 10.2 GHz), at which the image impedance has an asymptotic behaviour and the imaginary parts of the immittances in the lattice would be zero, as in (3.6). Therefore, the image impedance would depend exclusively on the losses. This fact, together with the effect at broad-

side, would lead to an unfavorable situation. However, the necessary introduction of microstrip line sections to cascade the radiating elements is advantageous, since it allows the broadside frequency to be set outside of these unstable frequencies of the image impedance of the strip-slot. Fig. 3.10 illustrates the change in the reflection coefficient of an infinite periodic structure with strip-slots (according to 3.3) through adding microstrip line sections (in this case $p=10$ mm, which is the selected value). The solid blue curve corresponds to the hypothetical case of an infinite structure with the unit-cell as the two-port obtained from the strip-slot with coincident reference planes (not implementable in reality) and the red dashed curve, an infinite structure built with the strip-slot with microstrip line sections. The reflection coefficient improves several dB by moving the broadside frequency to a more favourable frequency for the image impedance of the strip-slot. This is why the broadside effect is not so critical in the proposed structure, in which 6.2 GHz was selected as first broadside frequency, which corresponds to $p=10$ mm, as previously stated.

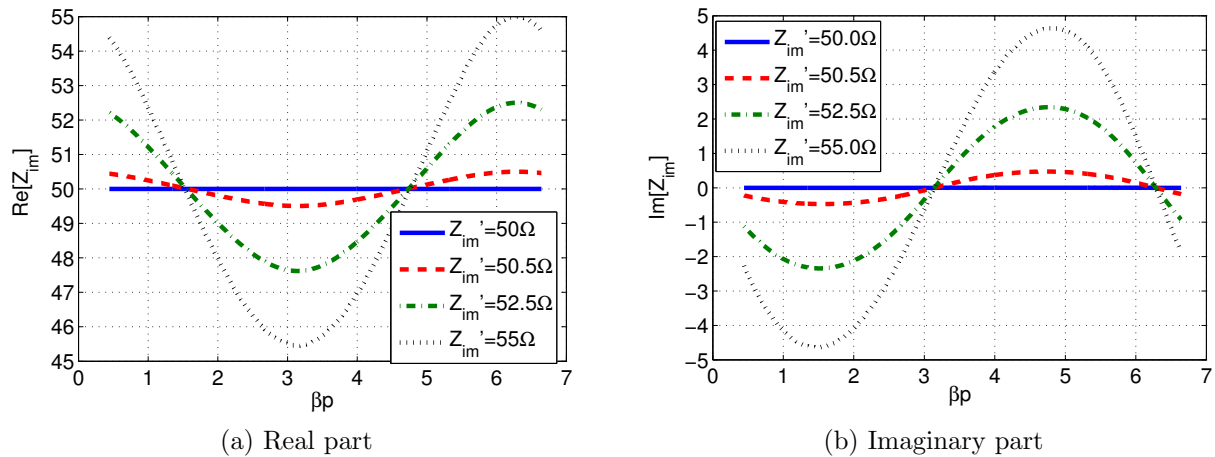


Figure 3.9: Image impedance of the resulting section of a resistive symmetrical lattice network with Z_{im}' with a transmission line section at each port. The total propagation factor is βp .

Mitigation of the Broadside Effect with a Matching Network

In [28], the use of matching networks to mitigate (or even suppress) the broadside effect was demonstrated. The authors proposed the use of classic input matching networks, like the quarter wave transformer or the single matching stub, to be added to the unit-cell of LWAs, in order to make the input impedance of a single unit-cell equal to Z_0 at the broadside frequency.

It is evident that if the LWA is terminated by a matched load Z_0 and Z_{in} of a

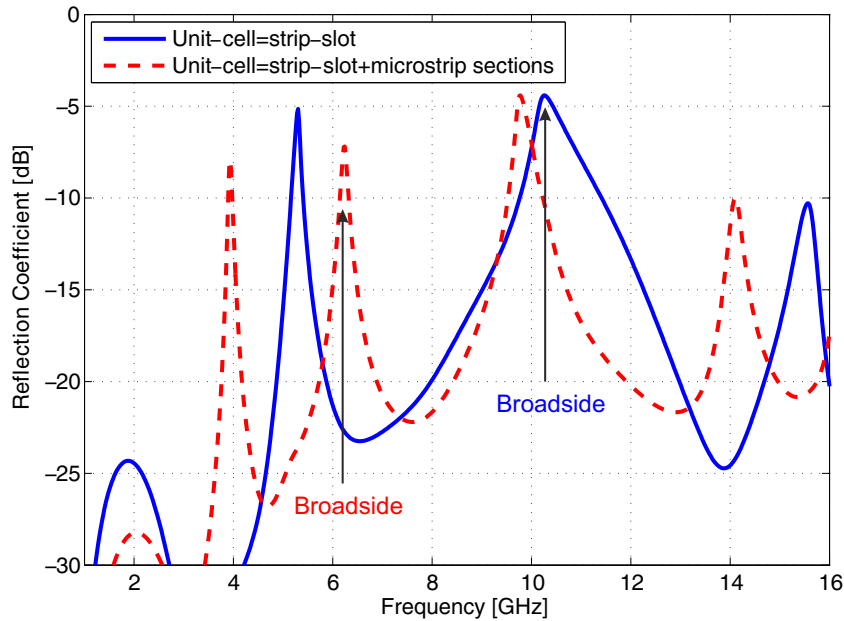


Figure 3.10: Comparison of the reflection coefficient for an infinite periodic array with strip-slots for two different pitch values. The solid blue curve corresponds to the hypothetical case of an array with no microstrip line sections ($p = 0$) for interconnecting the elements and the red dashed curve corresponds to the manufactured array ($p = 10$ mm).

Z_0 -loaded unit-cell is Z_0 at a frequency, then the reflection coefficient at the input of the antenna will be zero and perfect matching at the input will be obtained at this specific frequency.

The implementation of this technique in the proposed array can be seen in Fig. 3.11. For dimension restrictions, the chosen matching network has been the delay line with single stub. The input impedance when loaded with Z_0 has been obtained from electromagnetic simulations. Then, the lengths of the delay line and the stub have been calculated in order to match the input impedance at the broadside frequency (6.2 GHz) with Z_0 . No further optimizations have been carried out, therefore the matching is not perfect at broadside, but it has improved with respect to the original array, as can be seen in Fig. 3.12.

However, the problem of this matching technique is that it is narrowband and strongly frequency-dependent, which leads, for instance, to a worsening of the reflection coefficient over the second radiation band and degradation around the second broadside. Therefore, for a dual-band or relatively wideband array, it is definitely not a good solution.

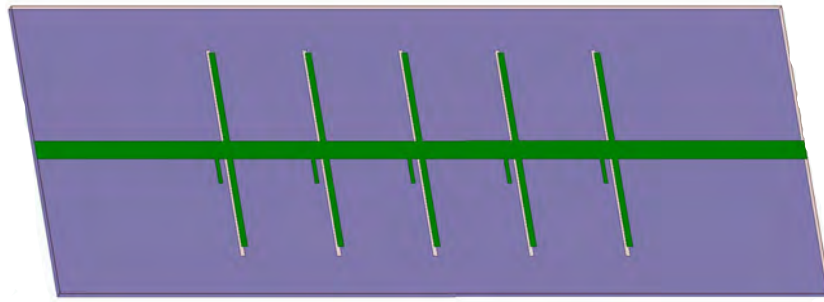


Figure 3.11: Layout of the array with single stub matching network.

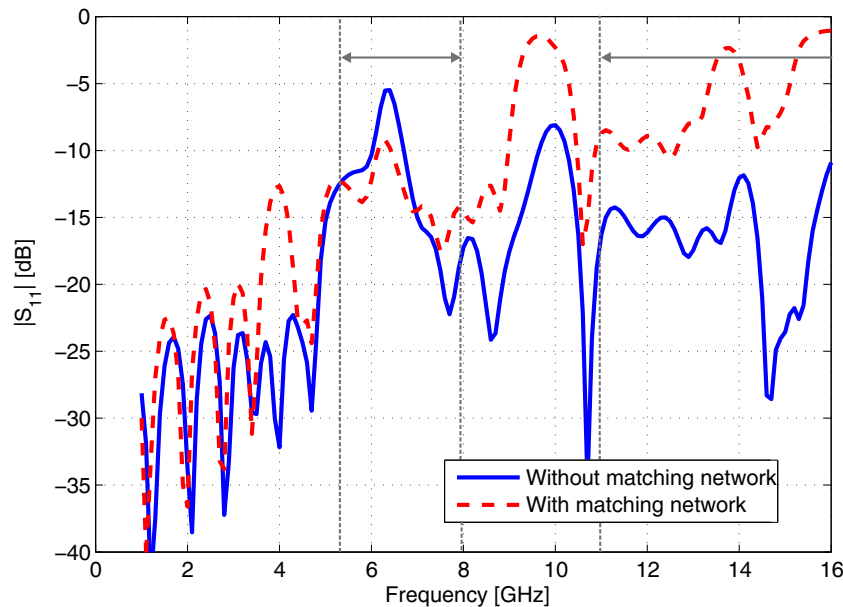


Figure 3.12: Comparison of the simulated $|S_{11}|$ between the original array and the array with matching network.

Mitigation of the Broadside Effect Through a Misalignment of the Element

By introducing a small misalignment between the slot and the strip along the direction of the microstrip line, a slight modification in the reflection coefficient is obtained, since the structure is made asymmetrical. The layouts of the unit-cell or array element with aligned and misaligned strip-slots are shown in Fig. 3.13. The effect of this misalignment has been studied by using the electromagnetic simulator. Fig. 3.14 plots the $|S_{11}|$ of a single strip-slot for different values of misalignments. It can be observed that certain resonances appear when the structure is slightly asymmetrical without significantly compromising the good matching for the rest of frequencies. Advantage of this effect has been taken to mitigate the broadside mismatching of the proposed TWA.

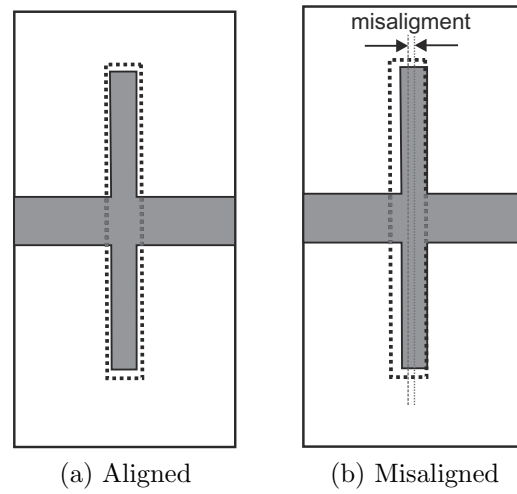


Figure 3.13: Layouts of the aligned and misaligned strip-slot elements.

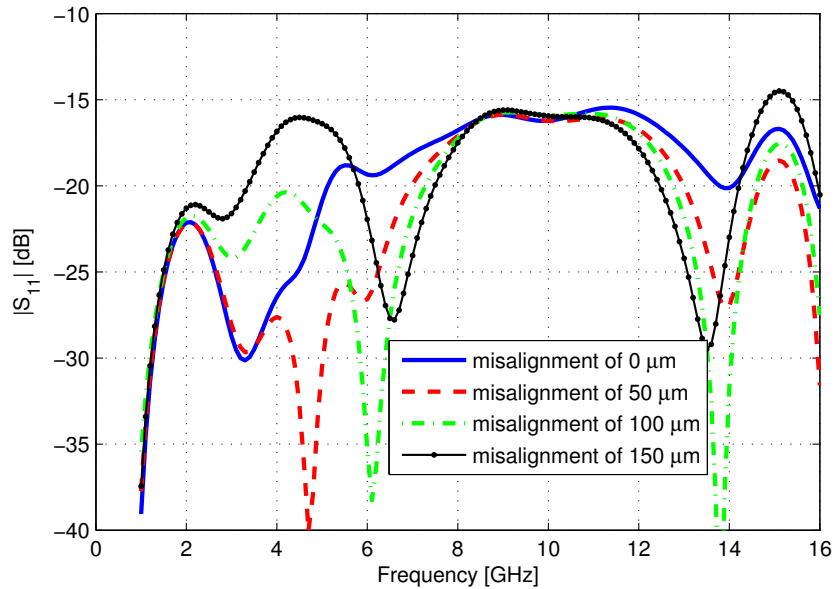


Figure 3.14: Comparison of the simulated $|S_{11}|$ of the radiating element with different misalignments.

In order to improve the broadside mismatching of the initial array, a misalignment of $150\ \mu\text{m}$ has been introduced into all the elements, shifting the slot to the input port of the antenna. This value has been chosen according to the simulations to obtain the smallest reflection coefficient at the broadside frequency ($6.2\ \text{GHz}$). This misalignment represents almost a 30% of the total shift that would lead to alternate strip-slot (with no area superimposed).

The array with misaligned elements has been manufactured. Although the accuracy of the available technology has not allowed the misalignment to be set exactly to the

desired level, it is near enough to prove the concept. Fig. 3.15 shows a comparison of the measured $|S_{11}|$ between the array with aligned elements and the array with misaligned elements. The improvement in the reflection coefficient at broadside is manifest, while it maintains the good value over the remaining frequencies of the radiating bands. Fig. 3.16 shows the comparison of the $|S_{11}|$ between measurement and simulations with good agreement.

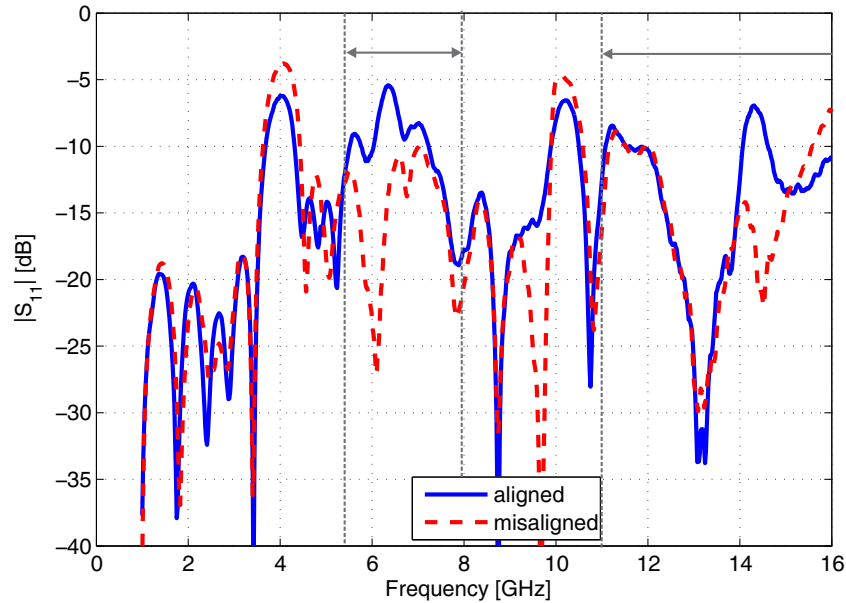


Figure 3.15: Comparison of the measured $|S_{11}|$ between the aligned and the misaligned strip-slot array.

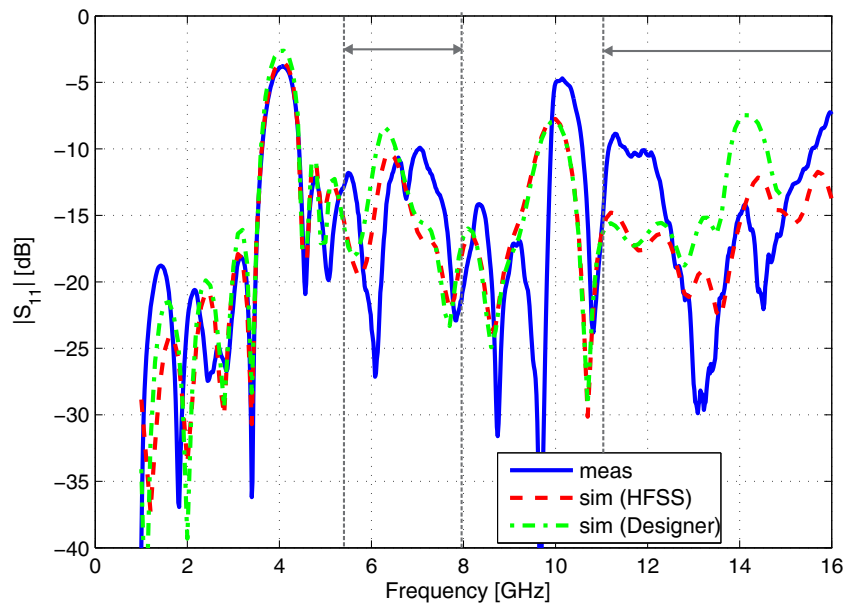


Figure 3.16: Comparison of the $|S_{11}|$ between measurement and simulations for the misaligned strip-slot array.

The radiation pattern does not change through the introduction of the misalignment, since the radiating source (mainly, the slot) is not modified, but the radiation efficiency does. This is shown in Fig. 3.17. An increase in the radiation efficiency around the two broadside frequencies (around 6.2 and 14.1 GHz) is noticeable, which confirms the mitigation of the broadside open-stopband effect.

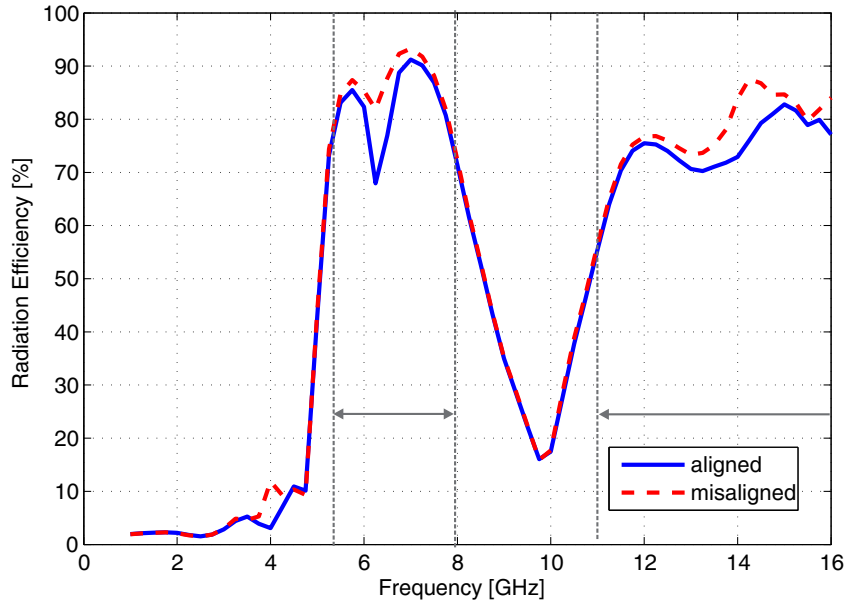


Figure 3.17: Comparison of the simulated radiation efficiency between the aligned and the misaligned strip-slot array.

It is worth mentioning that, very recently, a paper has been published which proposes the introduction of transversal assymetry in the unit-cell of LWAs to equalize the radiation efficiency and the image impedance through broadside [30]. The concept behind it is the same as the applied here: taking advantage of the extra degree of freedom (the misalignment or assymetry) to improve the reflection coefficient of the unit-cell at broadside. Therefore, it is pointed out that the concept is extendable to other unit-cell structures.

3.2 ELECTRONICALLY RECONFIGURABLE ARRAY

Reconfigurability is currently a key feature in the field of antennas for its many applications, such as in satellite and mobile communications [31, 32], digital television broadcasting [33] and even wearable fabric applications [34]. Specifically, the control of the beam direction can lead to two demanding features: electronic beam steering,

which allows the radiation direction to be pointed at a desired angle at a single frequency, and frequency tunability, which means maintaining the beam direction over a range of frequencies.

For beam reconfigurability, series-fed microstrip arrays have been extensively used due to the advantages of planar technology and series feeding. Thanks to the phase shift provided naturally by the feed microstrip line, phase shifters with less phase range than in corporate feeding can be used. The phase shifters are designed to provide scanning from backward to forward angles, thus covering a wide range of the space, which is demanded by applications. In [35], two microstrip antennas with beam control capability were presented: one based on loaded-line phase shifters and another one using reflective shifters. The solution with the latter provided a better performance, obtaining a wider range for the beam angle (around 60° centred at broadside), but with very narrow bandwidth. Some other solutions have been proposed using phase shifters based on tunable positive/negative refractive index (PRI/NRI) structures [36, 37]. These two designs were made for 2.4 GHz WLAN, but both shared a narrow bandwidth and angle range of less than 70° around broadside.

The narrow bandwidth of most of the works for electronic beam steering in microstrip technology is a consequence of the resonant impedance bandwidth of the microstrip conventional radiators, patches and slots. With these radiating elements, arrays with frequency reconfigurability must tune not only the feeding network but also the array element itself. This complexity is a serious limitation for frequency-tunable antenna arrays with fixed beam and is the reason for the relatively low number of publications on this topic. When a non-resonant element is used instead, the requirement of tuning the radiating element disappears and a simpler structure can be used. This is the approach of [38], where the radiating element is a non-resonant coplanar strip with phase reversal. Fixed-beam at broadside with frequency tunability over a relatively broad bandwidth was demonstrated by including some varactors. However, this array requires a balun for the structure feeding, not very advantageous for non-differential devices, and has a considerable length, N times $\frac{\lambda}{2}$, where N is the number of cells, which must be high for good radiation efficiency, due to the low leakage factor of the radiating element. Moreover, electronic steering was not considered.

With the aforementioned necessity of reconfigurability and the increasing demand of broadband services, a planar series array capable of both electronic steering and beam maintenance over broad bandwidth results very appealing. For this purpose, the complementary strip-slot element is an excellent candidate, due to its non-resonant

nature, series feeding and easy integration with shifting microstrip-based structures. Thanks to its broad matching, it can be used over broad bandwidth with no need to tune the radiating element.

In this section, the proposed TWA of 3.1.2 is extended to add reconfigurability properties by introducing varactor-based loaded-line phase shifters in order to allow the control of the radiation angle over relatively broad bandwidth. This array is designed for a lower frequency band, therefore, the geometry of the elements with respect to that of the array in Section 3.1.2 is modified. The capability of the antenna to maintain the main lobe angle through frequency and to steer it in a wide range at a given frequency is demonstrated. Competitive performance is obtained in terms of scanning range (up to 90° around broadside) and bandwidth (1.71-2.17 GHz) with this very simple structure.

3.2.1 Geometry

The proposed reconfigurable antenna consists of a TWA as the one introduced in 3.1.2 with phase shifters between the elements. The array is terminated in a matched load and the elements are aligned (no especial attention has been paid to mitigate the deterioration at broadside). To fit the length of the phase shifters to the distance between the radiating elements, d , microstrip lines are used. Fig. 3.18 shows the geometry of the proposed antenna, with four radiating elements, spaced a distance p , three phase shifters and the fit transmission lines between them. Their phase contributions are ϕ_e , ϕ_l and ϕ_m respectively.

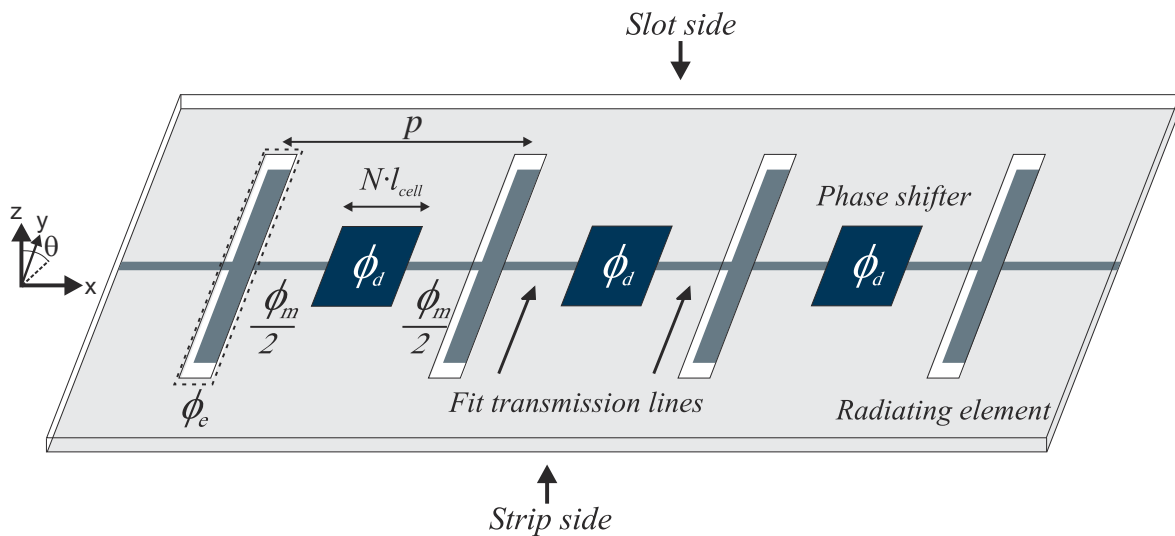


Figure 3.18: Schematic of the antenna and the used coordinate system.

For the phase shifter, simplicity and wide range of phase was pursued, while maintaining its size to a minimum. Thus, a phase shifter based on a transmission line loaded with lumped elements, as proposed in [39], was chosen. The loaded-line phase shifter consists of a periodically loaded high impedance microstrip line with N unit-cells, where Z_{hi} and v_{hi} denote the characteristic impedance and phase velocity for the unloaded line. The unit-cell of the phase shifter consists of a section of high impedance transmission with a physical length of $l_{cell} \ll \lambda$, in which a shunt load element is connected to the ground, as Fig 3.19 shown. The loading element is a variable shunt capacitor, $C(V_R)$, controlled by a DC feed, V_R , which acts as a reverse bias voltage. The shunt loading configuration allows the whole phase shifter to be controlled by this single DC signal. The variation in $C(V_R)$ is inversely proportional to V_R , having C_{max} for $V_{R_{min}}$ and C_{min} for $V_{R_{max}}$.

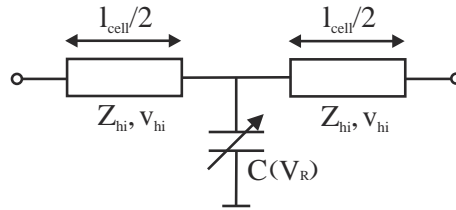


Figure 3.19: Phase shifter unit-cell.

3.2.2 Design Guidelines

Design equations for the phase shifter can be easily obtained following the analysis of periodic structures described in [40]. This structure has a low-pass response with image impedance, phase velocity and cut-off frequency given, when $l_{cell} \ll \lambda$, by

$$Z_{loaded}(V_R) = \sqrt{\frac{L_u}{C_u + C(V_R)/l_{cell}}} = \frac{Z_{hi}}{\sqrt{1 + \frac{C(V_R)/l_{cell}}{C_u}}} \quad (3.9)$$

$$v_{loaded}(V_R) = \frac{1}{\sqrt{L_u \cdot (C_u + C(V_R)/l_{cell})}} = \frac{v_{hi}}{\sqrt{1 + \frac{C(V_R)/l_{cell}}{C_u}}} \quad (3.10)$$

$$f_c(V_R) = \frac{1}{\pi \sqrt{L_u l_{cell} \cdot (C_u l_{cell} + C(V_R))}}, \quad (3.11)$$

respectively, where L_u and C_u are the inductance and capacitance per unit of length of the unloaded transmission line and $C(V_R)$ is the loading capacitance.

According to (3.9) and (3.10), $C(V_R)$ contributes to lower Z_{loaded} and v_{loaded} . From (3.10), it is possible to define the phase shift range given by a single unit-cell when the loading capacitance varies from its maximum to its minimum value as

$$\Delta\phi = \phi_{max} - \phi_{min} = \phi(C_{max}) - \phi(C_{min}) = \frac{2\pi f \cdot l_{cell}}{v_{loaded}(C_{max})} - \frac{2\pi f \cdot l_{cell}}{v_{loaded}(C_{min})}. \quad (3.12)$$

Equations (3.9)-(3.12) allow the proper design of the required phase shifter.

In order to estimate the main radiation direction of the array easily, θ , the equation from uniform arrays [41] can be used (which is equivalent to (3.2)):

$$\theta = \arcsin\left(\frac{\phi_t}{kp}\right), \quad (3.13)$$

where θ is defined in Fig. 3.18, k is the wavenumber of the air and the total phase shift between elements, ϕ_t , is the phase contribution of the radiating element, ϕ_e , the phase shifter, ϕ_l and the microstrip interconnecting sections, ϕ_m . Thereby,

$$\phi_t(f, V_R) = \phi_e(f) + \phi_d(f, V_R) + \phi_m(f). \quad (3.14)$$

The condition that ϕ_t must satisfy in order to achieve a theoretical full range of variation in θ (i.e. $-90^\circ \leq \theta \leq 90^\circ$) is that $\phi_t(V_R) - 2\pi n$ scans the interval given by $[-kp, kp]$, at a given frequency, where n will be referred to as the array period, which is equivalent to the index (except for a change in the sign) of the radiating spatial harmonic in Floquet's terminology.

Therefore, given a contribution of ϕ_e and ϕ_m at a single frequency, the shift introduced by the phase shifter itself (depending only on V_R) must be wide enough to cover this range.

Since there are many variables (each other dependent) that determine the pointing angle, a general example is analysed, in order to illustrate the importance of the selection of the number of cells for the phase shifter, when the pitch period is fixed. Fig. 3.20a plots ϕ_t versus frequency in a general case, where d has been already fixed. The limits given by the condition of full-space beam scanning are shown in solid red. The dashed lines represent ϕ_t over frequency when V_R is tuned to provide a minimum and a maximum value for the capacitance $C(V_R)$ for an N -cell phase shifter. There is a frequency range, BW_1 , over which the antenna is able to steer the main beam in the

whole angle sweep, considering the first period of the array factor. This bandwidth is determined by the range of ϕ_t , limited by C_{max} and C_{min} , contained within $-kd$ to kd . The dotted lines in Fig. 3.20a correspond to an $N + m$ cell phase shifter. As can be seen, its bandwidth, BW_2 , is wider than BW_1 because of a higher phase shift range. However, it must be pointed out that the initial and final frequencies of the bandwidth depend on the length of the interconnecting microstrip lines (ϕ_m). If d is fixed and the number of cells of the phase shifter is increased, the length of the interconnecting microstrip lines decreases in order to include more cells in the phase shifter, thus changing ϕ_m . Therefore, although a wider bandwidth is achieved with a higher number of cells in the phase shifter, this number must be chosen carefully to fulfil the specified frequency range.

Once the phase shift ϕ_t is known for a given range of frequency and a certain reverse bias voltage, θ can be evaluated. To do this, equation (3.14) is included in the expression for the main beam direction of an array with uniform amplitude feeding, leading to

$$\theta = \arcsin \left(\frac{\phi_e + \phi_d + \phi_m - 2\pi n}{kd} \right). \quad (3.15)$$

Equation (3.15) is an approximation whose validity is evaluated in later simulations and measurements.

Following with the general case of Fig. 3.20a, Fig. 3.20b shows θ versus V_R for different frequencies belonging to the case of N cells in Fig. 3.20a (C_{max1} and C_{min1}). The five frequencies of Fig. 3.20b have been marked as P1-P5 in Fig. 3.20a. The lower frequency corresponds to the light blue dash-dot-dot line (P1) and frequency increases to the right. In Fig. 3.20a, it can be observed that P2, P3 and P4 are within the bandwidth for full scanning (BW_1) and, accordingly, full scanning is achieved in Fig. 3.20b for these three frequencies. The periodicity of the array factor can be observed in the black solid curve (P5), where almost the whole range of θ can be achieved, but not with a continuous tuning of V_R . For high values of θ , low V_R is required, which is not convenient, since the varactor presents higher losses for low V_R and high frequencies. Consequently, for high frequencies, high values of V_R are desirable to minimize the losses. The number of cells of the phase shifter is then a design variable to control the location of the curves of Fig. 3.20b, as it was illustrated in Fig. 3.20a.

If the size of the antenna is a constraint, a trade-off between directivity, beam direction range and size must be taken. Small spacing between elements leads to low directivity and leaves little space for the phase shifter unit cells, which reduces the

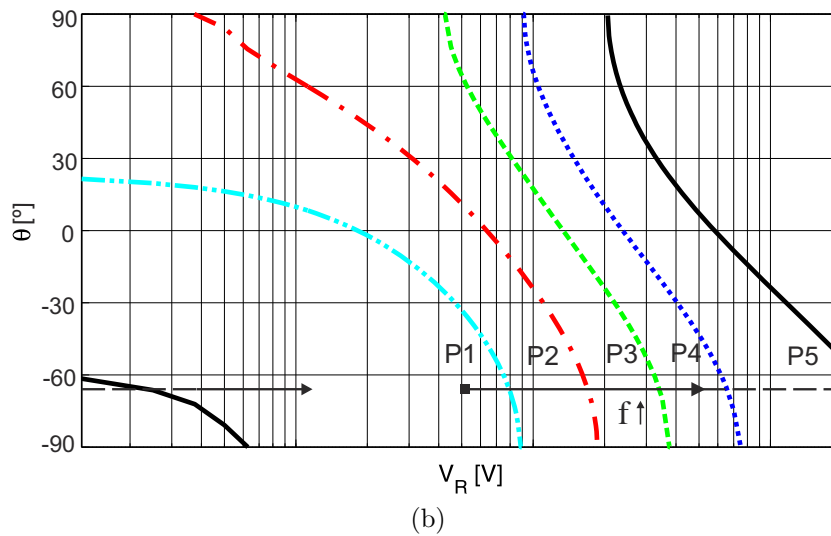
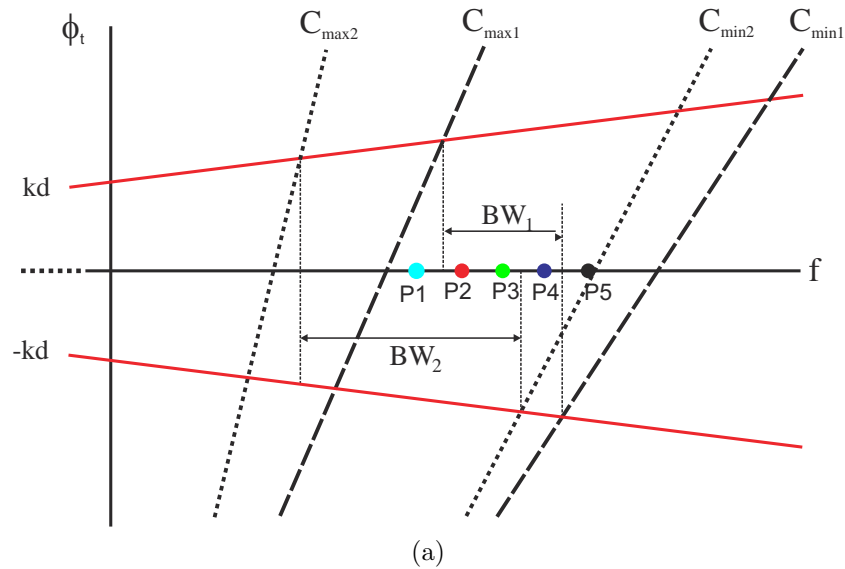


Figure 3.20: (a) An example of ϕ_t as a function of frequency and varactor capacitance for two phase shifters with different number of cells. (b) θ as a function of frequency and reverse bias voltage for the five frequencies marked in figure (a).

achievable phase shift range. An increase in d has the opposite effect. The drawback of a higher value of d is that the required range to achieve full beam scanning is increased.

It is evident that the fulfilment of the condition for full beam scanning also depends on the contribution of the phase shift of the radiating element. Therefore, the geometry of the element must be chosen in accordance to the requirements of the total phase range.

3.2.3 Design Proposal

A design example of the proposed array has been carried out for the LTE band from 1.71 to 2.17 GHz with four radiating elements. Electronic scanning and frequency re-configurability are aimed to be demonstrated with simulation and experimental results over this bandwidth. The chosen substrate for the design is the GIL 1032.

For the design of the element, good matching and a radiation efficiency better than 30% have been pursued over the design bandwidth. This latter specification is imposed in order to have good radiation efficiency in the array with only four elements. Therefore, the widths and lengths of the slot and the strip have been chosen with these two criteria. From all the pairs of widths that achieve a $50\ \Omega$ impedance level, the one that provides better radiation efficiency has been chosen. Moreover, the lengths of the strip and slot have been adjusted to have the same electrical lengths, thus achieving constant impedance behaviour according to (2.4), and with the requirement that the resonant frequency associated to the slot is below the design bandwidth (to make the element efficient in terms of radiation). In this way, the strip and slot widths have been set to 4 and 5 mm, and their lengths, to 80.5 and 86 mm, respectively. According to electromagnetic simulations, this element attains a $|S_{11}|$ better than -13 dB and a radiation efficiency better than 30% over the whole bandwidth. Fig. 3.21 plots the simulated $|S_{11}|$ of the chosen element over a much wider band, in order to highlight the ultra broadband impedance matching of the element. The resulting simulated phase shift introduced by the designed element, the term $\phi_e(f)$ in (3.14), is plotted in Fig. 3.22.

In order to design the phase shifter unit-cell, the minimum cut-off frequency and the unit-cell length were chosen first. The former determines the maximum working frequency and it has to be chosen high enough above the working bandwidth. The proposed antenna is aimed to cover from 1.71 GHz to 2.17 GHz, so f_c^{min} was set to 2.5 GHz. l_{cell} was chosen to be 11 mm in order to make the design easily manufacturable and leave enough space for the placement of the varactors.

Then, the characteristic impedance for the unloaded line (Z_{hi}) and the minimum equivalent characteristic impedance, Z_{min} (which is Z_{loaded} for C_{max}) were chosen. Z_{hi} was set to $110\ \Omega$, which in the chosen substrate led to a microstrip line width of 0.33 mm, and Z_{min} was set to $50\ \Omega$. The latter means that the higher the loading capacitance, the better return losses the phase shifter provides, given an environment of $50\ \Omega$.

With the chosen substrate, Z_{hi} , v_{hi} and, therefore, C_u and L_u , were calculated.

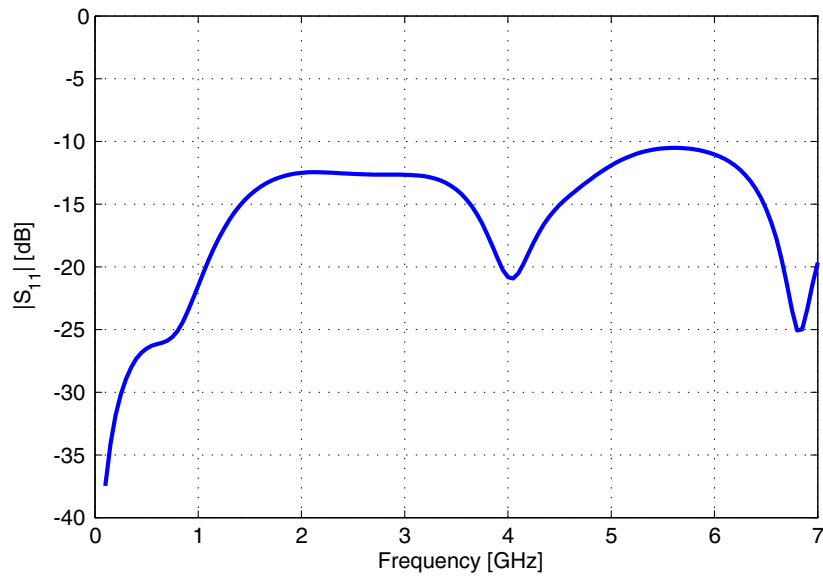


Figure 3.21: $|S_{11}|$ of the radiating element obtained from electromagnetic simulation.

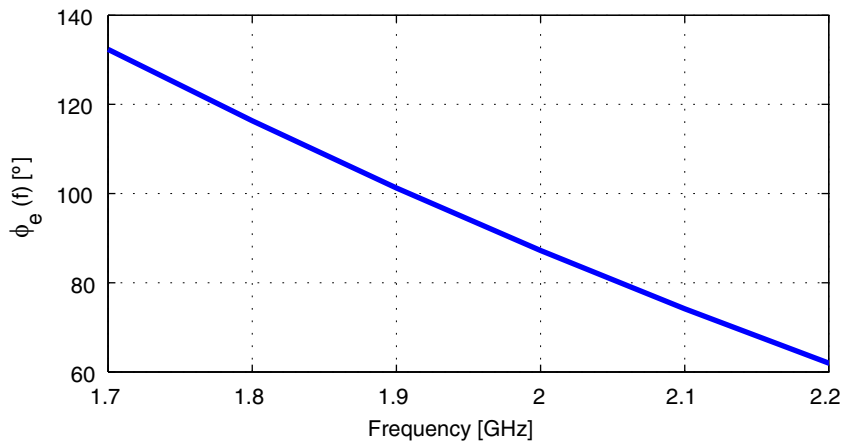


Figure 3.22: Intrinsic phase shift introduced by the element (without considering the phase of the feed microstrip line), obtained from electromagnetic simulation.

Using these and f_c^{min} in (3.11), C_{max} was found to be 2.1 pF. Once the maximum loading capacitance was determined, a varactor was chosen. In this case, it was the MACOM MA46H071-1056, with a top capacitance of 2.46 pF and a minimum of 0.29 pF at its maximum reverse breakdown voltage, which makes Z_{loaded} 88 Ω from (3.9). This is the maximum available characteristic impedance, given the chosen varactor. With C_{max} and C_{min} , it was possible to determine the maximum phase shift range given by a single cell from (3.12), which was 40° at the centre frequency of the bandwidth. If a higher phase shift range is desired, more cells must be added. However, a greater number of cells causes an increase in the insertion losses of the complete phase shifter.

The distance between the radiating elements was set to 67.5 mm after some simu-

lations in order to have a good antenna efficiency and directivity with four elements. To cover a wide enough phase shift range in the working bandwidth, a five-cell phase shifter was selected, with a total length of 55 mm and 200° of maximum phase shift range at the central frequency. The radiating elements and the five-cell phase shifters have been interconnected with $50\ \Omega$ microstrip lines. Then, the total dimension of the antenna, taking into account the input and output access lines for the feeding (30 mm each one) is $266.5\ \text{mm} \times 146\ \text{mm}$. Fig. 3.23 shows the resulting manufactured array. The varactors were fed through the port of the antenna by using a bias-tee to combine the RF with the DC signal.

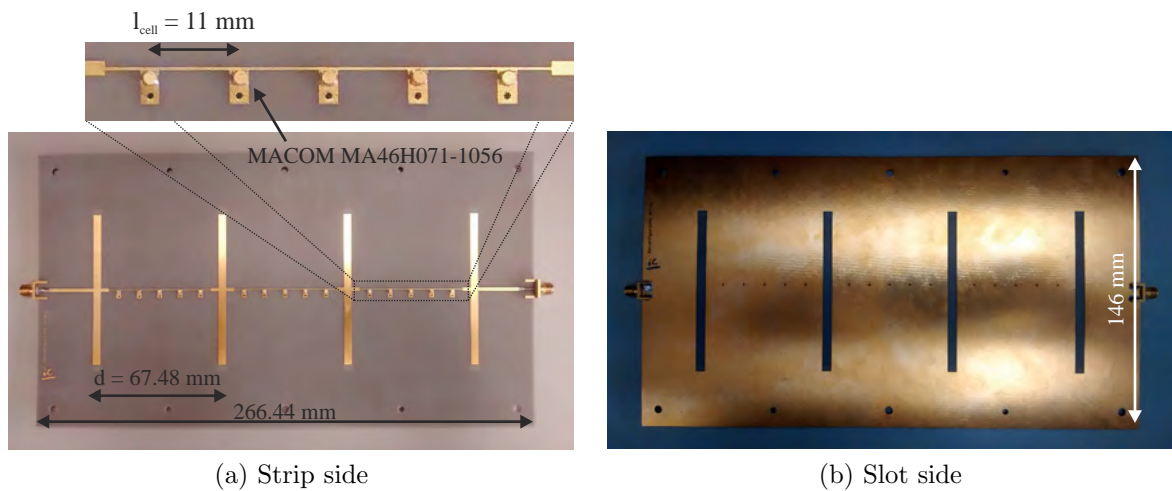


Figure 3.23: Manufactured antenna.

Once the parameters of the design have been determined, the validity of (3.15) to predict the main pointing direction of the array factor is checked. In order to do this, results from (3.15) are compared with the main pointing direction of the radiation pattern obtained from the full electromagnetic simulation of the antenna with HFSS in Fig. 3.24, where θ versus V_R is plotted for different frequencies. Since it is necessary to know the phase shift between elements to evaluate (3.15), the different contributions in the total phase shifts have been obtained from individual electromagnetic simulations. The markers come from HFSS simulations, whereas the solid, dashed and dot-dot-dashed lines are evaluated with (3.15). Good agreement is obtained for $-45^\circ < \theta < 45^\circ$. The discrepancies for angles close to -90° or 90° are due to the radiation pattern of the strip-slot element, which has a null of radiation because of the ground plane. The radiation pattern of the element is not considered in (3.15), which only represents the array factor.

Full electronic scanning is achieved at 1.9 GHz (dashed line), with a continuous

sweep of V_R . For frequencies well below, such as 1.71 GHz (dot-dot-dashed line), some angles are not achievable. In this example, the range from 10° to 45° is not covered. For high frequencies, such as 2.17 GHz (solid line), full electronic scanning is only achievable with a non-continuous sweep of V_R , which supposes a limitation regarding the high losses associated with low values of V_R and high frequencies, as aforementioned.

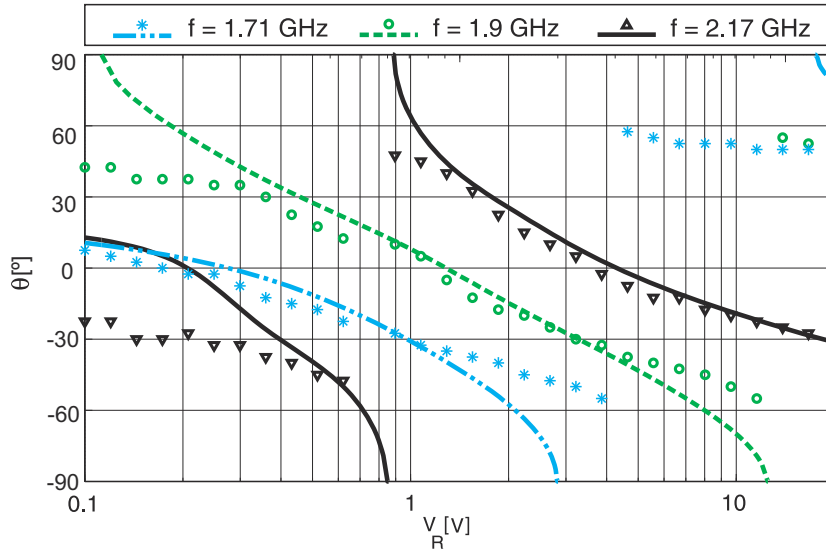


Figure 3.24: Main pointing direction, θ , versus the reverse bias voltage. The lines are obtained by evaluating θ in (3.15) and the markers come from the full electromagnetic simulation of the antenna in HFSS.

3.2.4 Results and Discussion

In this section, the impedance matching and the steering capabilities of the designed antenna are evaluated². It is important to mention that the slight disagreement between the $C(V_R)$ provided by the varactor manufacturer's model and the real component made it necessary to obtain a correspondence between the real V_R and the model for each capacitance value. For this purpose, the varactor was measured and the real $C(V_R)$ curve was obtained. ANSYS Designer was used for the simulation of the circuit parameters, such as the $|S_{11}|$, and the manufacturer's model was used for the varactors, therefore, the equivalent V_R was later used for the measurements. For the radiation simulations, this correspondence was not necessary, since ANSYS HFSS was used with lumped RLC boundaries, which represent a parallel combination of lumped resistor, inductor, and/or capacitor applied to a surface. From the experimental characterisation

²The radiation measurements were taken in the anechoic chamber of the Laboratorio de Ensayos y Homologación de Antenas, Universidad Politécnica de Madrid, Madrid (Spain).

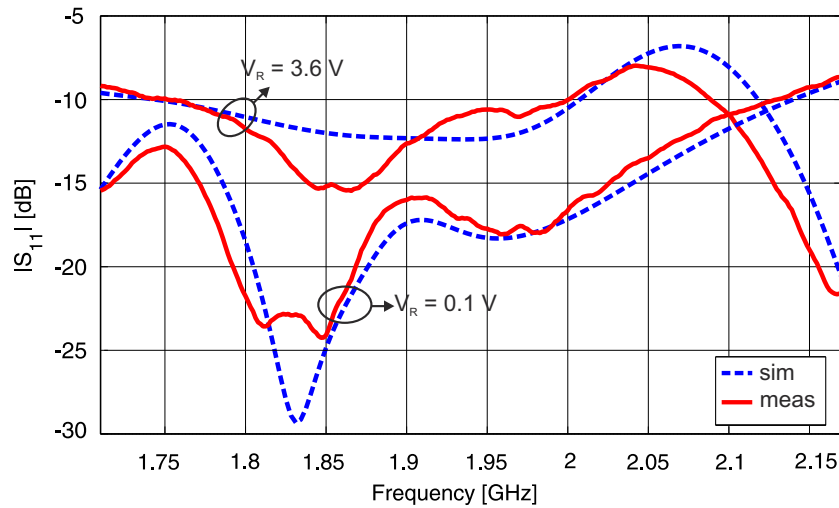


Figure 3.25: $|S_{11}|$ obtained from the simulation and measurement of the designed array for $V_R = 0.1$ V and $V_R = 3.6$ V.

of the varactor, the equivalent RC circuit was obtained and, then, the value of the capacitance and its corresponding resistance were directly introduced into HFSS to take into account the real losses of the varactors.

In order to analyse the impedance matching of the antenna, the S_{11} parameter was measured and compared to the simulations. This is shown in Fig. 3.25 for two values of V_R . In the traces for $V_R = 3.6$ V, the $|S_{11}|$ is above -10 dB between 2 and 2.12 GHz. This voltage corresponds to a broadside lobe in that frequency range, according to Fig. 3.24. Under this condition, the radiating elements are in phase, so the impedance mismatching is maximum. In the traces for $V_R = 0.1$ V, the same behaviour is found for frequencies above 2.12 GHz.

However, good matching is found over almost the whole considered bandwidth, the $|S_{11}|$ being below -10 dB. As was expected from the phase shifter design, a lower value in V_R provides wider matching bandwidth, since the loading capacitance is near its maximum and the equivalent characteristic impedance is closer to 50Ω .

Regarding radiation, two possible modes of operation are of interest: maintaining the main lobe over frequency and electronic scanning at a certain frequency. For the first purpose, the reverse bias voltage had to be adjusted to get the chosen angle for the desired frequencies by evaluating $\theta(V_R)$ in equation (3.15). According to Fig. 3.24, a certain range of θ can be pointed for all the frequencies considered. This range is theoretically limited by the lowest frequency and it goes from approximately -10° to 50° .

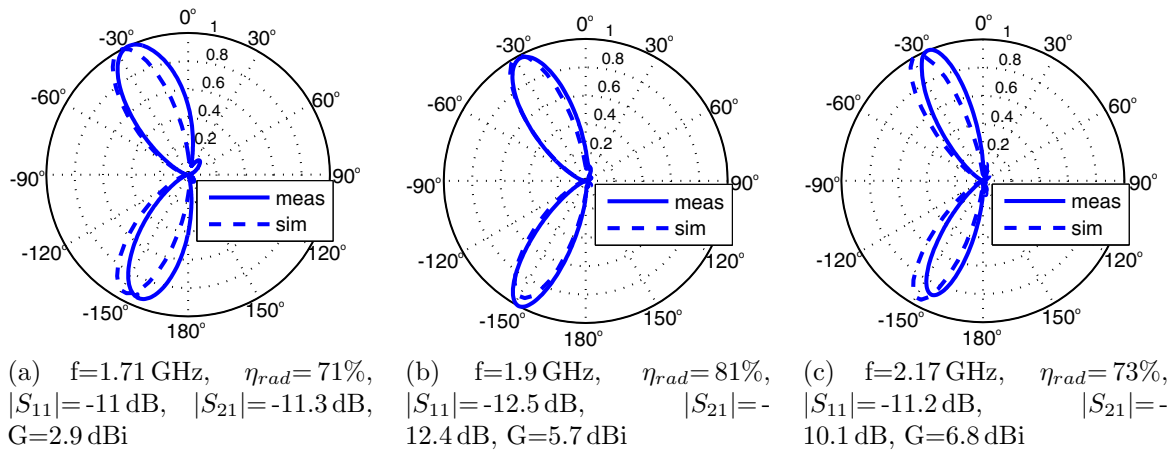


Figure 3.26: Normalized simulated (dashed lines) and measured (solid lines) radiation patterns in linear scale obtained when some V_R are applied as the reverse bias voltage for different frequencies: 1.71 GHz, 1.9 GHz and 2.17 GHz, in order to maintain the main beam direction to -30° . The values of the measured $|S_{11}|$, $|S_{21}|$ and gain and the simulated radiation efficiency are shown for each plot.

As an example, an angle of $\theta = -30^\circ$ was chosen in order to illustrate the capability of the antenna of maintaining the pointing angle over frequency. Simulations were used to find the voltages needed for $\theta = -30^\circ$ (Fig. 3.24). Measurements of the radiation patterns for the ZX plane and different frequencies are shown in Fig. 3.26, where the main lobe is pointing to the required angle with a measured $|S_{11}|$ below -11 dB and a gain better than 2.9 dBi at the lowest frequency. This figure highlights how this antenna can work over a 24% of fractional bandwidth. This is possible due to the good impedance matching over a wide range of frequencies of the radiating element, which allows tuning the frequency without modifying the element geometry, and the high phase range provided by the phase shifter. As expected, the gain increases with frequency, as does the electrical size of the antenna. The simulated radiation efficiencies are also indicated in the figure. It must be pointed out again that this simulation takes into account the real losses of the varactor, as previously explained, through the use of RLC boundaries. Thanks to the low losses of the chosen varactor over the designed frequency band, good values are obtained for the studied cases: 71%, 81% and 73% for 1.71, 1.9 and 2.17 GHz, respectively. The lowest value is obtained for 1.71 GHz, at which the required reverse voltage to obtain $\theta = -30^\circ$ is the lowest one and, consequently, the varactor presents more losses. The values of the $|S_{21}|$ are also included in Fig. 3.26. More power is wasted in Port 2 (the load) at 2.17 GHz, which can explain why the radiation efficiency is lower than for 1.9 GHz.

When a single frequency within the working bandwidth is considered, the proposed

antenna is likewise capable of steering its main lobe through two different quadrants. As an example, the measured radiation patterns at 2 GHz for the proposed antenna are plotted in Fig. 3.27 for values of V_R so that the main lobe steers from $\theta = -45^\circ$ to 45° in order to illustrate this scanning capability. The necessary values of V_R have been obtained from the analysis based on electromagnetic simulations, like Fig. 3.24. Electronic scanning is successfully achieved over a range of around 90° .

Table 3.1 shows the measured $|S_{11}|$, $|S_{21}|$ and gain, and the simulated radiation efficiency associated to the radiation patterns plotted in Fig. 3.27. Good impedance matching is achieved except for the broadside case, as it is expected from travelling-wave antennas, and a gain between 3.3 and 6.6 dBi is obtained. These values of gain might be low for beam scanning application, such as radar, although beam steering might be useful for other purposes such as reconfiguration of the area illuminated by the antenna, for which the gain may not need to be high. In any event, the gain can be increased, if required by the application, by making the antenna longer (adding more radiating elements with their corresponding phase shifters). The values of the $|S_{21}|$ indicate that some power is wasted at the end of the antenna (Port 2) and, then, the antenna could be made longer, thus improving both the gain and the radiation efficiency. Moreover, the element could be designed to radiate less power, thus requiring more elements (and, consequently, a longer antenna) for the same total efficiency.

Given Table 3.1, a reasonable radiation efficiency is obtained for all the directions, with the lowest value of 50% for $V_R=20$ V due to the high $|S_{21}|$. The voltage-dependent losses introduced by the varactors, as well as their voltage-dependent matching, are the cause of the variability of this parameter. Anyway, obtaining a radiation efficiency of around 70% in average, indicates that the radiating elements are able to radiate a significant amount of the power that reaches them, given the losses introduced by the varactors.

The measurement results demonstrate the antenna capability for both electronic steering the beam at a single frequency in a certain bandwidth and maintaining the radiation pattern over frequency. Moreover, the usefulness of the design curves based on the theoretical equation (3.15) and the electromagnetic simulations has also been highlighted. However, some limitations can be found, such as the reduced scanning range at the lowest frequency (1.71 GHz) or the high losses associated to the high frequency and low values of V_R , which might limit the steering at 2.17 GHz to angles above -30° , according to Fig. 3.27. In this way, according to Fig. 3.27, maintaining the beam over the considered bandwidth can be achieved in the range between -50°

Table 3.1: Measured $|S_{11}|$ and gain and simulated radiation efficiency for the voltages used in Fig. 3.27 at 2 GHz

V_R [V]	$ S_{11} $ [dB]	$ S_{21} $ [dB]	Gain [dBi]	η_{rad}
1.3	-17.1	-19.3	3.5	73%
1.5	-22.8	-19.2	3.3	75%
1.9	-22.8	-21.5	4.3	76%
3.0	-7.6	-10.5	3.6	58%
4.0	-10.0	-10.5	4.6	74%
7.0	-11.4	-12.4	6.6	80%
20.0	-10.1	-8.6	5.1	50%

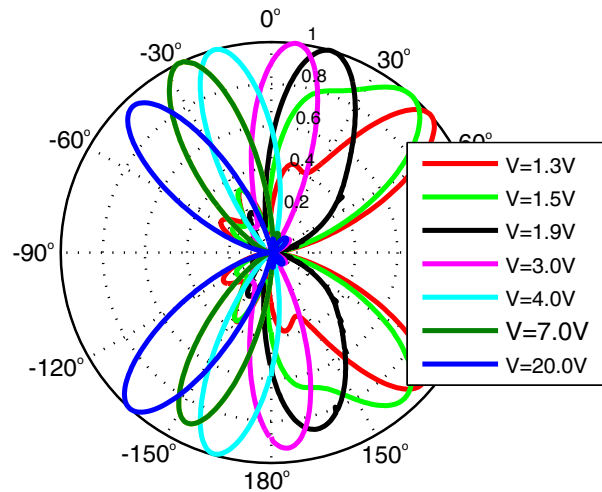


Figure 3.27: Measured normalized radiation patterns in linear scale at 2 GHz for some values of V_R .

and 10° off the broadside direction (where broadside corresponds to 0°). Nevertheless, the results of the performance of the proposed design are a consequence of the decisions that have been made in the design. It is important to point out that the curves in Fig. 3.27 depend on many variables (the distance between elements, the number of cells of the phase shifter, etc). Therefore, the results can be improved by, for example, incorporating more stages in the phase shifter or by using another varactor device. Anyway, the specific application will set the constraints and the proposed design is just an example to show the potential of this simple structure.

Finally, another aspect that might limit the practical applicability of the antenna is the bidirectionality. If, for the specific application, it is desirable to avoid one of the beams, the classic solution of placing a reflector at a certain distance from the antenna can be applied. This solution has been simulated, in order to illustrate this

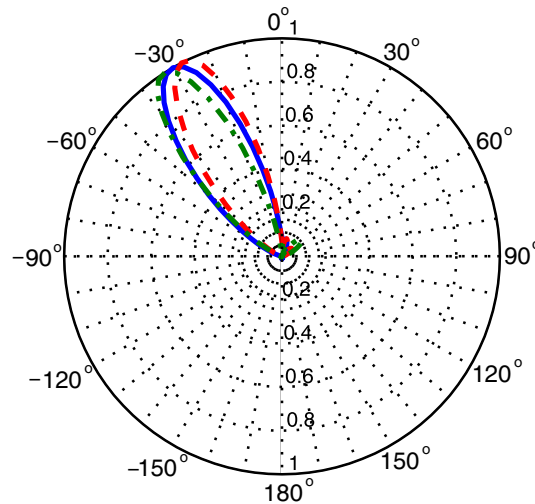


Figure 3.28: Normalized simulated radiation patterns in linear scale obtained for the same case as Fig. 3.26 with a reflector plane over the microstrip layer.

possibility. The reflector has been placed at a distance of $\lambda/4$ at the centred frequency of the bandwidth (i.e. 3.9 cm), over the microstrip layer. Fig. 3.28 shows the resulting radiation patterns corresponding to the functionality of Fig. 3.26. It is shown that one beam can be removed without modifying the radiation pattern, except for an increase in the gain. In any event, some other solutions for removing one beam could be implemented, like the use of FSSs (Frequency Selective Surfaces) or AMCs (Artificial Magnetic Conductors), which would allow the size of the antenna to be minimised for single beam radiation.

3.3 CONCLUSIONS

The broad impedance bandwidth and series feeding configuration of the complementary strip-slot makes it especially suitable for building TWAs with beam steering capabilities. In this chapter, the application of the element to build such arrays has been investigated and proven. The wideband matching of the element allows significant flexibility in the design and enhanced performance.

In the first section of the chapter, a TWA built by cascading several elements has been studied. It has been proven that the Floquet's theorem and the spatial harmonic expansion are appropriate tools for predicting the frequency behaviour in spite of the limited size of the array. The structure is able to scan from backward to forward directions according to this theory, over different bands. The multiband behaviour is a consequence of the periodicity of the phase constant, but it is possible thanks to the

broadband matching of the element. The low deterioration of the radiation efficiency and reflection coefficient in broadside has been improved by slightly misaligning the slots with respect to the strips, thus achieving full-space frequency scanning over both bands.

In the second section of the chapter, the concept of TWA has been extended to add reconfigurability properties by introducing varactor-based loaded-line phase shifters. A design has been carried out. Unlike previous works in the literature, the proposal achieves both electronic steering with wide angle range and fixed beam over the design bandwidth, possible thanks to the non-resonant element on which the array is based. Since the radiating element is broadly matched, it does not have to be modified when the frequency is varied, which is a significant advantage with respect to other works. The proposed array, in microstrip technology, presents a very simple design with series feeding that allows all the integrated devices to be placed on the same layer and to be controlled by a single DC signal. In this way, the versatility of steering or maintaining the beam over frequency can be carried out by just varying the reverse bias voltage of the loading capacitance. Therefore, once the structure has been set up, it does not require any on-site supervision, allowing a remote control of the antenna.

Chapter 4: Strip-Slot-Based Log-Periodic Array

In Chapter 2, the complementary strip-slot element has been analysed and the results have shown its potential as the basic element for novel antennas. This has been highlighted in Chapter 3, in which the strip-slot has been used to build linear TWAs. In this chapter, the concept of a planar log-periodic array based on this wideband radiating element is studied. Since the radiating element is not resonant, the analysis differs from the previous reported log-periodic arrays. The chapter is structured as follows. Section 4.1 states the motivation and reviews the state of the art of log-periodic arrays. Section 4.2 briefly explains the design parameters in classic log-periodic arrays. Section 4.3 describes the design criteria that must be taken into account for building a log-periodic array with this element, whereas Section 4.4 collects the simulation and experimental results for a particular design. Section 4.5 describes a method for computing the radiation of the array using the equivalent circuit of the element, Section 4.6 explores the possibility of avoiding bidirectional radiation by introducing a reflector plane and, finally, Section 4.7 summarizes the main conclusions.

4.1 MOTIVATION

Massive wireless data transmission is nowadays one of the most demanding services from telecommunication users. In order to satisfy this need, compact antennas that cover wide bandwidths maintaining the radiation pattern are required. Therefore, the field of wideband antennas has received increasing research interest. These antennas are also important for reconfigurability, since their frequency response can be modified by introducing reconfigurable filters into it, thus switching into a desired narrow band [42, 43]. One of the wideband antenna examples used is the monopole antenna, which covers

wide bandwidth with a simple geometry; however, its radiation pattern changes rapidly with frequency. Vivaldi antennas are capable of maintaining the radiation pattern over frequency, but they have the problem of large size. Log-periodic arrays are wideband antennas built out of resonant elements. Thanks to the log-periodic progression in its geometry, a log-periodic array is suitable for covering wide bandwidth. Combining printed technology with log-periodic arrays results in one of the best candidates for this purpose, due to its simplicity, light weight, low profile and performance.

Printed dipole arrays have the drawback of complex feeding, which is an unsolved problem still currently being addressed [44]. However, other planar log-periodic arrays can be properly fed by a microstrip line, thus simplifying the feeding structure. There are some examples of microstrip-fed patch log-periodic arrays, with different feeding configurations: microstrip series configuration [45], slot-coupled feeding [46], direct feeding with vias [47], etc. In either the slot or patch radiators, the design methodology for the log-periodic array is similar to that carried out by Carrel for dipole log-periodic arrays [48], since both are resonant elements as the dipole. Therefore, the design methodology has been established taking into account this resonant nature. For instance, the scale factor τ ($\tau = \frac{l_n}{l_{n+1}}$, where l_n is the length of the n^{th} element) is limited by the resonant behaviour of the element, since enough elements are necessary to radiate all the power and, if τ is very small, the adjacent element resonances are too far from each other and not enough elements are able to radiate at a certain frequency. However, if τ could be lowered, a reduction in size would be achieved for the same bandwidth [49].

On the other hand, a matched load was usually used to terminate a microstrip log-periodic array, which has the advantage of avoiding the undesired reflection at the load, but it deteriorates the radiation efficiency over the operating bandwidth, especially at the band edges, of about 10% or even more [50].

The complementary strip-slot element does not have a resonant nature and is broadly matched, as shown in Chapter 2. Therefore, building a log-periodic array with this element can allow extending the bandwidth with respect to conventional log-periodic arrays. Additionally, the wideband nature of the element guarantees high radiation efficiency, thus allowing the termination of the array in open circuit instead of a matched load. To the author's knowledge, the concept of a log-periodic array based on a wideband element has not been hitherto discussed.

4.2 BRIEF REVIEW ON CLASSIC LOG-PERIODIC ARRAYS

Log-periodic arrays consist of a transmission line loaded with log-periodically scaled radiating elements at log-periodic spaces [51]. A log-periodic array transforms into itself when the frequency is scaled logarithmically, since inside the array there is only one region that is radiating (the active region) and this region is being shifted inside the array with a change in frequency in a way that it keeps the same geometry in terms of wavelengths.

Fig. 4.1 shows a schematic diagram of a log-periodic array with linear elements. The following parameters define its geometry:

$$\tau = \frac{l_{n-1}}{l_n} = \frac{d_{n-1}}{d_n} \quad (4.1a)$$

$$\sigma = \frac{d_n}{2l_n} \quad (4.1b)$$

$$\alpha = \tan^{-1} \left(\frac{1 - \tau}{4\sigma} \right) \quad (4.1c)$$

where τ is named scale factor, σ , spacing factor, and α is the angle defined in 4.1.

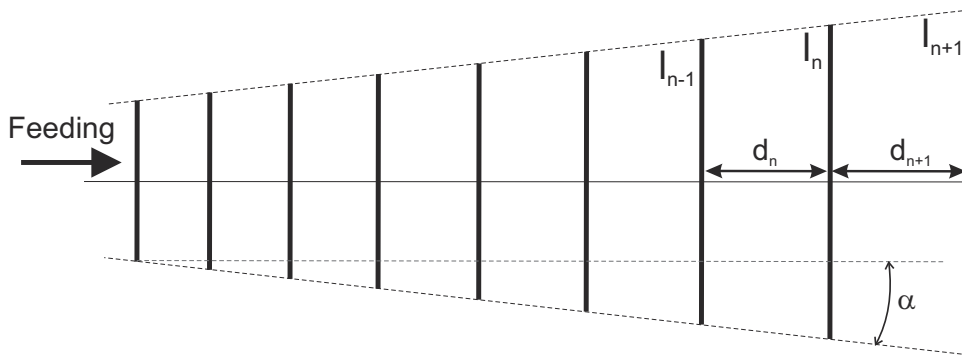


Figure 4.1: Schematic diagram of a log-periodic array.

Since the elements in a classic log-periodic array are resonant, the array bandwidth will be determined by the lengths of the shortest and the longest elements. At the lowest frequency, the largest element will be around its resonance and as the frequency is increased, the element around its resonance (active element) will be closer to the apex. Since the excitation is by the shortest element, the wave must go through some elements until it reaches the active element. This region of non-radiating elements is called the transmission region. Due to their resonance nature, these elements are mismatched out of their resonance frequencies. Then, it is indispensable to cause

destructive interference in the transmission region to avoid reflections. Since the phase shift between adjacent elements in the transmission region is low because its distance is much lower than the wavelength, it is sufficient to introduce a frequency-constant 180° phase shift between adjacent elements. In dipole log-periodic arrays, this was achieved by mechanically crisscrossing the feed [52], and in planar technology this was simplified by alternating the offset of the patch/slot with respect to the feed line for each adjacent element [50]. Moreover, this extra phase introduction produces a phase progression so that the array radiates endfire towards the excitation (shorter elements), thus preventing the larger elements to cause interference effects to the pattern result for being excited by the radiated field, which happened when the extra 180° phase was not added.

An important decision to make in log-periodic arrays is the value of τ , which determines the number of elements in the active region. If it is too close to 1, the variation in length between one element and its adjacent is low and an array with a high number of elements will be required to cover a certain bandwidth. However, high radiation efficiency is guaranteed since the active region will be constituted by enough elements to radiate all the power off. On the other hand, if τ is low, a more compact design is obtained, but a smaller number of elements will make up the active region, which might not be able to radiate all the power, and end effects of the array can deteriorate the performance.

The selection of σ determines the phase velocity of the travelling wave, which increases when σ does it. From semiempirical results of dipole arrays, it was concluded that, for a certain τ , there is an optimum value of σ to guarantee that the phase progression is the necessary for backfire radiation with the highest directivity [51].

4.3 DESIGN OF THE PROPOSED LOG-PERIODIC ARRAY

The complementary strip-slot is a non-resonant element. Therefore, if properly designed it can be matched over a very broad bandwidth. Moreover, its radiation efficiency is neither resonant, but high-pass, as was shown in Fig. 2.23, since the element starts radiating efficiently from the resonance frequency of its slot on (which will be referred to throughout this chapter as the *characteristic frequency* of the element). Consequently, as in dipole log-periodic arrays, the lengths of the shortest and the longest

elements will determine the operating bandwidth. If the active region was only made up of one element, then the length of the smallest slot (l_{s1}) must be half-wavelength at the maximum operating frequency and, likewise, the length of the longest element (l_{sn}) must be half-wavelength at the minimum frequency. Since only one complementary strip-slot element cannot radiate all the power, the active region will be wider than a single element and the bandwidth will be less than that given by $\frac{l_{sn}}{l_{s1}}:1$.

Another parameter that needs to be addressed is the relative spacing (σ) between elements. In the case of the strip-slot element, it cannot be chosen too high, because then many ripples appear in the radiation patterns and not too low because then the matching gets worse due to inter-element coupling effects. As previously mentioned, in log-periodic arrays with resonant elements, it is indispensable to introduce a 180° phase shift between adjacent elements to avoid reflections from the transmission region. Nevertheless, when broadly matched elements are used, this problem disappears since all the elements in the array are matched over the whole bandwidth, even below their characteristic frequency. Therefore, in the proposed array, this additional phase shift must not be introduced. In this way, the spacing factor σ can be chosen according to other criteria. In particular, coupling effects between elements impose a minimum value for this variable, because low values of σ lead to poor matching.

An additional difference with conventional log-periodic arrays lies in the selection of the scale factor τ . In the classic arrays, τ must be near 1, because if it is too low, there are not enough elements able to radiate and the radiation efficiency can be low. Moreover, reflections from end effects deteriorate the performance. This limitation is overcome with the strip-slot element. Since its radiation efficiency is not resonant but high-pass, it is assured that there are enough elements radiating at each frequency. Low values of τ reduce the size of the array to cover a certain bandwidth.

In order to build the array, the log-periodicity has been applied in the lengths of the slots, as well as in their widths. However, the lengths and widths of the stubs are designed for optimum matching of each element, which does not necessarily follow a logarithmic progression. This happens because not all the geometrical variables of the design are scaled. For instance, to avoid complexity in the design, the height of the substrate and the width of the microstrip are kept constant. Therefore, while designing the lengths and widths of the stubs for optimum matching, the log-periodicity of the image impedance is ensured. This way, the electrical properties of the array, and not the geometry of the element, are attempted to be maintained with the logarithm of frequency.

Table 4.1: Geometry of the strip-slot elements of the proposed array.

Element	l_S [mm]	w_S [mm]	l_M [mm]	w_M [mm]
1	13.58	0.40	13.25	0.54
2	14.93	0.44	14.37	0.57
3	16.42	0.48	15.59	0.60
4	18.06	0.53	16.93	0.65
5	19.86	0.58	18.39	0.70
6	21.84	0.64	20.01	0.75
7	24.01	0.71	21.81	0.81
8	26.41	0.78	23.80	0.87
9	29.04	0.85	26.00	0.94
10	31.93	0.94	28.43	1.01
11	35.12	1.03	31.13	1.09
12	38.62	1.14	34.15	1.18
13	42.47	1.25	37.48	1.28
14	46.71	1.38	41.19	1.41
15	51.36	1.51	45.35	1.52

A log-periodic array example has been designed for the GIL 1032 substrate, with $\epsilon_r=3.2$ and $h = 30$ mil. A low τ has been chosen to prove the aforementioned concept ($\tau = 0.909$). In order to cover an acceptable bandwidth, but keeping the total size of the array manageable, 15 elements will build up the array. As a trade-off between matching and size, σ has been set to 0.17, since a further reduction of the spacing would have led to mismatching due to coupling effects. The length of the longest slot (l_{sn}) has been chosen to resonate at 2.3 GHz and the length of the smallest (l_{s1}), at 8.6 GHz. Once the parameters of the array are set, the slot geometries are determined. Nevertheless, the stubs must be designed for optimum matching, as previously mentioned. For the GIL 1032 substrate, the slotline-microstrip coupling structure has been electromagnetically analysed in Section 2.5 and the even and odd mode parameters have been extracted for a wide range of stub and slot widths and over the bandwidth of interest. This way, it is possible to obtain the pairs of widths that lead to 50Ω broadband impedance level (Fig. 2.25).

Taking into account Fig. 2.25, the geometry of the array is shown in Table 4.1, where l_S and w_S are the length and width of the slot, respectively, and l_M and w_M , those of the stub. The resulting layout can be seen in Fig. 4.2. The array is fed through the smallest element by a 50Ω microstrip line, 1.84 mm wide. The total length of the array is 18.4 mm, which is 2.3λ at the lowest characteristic frequency (2.3 GHz).

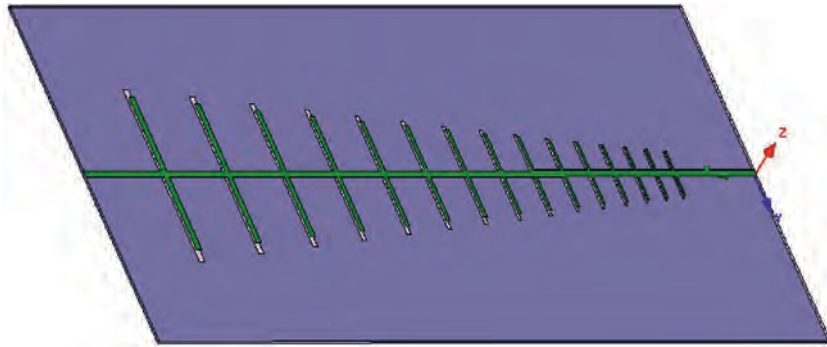


Figure 4.2: Layout of the proposed log-periodic array.

4.4 RESULTS AND ANALYSIS

The proposed array has been manufactured and measured. The resulting structure can be observed in Fig. 4.3. Two connectors have been soldered at the ends of the microstrip line in order to be able to compare the termination in open circuit with the matched load.

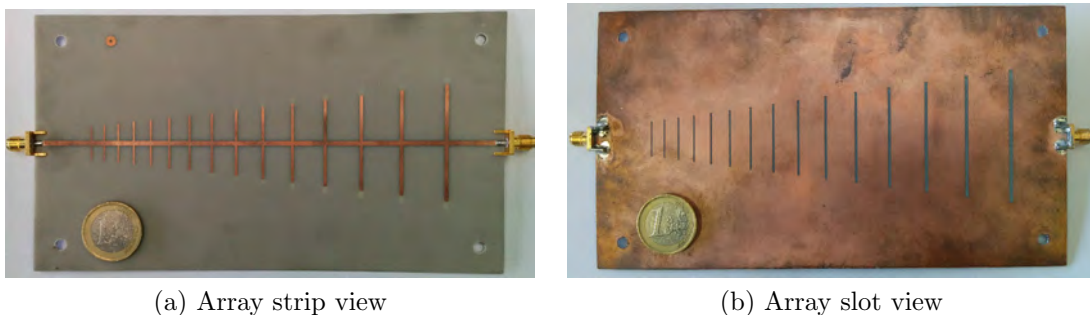


Figure 4.3: Photographs of the manufactured log-periodic array.

In Fig. 4.4, the VSWR of the proposed design is plotted. The figure shows the measurement and simulation with matched load, along with the measurement with open circuit. It can be observed that from 2.7 GHz, the array is well matched (with a criterion of $VSWR < 2.5$) and there is no difference between a matched load or an open circuit, which means that the array is radiating all the power off (there is no reflection from the load). The comparison between measurements with and without matched load allows us to determine the beginning of the operating bandwidth (2.7 GHz), which is slightly above the characteristic frequency of the largest element (2.3 GHz). This fact is a consequence of the length of the active region, which is bigger than a single element. Therefore, it is required that the minimum operation frequency is such that several elements are radiating. It is also highlighted in Fig. 4.4 that good agreement is obtained between simulation and measurement.

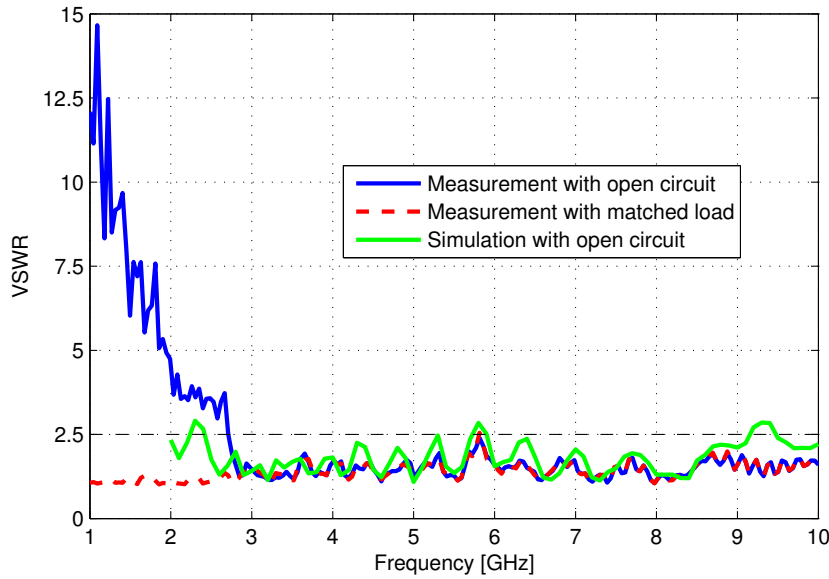


Figure 4.4: $VSWR$ comparison between simulation and measurement.

In order to analyse the behaviour of the array, a study of the evolution of the voltages across the slots with frequency has been carried out. Fig. 4.5 shows the voltage magnitude across the slots at different frequencies, extracted from electromagnetic simulation (using the *Field Calculator* of HFSS). It can be observed that the point of maximum voltage shifts with an increased of frequency towards shorter elements, which corroborates the operation as a log-periodic array. Moreover, it can be appreciated that out from the extreme frequencies there are around six slots with significant voltage at each frequency, which provides an idea of the effective length of the active region.

In Fig. 4.6, the measured¹ and simulated radiation patterns at different frequencies over the operating bandwidth are shown. It can be observed that the radiation pattern is mostly maintained over frequency, as expected. However, some variability in the pointing direction is appreciable at some frequencies. In the measurements, a maximum shift of approximately 12° at 6.55 and 8.65 GHz is found. For the rest of the frequencies, only $\pm 3^\circ$ shift is obtained. The maximum shift of 12° is found for a half-power beamwidth of around 27° , which means that more than 50% of the beam overlaps with the desired beam. Although undesired, this variability is not uncommon in log-periodic arrays, since, by design, the characteristics of the antenna are only guaranteed at the corresponding log-periodic frequencies. Moreover, truncation effects can modify the radiation pattern at the extreme frequencies (which is the case of 8.65 GHz).

¹The radiation measurements were taken in the anechoic chamber of the Communications Engineering Group of the University of Birmingham, Birmingham (UK).

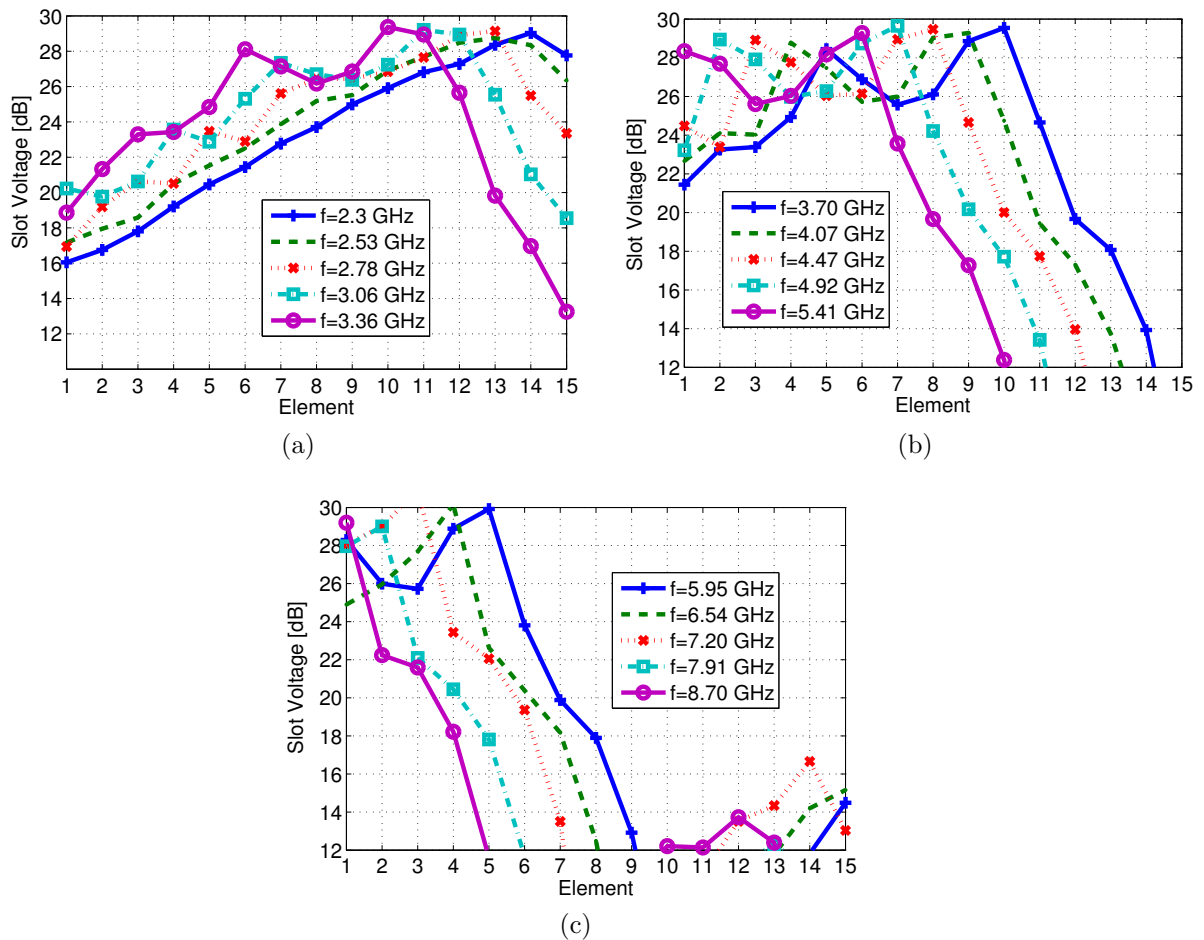


Figure 4.5: Magnitude of the voltage drop across the slots at different frequencies, extracted from electromagnetic simulation (using the *Field Calculator* of HFSS).

If this variability in the pointing angle is critical for the specific application, it could be lowered by choosing τ closer to the unity and introducing more elements, but there will always be a trade-off between size and performance.

Bidirectional radiation is obtained, since the complementary strip-slot radiating element radiates into both half-spaces. For the analysis of radiation of a log-periodic structure, it is customary to consider the structure as a locally periodic structure, which means that the active region is considered as a uniform array instead of log-periodic [53]. In this way, according to Floquet wave expansion and spatial harmonics theory, the array must radiate towards the apex, since when a spatial harmonic enters the visible range, radiation occurs in backfire direction (see Section 3.1.2). That is why classic log-periodic arrays always radiate backfire and no other radiation direction is possible. Since the radiation pattern of a single element of the array proposed in this paper has a null in the direction of the apex, the resulting main beam direction

is a backward angle but not backfire, which can be seen in Fig. 4.6. Therefore, the combination of the array factor and the element radiation pattern leads to radiation at a fix angle around 45° .

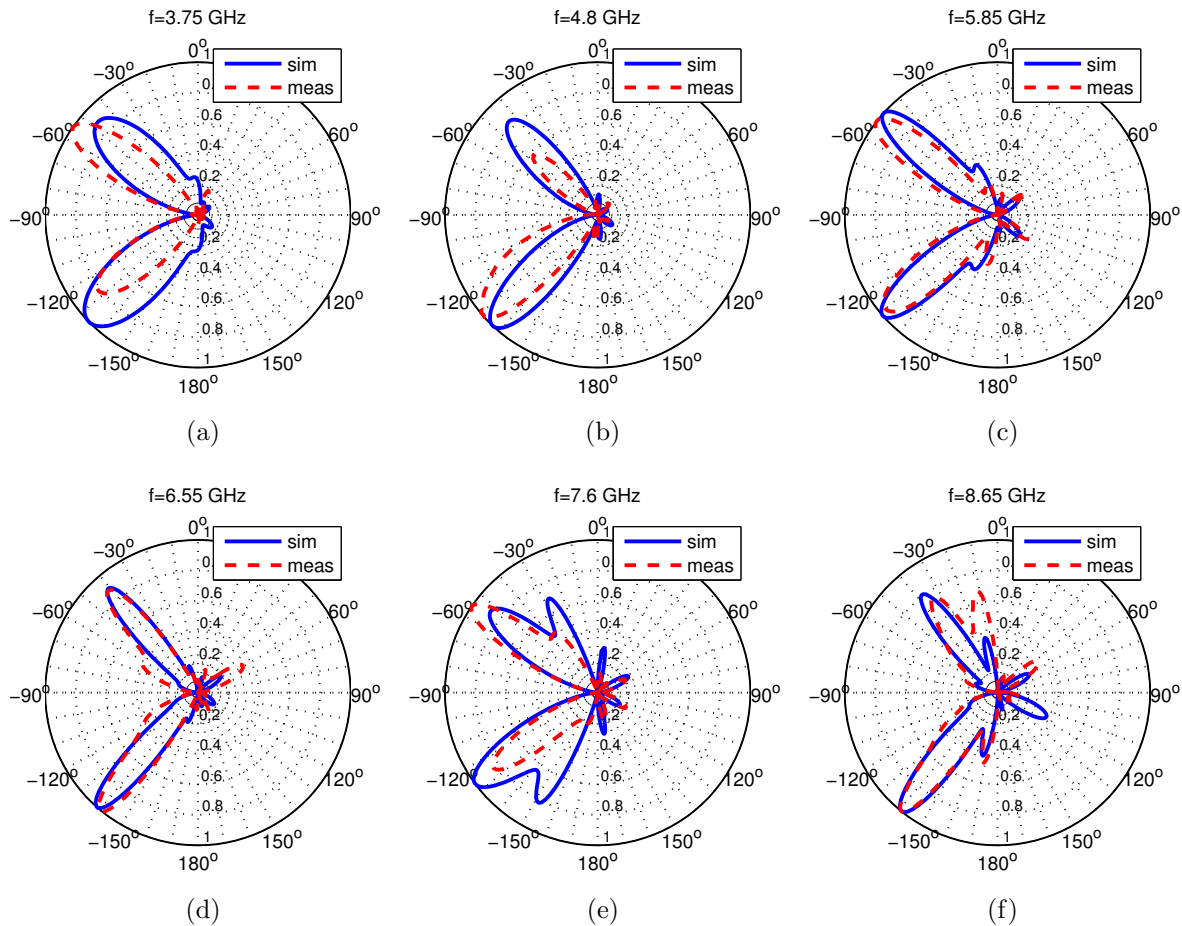


Figure 4.6: Measured and simulated radiation patterns of the log-periodic array at different frequencies.

The simulated and measured peak gain are plotted in Fig. 4.7. The gain decays at low frequencies, since below 2.3 GHz, all the elements are below their characteristic frequency and hardly radiate. Over the operating bandwidth, a peak gain between 5 and 9 dB is obtained.

The simulated radiation efficiency is plotted in Fig. 4.8. It can be observed that an efficiency of better than 85% is obtained over the operating bandwidth.

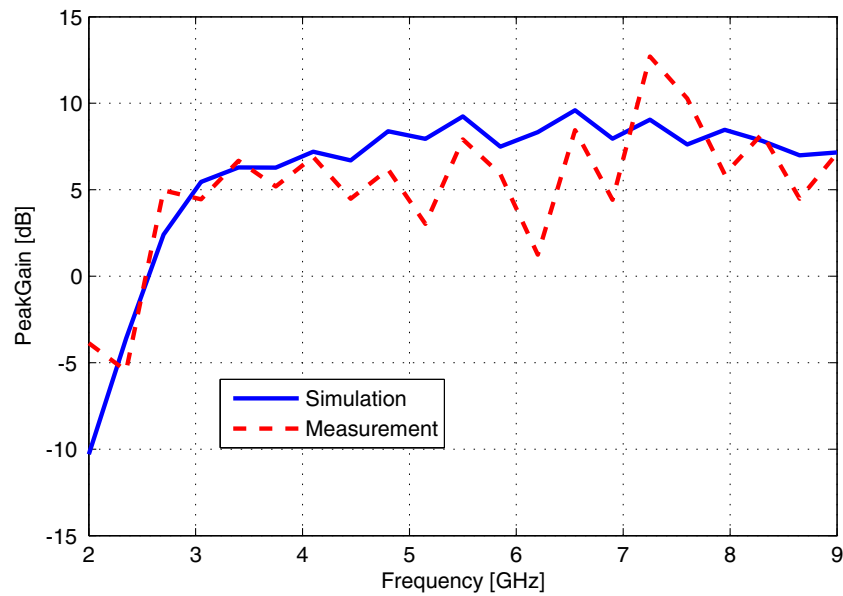


Figure 4.7: Peak gain comparison between simulation and measurement.

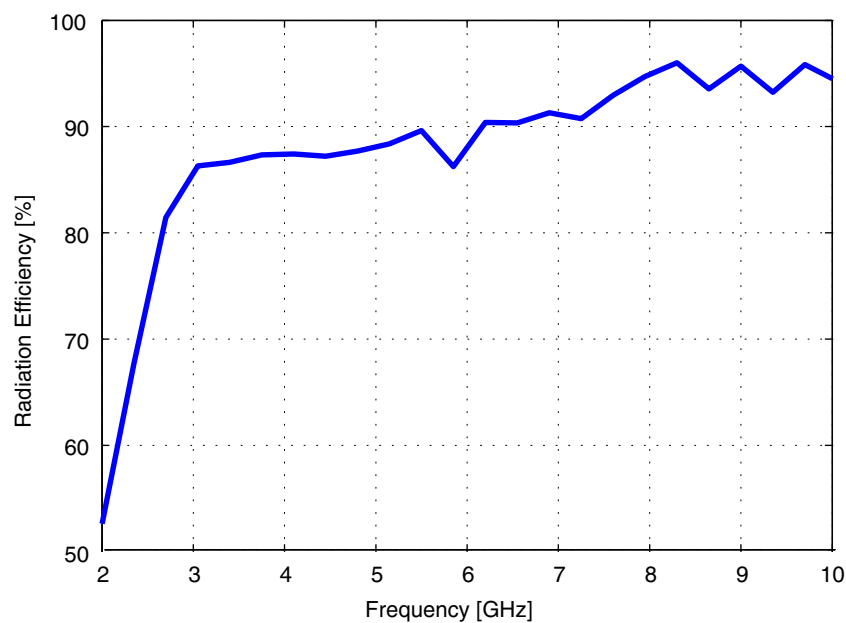


Figure 4.8: Simulated radiation efficiency of the log-periodic array.

4.5 RADIATION COMPUTATION USING THE EQUIVALENT CIRCUIT

A drawback in the study and design of these log-periodic arrays is the high computational load of the electromagnetic simulation, which makes it difficult to optimise, or even to explore, different designs. Therefore, in this section, an alternative method of analysis by using equivalent circuits is described.

In Section 2.2.2, a lattice network equivalent circuit was proposed for the complementary strip-slot element. Therefore, by simulating the coupling microstrip-slotline structure for different widths of the slot and the strip over frequency, the even and odd mode parameters for a wide range of geometries and frequencies can be obtained. A modification with respect to the circuit of 2.2.2 has been introduced in an effort to model the radiation. Since no accurate model for the radiation has been found and the slot radiation is dominant over the strip, the radiation has been incorporated into the series branch (the branch associated with the slot) as a frequency-dependent resistance $R_{rad,i}$. This parameter is obtained from the full electromagnetic simulation of a single element, by extracting the impedance parameters, converting them into lattice impedances and taking the real part of the series branch. An attempt was made in order to introduce the radiation as losses-per-unit length in the transmission lines of the series branches, instead of a frequency-dependent resistance, but no difference was noticed in the results.

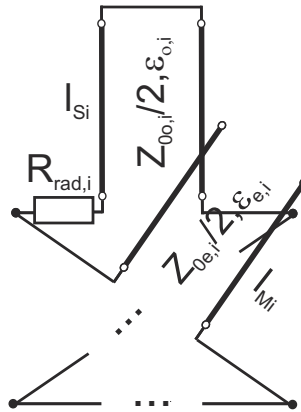


Figure 4.9: Lattice equivalent circuit of the element i .

Once the radiation resistance for one referential element n has been extracted, the equivalent circuit of another element i can be built by taking its corresponding set of mode values $[Z_{0e,i}, \epsilon_{e,i}, Z_{0o,i}, \epsilon_{o,i}]$ and by properly frequency scaling the radiation resistance of the referential element n :

$$R_{rad,i}(f) = R_{rad,n}(\tau^{n-i}f). \quad (4.2)$$

This radiation scaling is possible because one slot is equal to its adjacent except for a scale factor, therefore it can be assumed that the radiation is as well scaled. A similar scaling procedure was published in [54] for computing the S_{11} of a large log-periodic array by simulating just a small part of it and scaling the S-Parameters for obtaining

the total one. However, here only the scaling of the radiation is proposed, since an equivalent circuit for each array element when losses are neglected is available.

In order to check the aforementioned method, the design proposed in Section 4.4 has been modelled. The largest element $n = 15$ has been electromagnetically simulated over a wide bandwidth and $R_{rad,n}$ has been extracted. Then, for the rest of the elements, the radiation resistance has been scaled as indicated by (4.2).

By cascading the equivalent circuits of all the elements and the microstrip interconnection sections, the model of the total structure is obtained. As an example, Fig. 4.10 shows the comparison between the voltage drop across the slots 1, 7 and 15 extracted from HFSS and from the equivalent circuit model, in phase and magnitude. It can be observed that good agreement is obtained, even when the proposed method does not take into account coupling between elements.

From the voltage drops across the slots, it is possible to obtain the radiation power pattern as [51]

$$U = |E_{\theta n}|^2 \quad (4.3)$$

where the subindex n indicates *normalized* with respect to its maximum and

$$|E_{\theta}| = \left| \sum_{i=1}^{15} V_{slot,i} e^{jkr_i \sin \theta} |\cos(\theta)| \right|, \quad (4.4)$$

with k the phase constant in vacuum, r_i stands for the distance between the first element of the array and the element i and, finally, $|\cos(\theta)|$ is an approximation for the field radiation pattern of the complementary strip-slot element, which is considered constant over frequency.

In this way, the radiation patterns shown in Fig. 4.11 can be computed. The solid line represents the radiation pattern when V_{slot} is extracted from electromagnetic simulation and inserted into (4.4) and the dashed line, when V_{slot} is extracted from the model using equivalent circuits. Good agreement is achieved, not only between the two curves, but also with the measured and the simulated ones shown in Fig. 4.6. Although higher grating lobes are obtained with the equivalent circuit model, the qualitative behaviour of the radiation is obtained, which can be very useful in preliminary steps of the design.

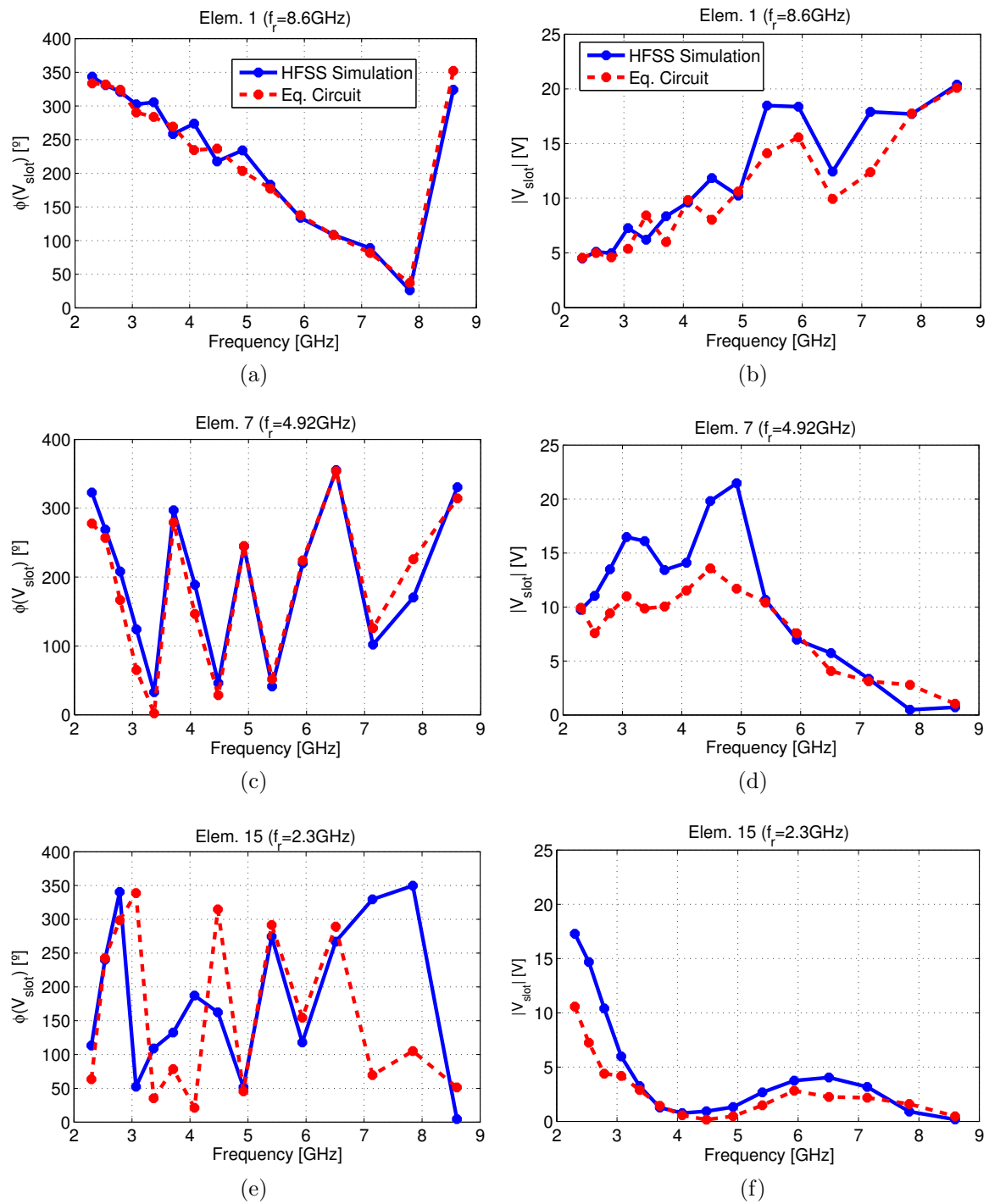


Figure 4.10: Phase and magnitude of the voltage drop across the slots of the elements 1, 7 and 15 over frequency. The solid line represents the one extracted from the HFSS simulation and the dashed line, from the model using equivalent circuits.

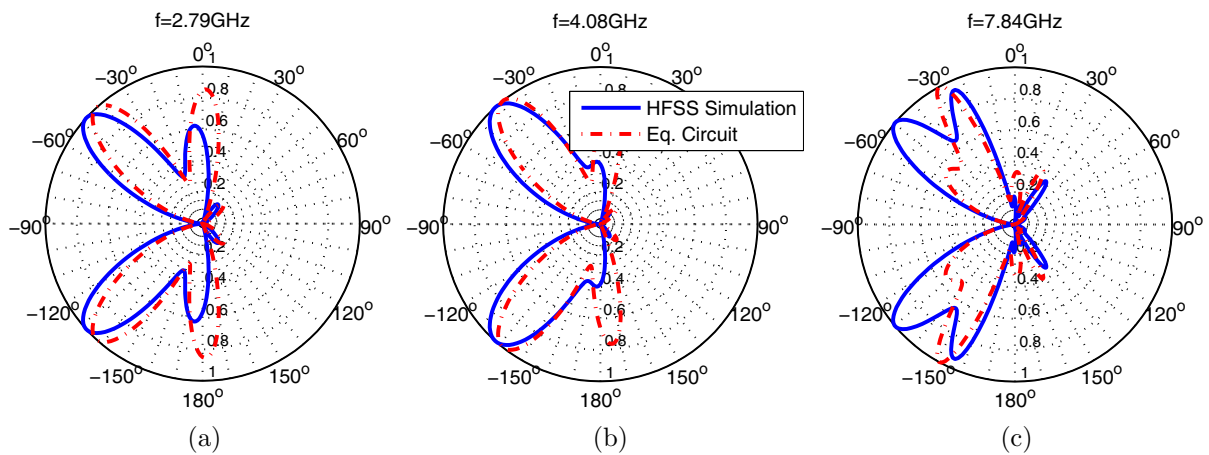


Figure 4.11: Computed radiation patterns of the log-periodic array, with V_{slot} extracted from the HFSS simulation (solid line) and from the equivalent circuit model (dashed line), for three frequencies which correspond to the characteristic frequencies of some of the elements ($f_r = 2.79, 4.08$ and 7.84 GHz).

4.6 BACK-RADIATION REDUCTION

As it has been seen in Section 4.4, the proposed array radiates into both half-spaces. However, a bidirectional pattern might limit some practical applications of this structure. If required, it would be possible to avoid the radiation in one of the half-spaces by introducing a reflector plane in the side of the face that the radiation is undesired [55] (as done in Section 3.2.4).

A low angle of the plane is required in order not to reflect the beam in a very different direction from that of the incident beam. Fig. 4.12 shows the log-periodic array with the reflector plane over the face of the strips. Some plastic screws have been used to join the array and the plane together. Fig. 4.13 shows the simulated and measured radiation patterns with the reflector plane inclined at an angle α (the same angle as that of the scaling of the elements) and at a height $\frac{\lambda_0}{2 \sin 45^\circ}$ over the smallest element at its corresponding characteristic frequency (8.6 GHz). Some modifications in the radiation patterns are perceptible, like higher grating lobes at some frequencies and some back radiation at the higher frequencies. Part of this can be attributed to the limited size of the reflector plane. However, it can be observed that it successfully removes the beam in the strips half-space, thus obtaining unidirectional radiation, without significantly altering the main beam direction.

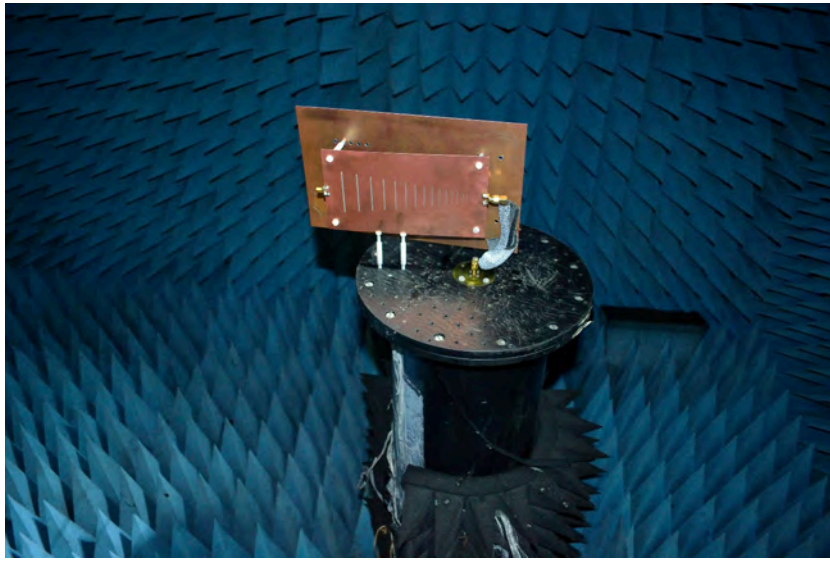


Figure 4.12: Fotografia of the proposed log-periodic array with the reflector plane.

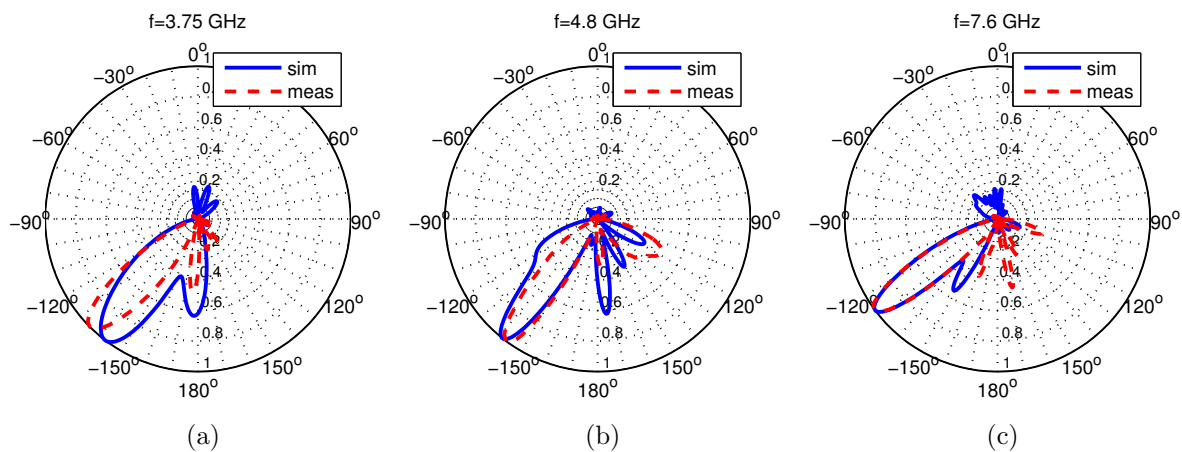


Figure 4.13: Simulated and measured radiation patterns of the proposed array with the reflector plane for different frequencies.

4.7 CONCLUSIONS

In this chapter, a new application of the complementary strip-slot element has been proposed: a log-periodic array. Since, the basic element is not resonant, the approach for the design of the log-periodic differs from that of other planar log-periodic arrays, which follow the design methodology of dipole log-periodic arrays. Since all the elements of the array are matched, there is no need to add a phase shift of 180° between adjacent elements for achieving destructive interference in the reflections, as other log-periodic arrays need to do. Moreover, since the element radiation efficiency is not resonant, but high-pass, a smaller τ does not lead to poor radiation efficiency and

size reduction can be achieved. Therefore, this analysis might broaden the horizon of log-periodic arrays for broadband radiating elements.

A design example with a low τ (0.909) has been proposed. The slots follow the log-periodic progression while the strips are designed for guaranteeing impedance matching for each element. The array radiates backwards with an angle of 45° , approximately, with bidirectional patterns in both half-spaces. A bandwidth from 2.7 to 8.6 GHz has been obtained with 15 elements and a σ of 0.17. A radiation efficiency of more than 85% and a gain better than 5 dB over the whole operating bandwidth have been reported. Moreover, it has been checked that the termination does not have any effect on the correct operation of the array.

A proposed method for computing the radiation of this array, based on the equivalent circuit of the element and the scaling of the radiation resistance, has been proven to be a useful tool to estimate the performance of the array without the need for the high-computational load electromagnetic simulation. Additionally, the possibility of avoiding bidirectional radiation by adding a reflector plane on one of the sides of the array has been discussed. Results with the reflector plane show that it would be possible to remove the radiation in one half-space without significantly altering the radiation pattern. Further research must be carried out for finding the best configuration of the reflector.

The proposed structure is a broadband antenna, inexpensive and single-layer that does not need to be terminated in matched load. Therefore, it can play an important role in the need for wideband antennas, for massive data transmission or for frequency reconfiguration, since it is possible to add additional circuitry on the microstrip layer without modifying the antenna itself.

Chapter 5: Strip-Slot-Based Sequentially Rotated Array

The previous two chapters have been devoted to exploiting the special features of the complementary strip-slot by means of the design of arrays with interesting performances. This chapter continues this line and deals with the last array concept assessed in this thesis: a sequentially rotated ring array with both multiband behaviour and polarisation agility. The chapter is structured as follows. Section 5.1 reviews the literature in this topic and explains the motivation for this concept. Section 5.2 describes the antenna geometry, the design methodology and the different modes of operation regarding polarisation. Section 5.3 proves the concept through an arbitrary design, its characterisation with simulated and experimental results of both polarisation modes (circular and linear), and an experimental demonstration of the polarisation versatility of the structure. In order to highlight the potential of the antenna, Section 5.4 applies the concept to the design of an antenna for Global Navigation Satellite Systems (GNSS) with dual-band and self-diplexing capabilities. Finally, Section 5.5 summarizes the main conclusions.

5.1 MOTIVATION

Polarisation reconfiguration is a powerful tool for enhancing the performance of a radio system. Having an antenna that can generate a radiation pattern with an arbitrary polarisation can be interesting for avoiding an undesired interfering signal by switching to an orthogonal polarisation, as well as decreasing the effect of multipath by adaptively switching to the best polarisation. In this way, the robustness and capacity of the whole system could be improved without additional circuitry or additional antennas in the transmitter or receiver (as in MIMO systems). Moreover, this technique can be

combined with any other, such as frequency multiplexing. That is why the so-called *polarisation agile antennas* are of great interest in research [56, 57].

The classic microstrip radiators, such as patches, radiate with linear polarisation (LP), although circular polarisation (CP) with these elements can also be achieved when two orthogonal modes are excited with the necessary phase difference. Nevertheless, arrays of linearly polarised elements are normally preferable, since they allow better polarisation purity, higher gain and radiation efficiency to be obtained. To achieve CP with linearly polarised elements, the sequential rotation technique can be used [58]. In this approach, N radiating elements are sequentially rotated and fed with a phase shift equal to the geometrical rotation angle $\frac{360^\circ}{N}$. There are multiple examples of patch arrays with CP that use this technique; however, most of them have a corporate feeding structure, which makes the use of additional circuitry mandatory to provide the necessary current phase shift between elements, thus increasing the complexity and cost of the antenna. On the other hand, series feeding with a transmission line has the advantage that the necessary phase shifts between elements are automatically generated if the feeding-line lengths are appropriately designed and more compact structures can be obtained, such in [59].

Sequentially rotated arrays have lately received more attention as potential agile antennas [60, 61, 62]. When an antenna, either consisting of a single element or an array, has two ports that excite two orthogonal modes in the structure, it is possible to generate different polarisation modes [63, 64, 65]. In a corporate sequentially rotated array, if different feeds are used for each element of the array, it is quite straightforward to switch from CP to LP, either horizontal or vertical, by switching off some of the radiating elements. However, in this case, the array factor changes from the case of CP to that of LP, which leads to different radiation properties, which is normally undesired. On the other hand, in a series-fed sequentially rotated array, either sense of circular polarisation (RHCP or LHCP) is available by exciting one port of the antenna and terminating the other port with a matched load. LP is also achievable when the structure is excited by the two ports simultaneously.

In [66], a ring patch array with sequential rotation technique and series feeding was proposed for CP. However, a slotline of 110Ω was used to feed the patches (due to the practical difficulty of implementing a 50Ω slotline) and the transition between the microstrip and the slotline required additional impedance transformers. In [61], the array of [66] was extended as an active antenna capable of switching between the two signs of circular polarisation and in [62], the same array was extended to switch

between LP and CP; however, LP was achieved by exciting only part of the elements (two patches in this case). The work of [66] was also extended in [67] for implementing a dual-circularly polarised array, by feeding the patches with two parallel slotlines, with opposite travelling directions.

Therefore, the capability of a two-port circularly polarised travelling-wave array to obtain different polarisation modes has been proved. However, obtaining dual-band or multiband behaviour while maintaining the polarisation agility properties seems to be a more challenging task, because planar agile antennas are made of resonant elements. For this reason, dual-band antennas with polarisation diversity are limited in the literature and the few examples available are based on a single modified patch. In [68], a dual-band antenna with different states of LP is proposed for WLAN systems; however, it is a multilayer patch that uses four shorting posts to adjust the two frequencies, with the resulting complexity in the geometry of the structure. Moreover, only parametric studies are available for designing the operating frequencies and no CP is achieved, only LP. In [69], a patch with a switchable slot is proposed for dual frequency operation, but only for the two signs of CP.

The complementary strip-slot does not suffer from the limitation of the narrow impedance bandwidth and, although it is linearly polarised, CP can be achieved by applying the aforementioned sequential rotation technique [58]. This radiating element has two important characteristics for building a novel array with polarisation agility. Firstly, the element has a microstrip series feeding, which allows a sequentially rotated array with a travelling-wave feeding to be built, thus simplifying the structure with respect to the corporate configuration and with no need of impedance transformers as in [66, 61, 62, 67]. Moreover, travelling-wave series feeding allows the excitation of the array through two ports, which in turn allows the generation of vertical LP (VLP), horizontal LP (HLP), RHCP and LHCP, just by controlling the phase and amplitude of the excitations at the two ports. Secondly, the element is broadly matched, which means that the operation bands are not restricted to the resonance frequencies of the radiating element, but the array can operate at every frequency at which the phase conditions for sequential rotation are fulfilled. Both features combined in one structure lead to an appealing antenna that can find demand in the emerging applications. An example is found for GNSS, in which antennas for the competitive navigation receivers must be able to simultaneously receive signals from different satellite constellations that are transmitted in different bands with the same sign of CP.

5.2 MULTIBAND ARRAY WITH POLARISATION AGILITY

Thanks to the inherent series feeding configuration of the complementary strip-slot radiating element, a sequentially rotated array can be easily implemented as a travelling-wave antenna, as Fig. 5.1 illustrates. A circular microstrip line is feeding the radiating elements, which are sequentially rotated 90° . The microstrip line is terminated in two ports.

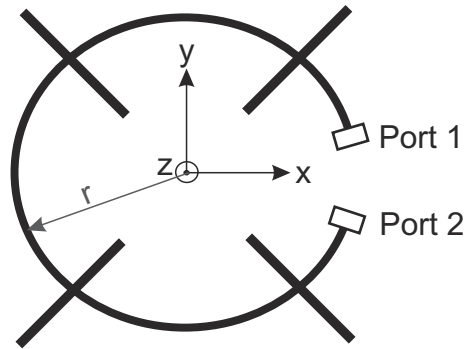


Figure 5.1: Configuration of the proposed ring array.

5.2.1 Design

The design of the proposed array is carried out with the objective of achieving CP when the antenna is fed by one port. In order to obtain CP with four linearly polarised elements, according to the sequential rotation technique [58], a phase shift of 90° or 270° between adjacent elements must be introduced. Therefore, the phase contributions of both the interconnecting microstrip line section ($\phi_{\mu strip}$) and the radiating element ($\phi_{element}$) must satisfy the following condition:

$$\phi_{total} = \phi_{\mu strip} + \phi_{element} = (2n + 1) \frac{\pi}{2}. \quad (5.1)$$

The phase shift that a microstrip line section between two elements introduces, when series circular feeding is applied, is given by:

$$\phi_{\mu strip}(f) = \frac{\pi r}{2} \beta_{\mu strip}(f) \quad (5.2)$$

where $\beta_{\mu strip}$ is the phase constant of the microstrip line and r is the radius of the ring

microstrip line, in accordance with Fig. 5.1.

In addition, a theoretical model for the phase shift that the element introduces was obtained in (2.5). Therefore, the theoretical phase shift between elements can be calculated.

For an arbitrary dual-band design, the degrees of freedom are the geometry of the element, which determines (2.5), and the radius of the microstrip feed line, which fixes (5.2). The total phase shift introduced by one element and the microstrip line section between elements must be 90° and 270° at the two design frequencies, respectively, as (5.1) indicates. Therefore, these two equations must be satisfied simultaneously by choosing the element geometry and the microstrip radius. However, it is important to point out that the phase response of the element can only be designed to some extent, because it depends on the even- and odd-mode parameters, which must correspond to a realizable geometry.

5.2.2 Modes of Operation

As aforementioned, the sequentially rotated array with series feeding and two ports allows the generation of different polarisation modes by choosing the appropriate feeding. When one port is excited and the other port is matched, the radiated wave has CP when condition (5.1) is fulfilled. The sense of the polarisation can be chosen by selecting the corresponding port. Since the radiating element (the complementary strip-slot) is broadly-matched and CP is obtained at all those frequencies where the phase shift between elements is 90° , or alternatively, 270° (with opposite CP sign to that with 90°), multiband behaviour can be obtained.

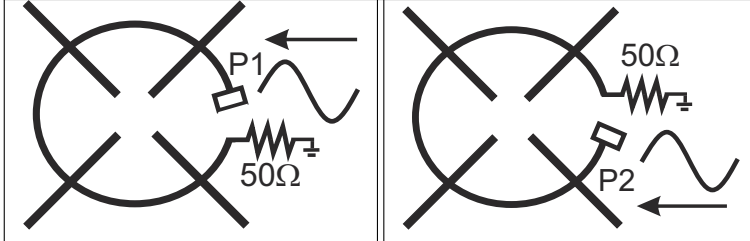
It is well-known that LP can be generated as the superposition of two orthogonal CP waves:

$$\vec{E} = \hat{y}e^{-j\beta z} = \left(\frac{\hat{y} + j\hat{x}}{2} + \frac{\hat{y} - j\hat{x}}{2} \right) e^{-j\beta z} \quad (5.3)$$

where a linearly polarised wave in the y -axis, travelling in the direction of z with a phase constant β , has been separated into the addition of two CP waves. This property can be used in the proposed antenna to generate LP by exciting the antenna by the two ports simultaneously. Moreover, it is evident that different orientations of LP can be obtained by applying the appropriate phase difference between the ports. In this way, if the two ports are excited with anti-phase waves instead of in-phase, the orthogonal direction of LP is obtained.

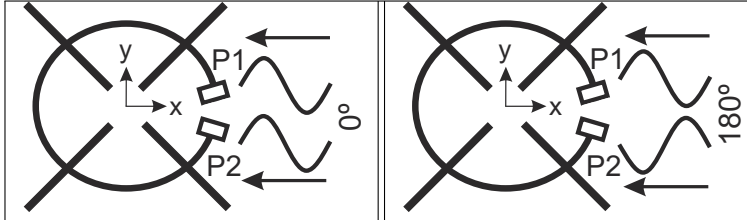
Tables 5.1 and 5.2 summarise the main modes of operation regarding polarisation along the z-axis for a general case with three operating frequencies (f_1 , f_2 and f_3), at which the condition (5.1) is fulfilled. Table 5.1 collects those for CP, whereas Table 5.2 those for LP. For CP, single excitation with the other port terminated in a matched load is required. The sign of polarisation depends on the phase shift between elements (either 90° or 270°) and the side of the structure (slot or strip), since the current flow sign depends on the observation side. In this way, it can be observed in Table 5.1 that the sign of polarisation alternates in the different operating bands and in the two sides of the structure. When the structure is excited by the other port, the opposite sign is obtained. For LP, the structure must be excited by the two ports simultaneously. Two orthogonal LP modes can be obtained with dual excitation: when the two ports are fed in-phase, the radiated field along the z-axis is polarised in the x-direction, whereas for anti-phase excitation, the radiated field is polarised in the y-direction. In the case of LP, no alternation in the polarisation is obtained for the different operating bands, as expected from (5.3), since although the sign of CP polarisation changes when feeding at one port, the superposition of both CP-waves from both ports leads to the same LP direction.

Table 5.1: Configurations for circular polarisation.



	Slot Side	Strip Side	Slot Side	Strip Side
@ f_1	RHCP	LHCP	LHCP	RHCP
@ f_2	LHCP	RHCP	RHCP	LHCP
@ f_3	RHCP	LHCP	LHCP	RHCP

Table 5.2: Configurations for linear polarisation.



	Slot Side & Strip Side	
@ f_1, f_2 & f_3	LP in x-axis	LP in y-axis

5.3 PROOF OF CONCEPT

For building an example of the circular array proposed here, the design of Prototype 2 of Section 2.4.1 has been used. In order to confirm the validity of the theoretical approach, $\phi_{element}$ has been obtained separately from (2.5) and from measurements. Fig. 5.2 represents the required radius r of the ring feed microstrip line for fulfilling condition (5.1):

$$r = \left[(2n - 1) \frac{\pi}{2} - \phi_{element}(f) \right] \frac{2}{\pi \beta_{\mu strip}(f)}. \quad (5.4)$$

The curve in blue is calculated theoretically using (2.5) and the one in red is obtained when $\phi_{element}$ in (5.1) is extracted from the measurement of a single element. It can be observed that, practically, no difference is obtained between the theoretical model and the simulation.

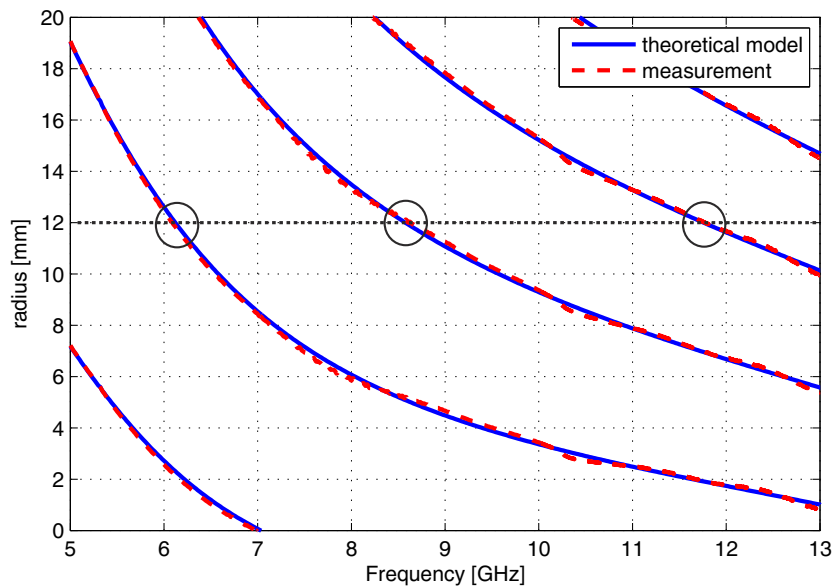


Figure 5.2: Required radius of the proposed ring array for CP at each frequency, in accordance with (5.1). The chosen radius of 12 mm is marked, together with the resulting frequencies of operation.

A design of the ring array has been carried out at 6.2 GHz. In order to be able to obtain CP at this frequency and with the element of Section 2.4.1, the radius of the microstrip feed line has been set to 12 mm, in accordance with Fig. 5.2. Additionally, multiband behaviour of the antenna with CP is expected, since condition (5.1) is also fulfilled around 8.6 and 11.7 GHz. The working frequency bands have not been chosen according to any specifications, but given the radiating element geometry of Section 2.4.1, which had been previously characterised, and pursuing minimum size of the

antenna. The manufactured prototype is shown in Fig. 5.3. It consists of a two-port ring array made up of four identical complementary strip-slot elements. The sequential rotation technique is applied in a simple travelling-wave form, with series feeding. The two ports connected to the microstrip line have been placed in two orthogonal axes of symmetry to facilitate the radiation measurements in the anechoic chamber. The purpose of the curved microstrip sections is to reach the connectors with small length and large radius. Their geometry practically does not affect the antenna performance.

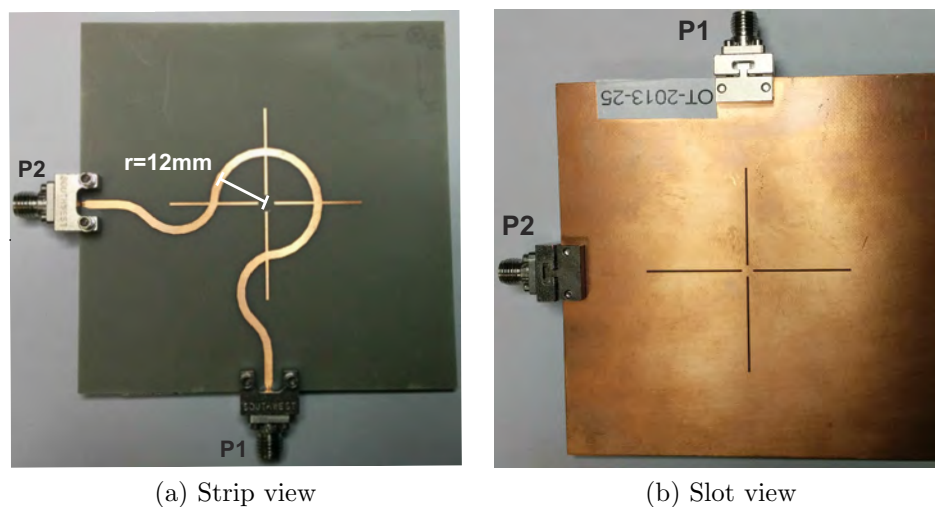


Figure 5.3: Layout of a manufactured antenna.

5.3.1 Results

In this section, simulated and experimental results¹ are shown for the two available polarisations: CP, with single excitation, and LP, with dual excitation.

Circular Polarisation

The antenna has been measured when one port is terminated in a matched load. Fig. 5.4 shows both measured and simulated reflection coefficient over a wide bandwidth, with the operating bands delimited in the figure. It is highlighted that the antenna is very well matched over the bands where CP is expected according to theory: around 6.2,

¹The radiation measurements were taken in the anechoic chamber of the Laboratorio de Ensayos y Homologación de Antenas, Universidad Politécnica de Madrid, Madrid (Spain).

8.6 and 11.7 GHz. In general, the return losses are better than 10 dB, except for some bands around 5.5, 10.5 and over 14 GHz. These bands are mismatched because they correspond to the frequencies where $\phi_{total} = 0^\circ$ and as a result the small mismatches from each element are added constructively, resulting in poor matching. However, for CP, the bands around $\phi_{total} = 90^\circ$ or 270° are used. It must also be pointed out that very good agreement is obtained between simulation and measurement.

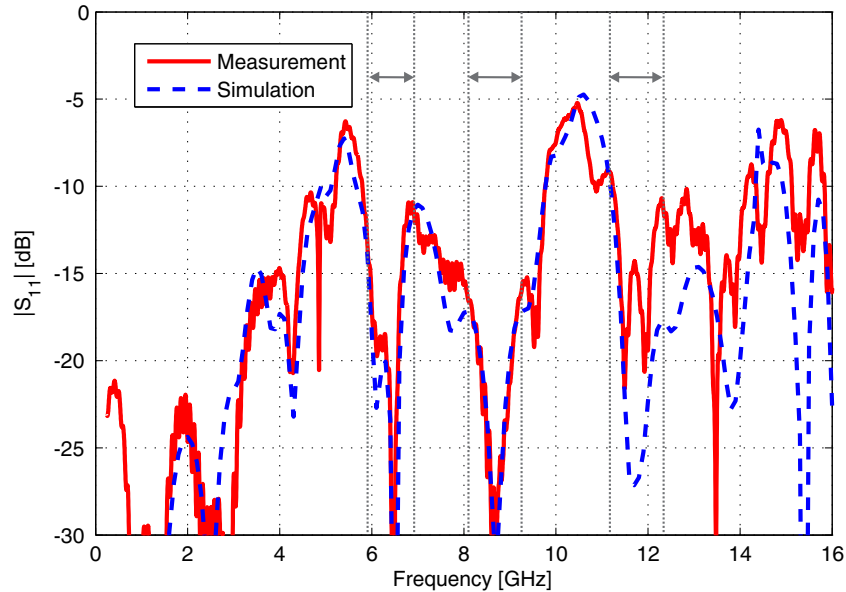


Figure 5.4: Simulated and measured $|S_{11}|$ of the ring array of Fig. 5.3. The operating bands are delimited.

Fig. 5.5 shows the axial ratio at broadside for the three bands in which, according to theory, CP is expected. In fact, axial ratios of less than 3 dB are obtained, which indicate good polarisation purity. Slight differences are noticeable between the simulation and measurement, although, in general, the same behaviour is reproduced.

In order to quantify the cross-polarisation levels and observe how the sign of polarisation changes with frequency, Fig. 5.6 plots the polarisation ratio ($\frac{RHCP}{LHCP}$) over the three analysed bands at broadside. The alternation of the polarisation sign between bands as well as for the two opposite directions can be observed. Cross polarisation levels around 20 dB are obtained in the slot half-space, whereas some lower values are attained in the strip side.

Fig. 5.7 shows the radiation patterns in a constant-azimuth plane (good rotation symmetry around z-axis has been checked) at each of the operating bands, with both the RHCP and LHCP components of the radiated field. The axes are those defined in Fig. 5.1, with $\theta = 0^\circ$ pointing to the broadside over the strip side. Good agreement

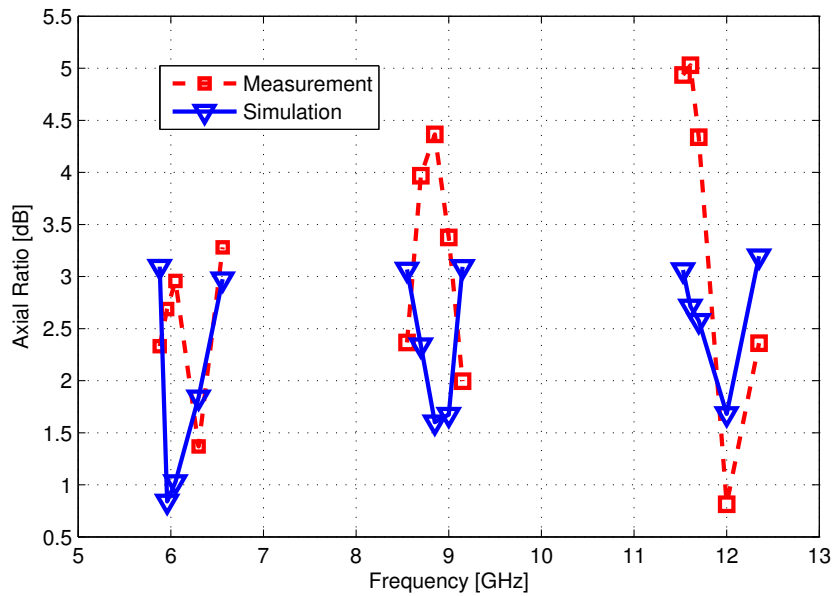


Figure 5.5: Measured and simulated axial ratio at broadside of the ring array of Fig. 5.3 over the three studied frequency bands.

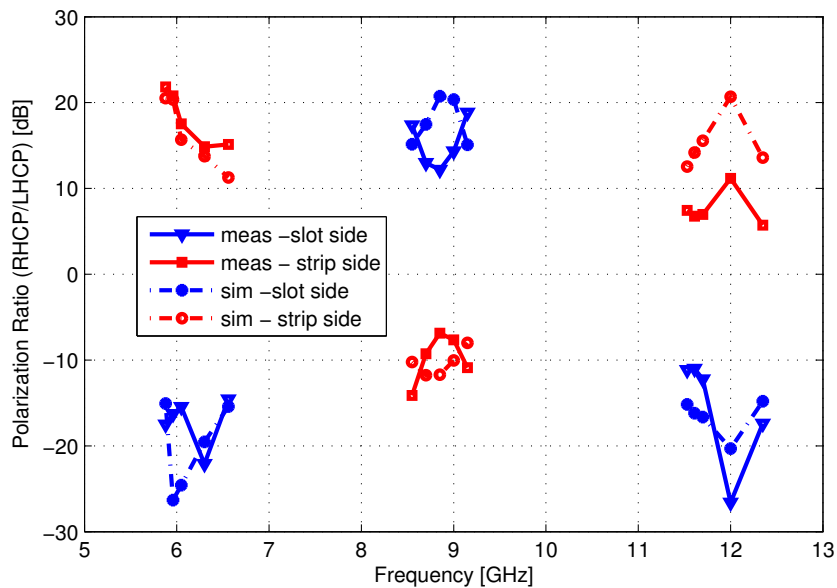


Figure 5.6: Measured and simulated polarisation ratio for single excitation over the three studied frequency bands. The red curves correspond to the broadside direction towards the strip face and the blue curves, towards the slots.

is obtained between the simulations and measurements. Moreover, the alternation of polarisation signs between consecutive operating bands and for the two half-spaces (slot and strip side) is also noticeable. At broadside, one of the signs of CP has its maximum whereas the other sign (cross-polar) has the minimum value, thus indicating good CP with broadside radiation. As long as the radiation direction is shifted from broadside,

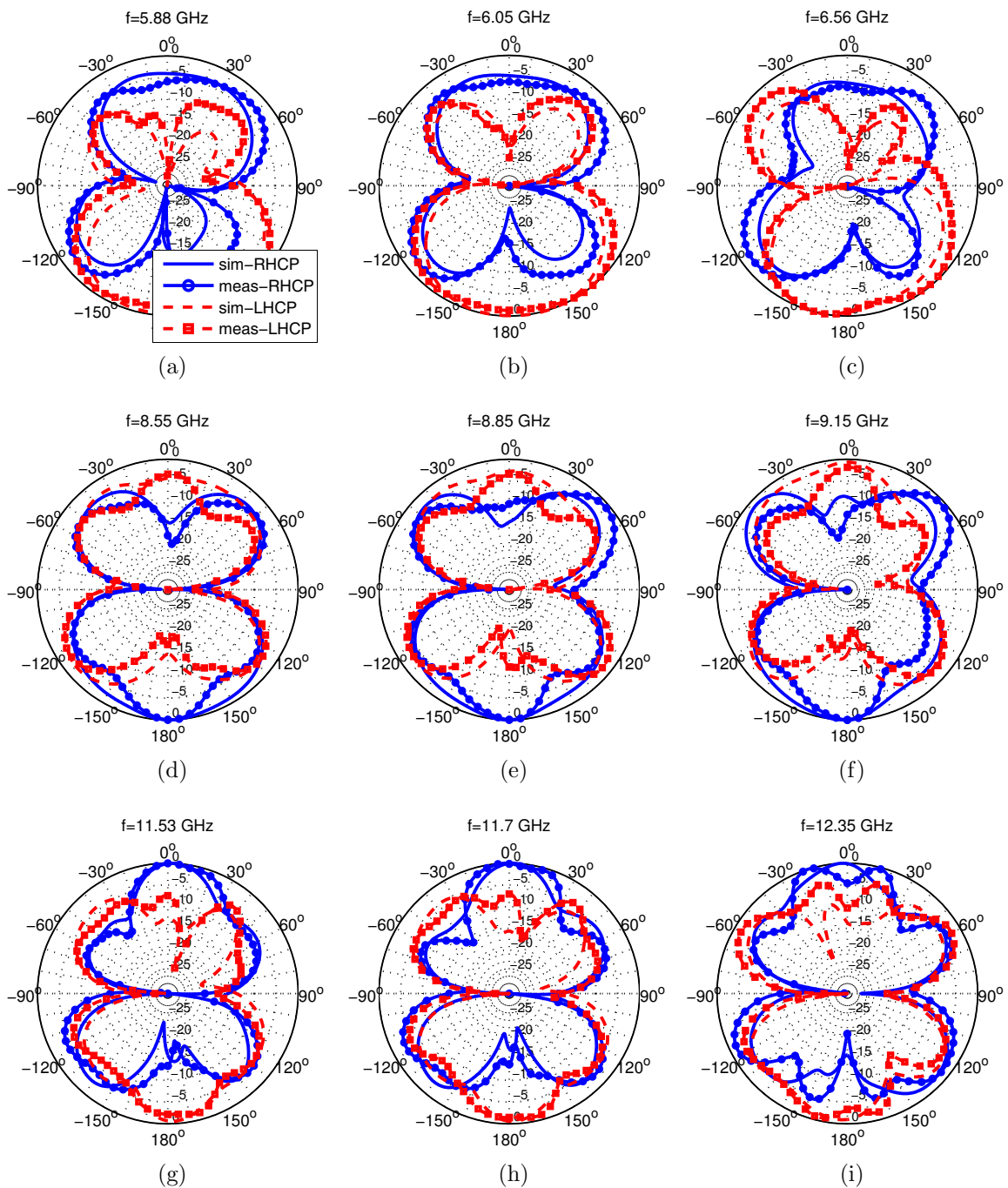


Figure 5.7: Measured and simulated radiation patterns in dB at the three studied frequency bands for single excitation in a constant-azimuth plane. The broadside direction towards the slot face corresponds to $\Theta = 180^\circ$.

the CP deteriorates, as it is expected from the sequential rotation technique, which is conceived to provide CP at broadside. The array radiates with slightly more intensity towards the slot half-space ($\theta=180^\circ$) than to the strips at the two lower bands, which is a consequence of the radiation characteristics of the single element.

Linear Polarisation

The antenna has also been simulated and measured by exciting the two ports simultaneously with the same amplitude, in order to characterise its performance with LP. A power divider has been used for this purpose, as detailed in Fig. 5.8.

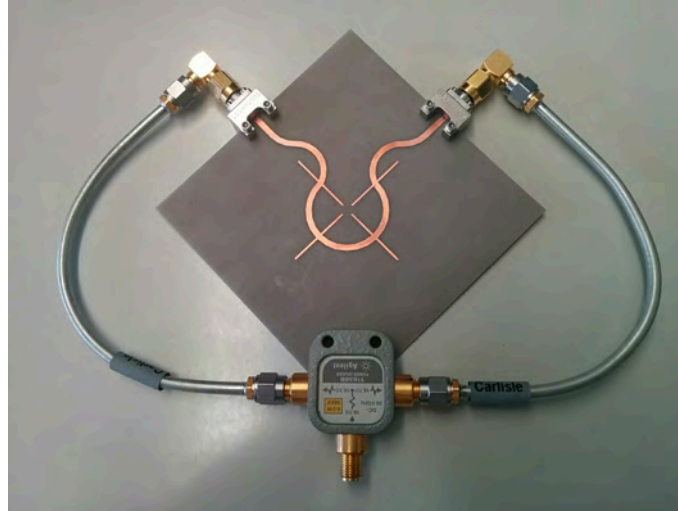


Figure 5.8: Measurement setup for LP.

Fig. 5.9 plots the polarisation ratio (E_ϕ/E_θ) over the three analysed bands at broadside and $\phi = 90^\circ$. Except for the higher frequency limit of the third operating band, polarisation ratios better than 15 dB are obtained. Therefore, it is proven that LP can be achieved with simultaneous port excitation. No simulations have been included, since simulation results predict a polarisation ratio better than 45 dB over the whole band. This disagreement between simulation and measurement can be attributed to the presence of the bulky power divider and the connecting cables in the measurement setup (see Fig. 5.8), not included in the simulations.

Fig. 5.10 shows the radiation patterns in a constant-azimuth plane ($\phi = 90^\circ$) for dual excitation, with both copolar (E_ϕ) and crosspolar (E_θ) components of the radiated field. Good agreement is obtained between simulations and measurements. It can be observed that the antenna radiates broadside with low cross-polarisation levels. Deterioration in the polarisation purity is found at the high limit of the frequency bands. It is worth mentioning that those high cross-polarisation levels are due to the non-symmetry of the structure with respect to the measured plane $\phi = 90^\circ$. In fact, the measured radiation patterns at $\phi = 0^\circ$ have lower cross-polarisation levels; however, the radiation patterns are less symmetric with respect to broadside, since, at this plane, the structure is not symmetric around the z-axis, with the bulky power divider at $\theta = -90^\circ$.

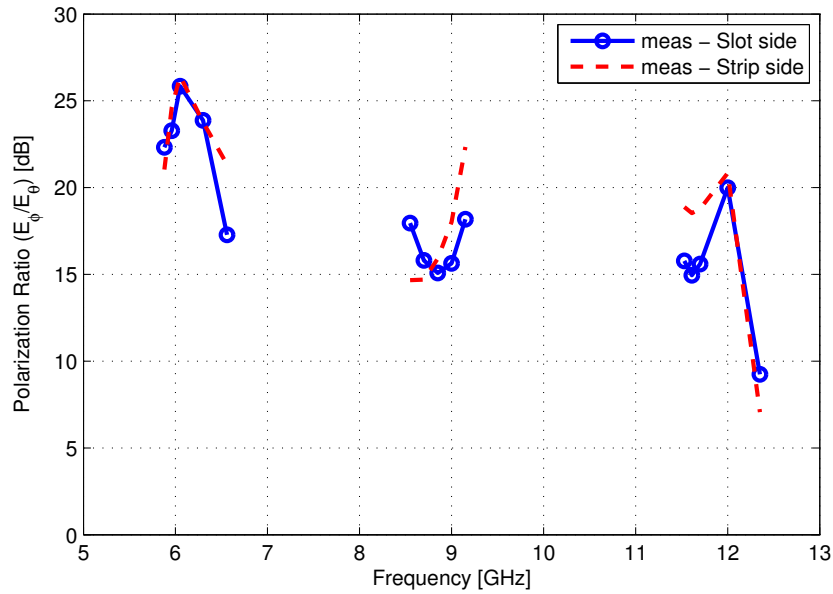


Figure 5.9: Measured polarisation ratio over the three studied frequency bands at broadside and $\phi = 90^\circ$ for dual in-phase excitation. The red curve corresponds to the broadside direction towards the strip face and the blue curve, towards the slots.

Anyway, very good radiation patterns are obtained with low cross-polarisation levels at the centre of the operating bands, thus proving that the antenna can be used with dual excitation for LP and broadside radiation. Better results will be likely obtained with a power divider in planar technology integrated with the antenna.

Finally, Fig. 5.11 shows the radiation efficiency for both characterised cases: CP and LP. It can be observed, that the antenna is capable of radiating more than 80% in the two modes of operation and over the three operating bands.

5.3.2 Experimental Demonstration

As has been shown, different excitations can result in different modes of operation over three different bands. The aim of this section is to highlight the versatility of this simple and low-cost structure with the measurement setup shown in Fig. 5.12. Two antennas are connected to a 4-port PNA-X network analyzer N5247A, capable of generating differential and common signals and measuring differential S-Parameters.

Fig. 5.13 shows the transmission coefficients when two identical prototypes of the proposed antenna are connected in the measurement setup of Fig. 5.12. Ports P1 and P3 belong to the transmitting antenna and P4 and P2 are the respective ports

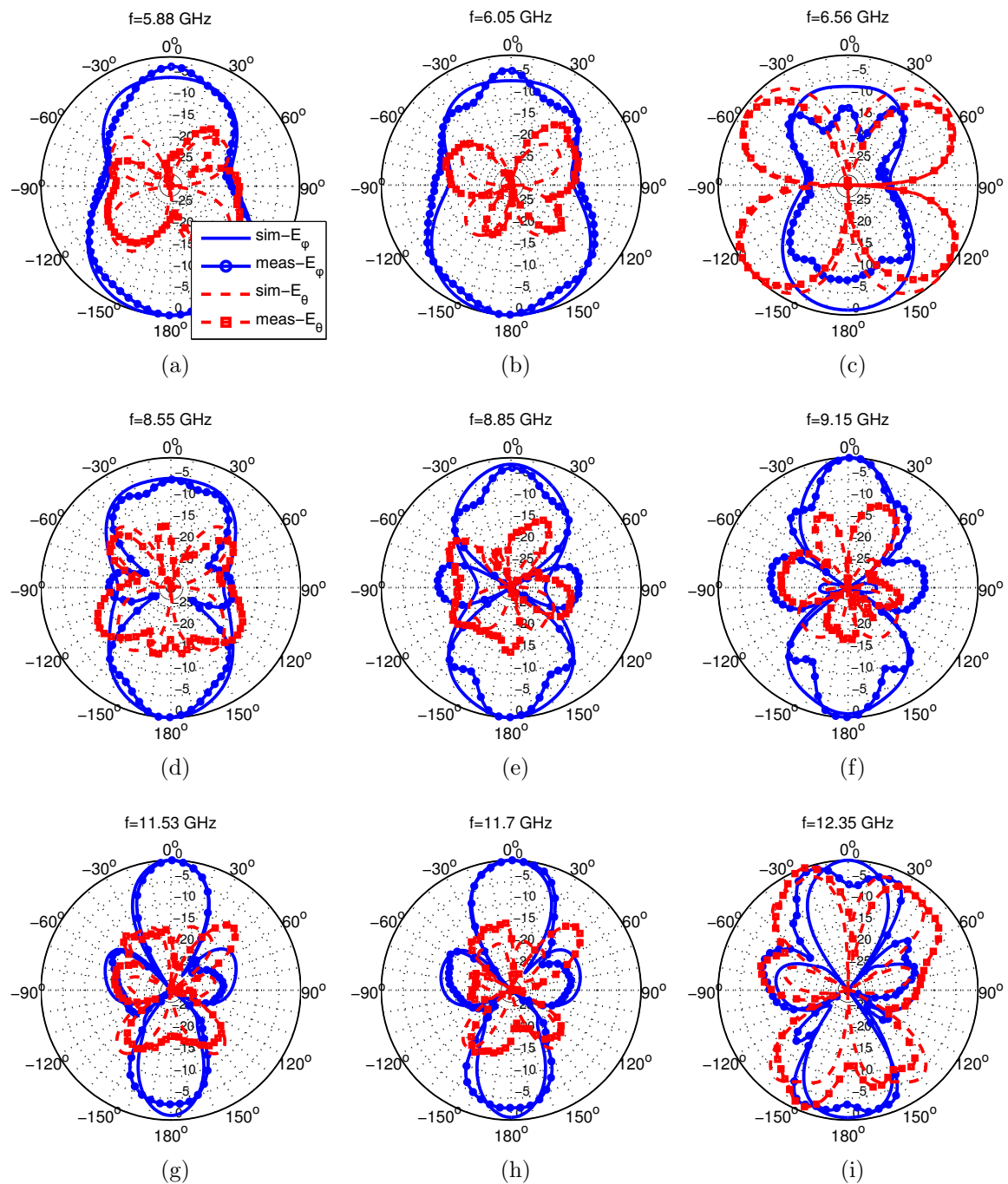


Figure 5.10: Measured and simulated radiation patterns in dB at the three studied frequency bands for dual in-phase excitation at a constant-azimuth plane ($\phi = 90^\circ$). The broadside direction towards the slot face corresponds to $\Theta = 180^\circ$.

in the receiving one. It can be observed that the signal transmitted by P1 is received in P4, which corresponds to the same sign of polarisation, whereas low signal level (about 10 dB lower) is received at P2. Likewise, the signal from the other port of the transmitting antenna, P3, is received in P2, but not in P4. This result indicates that

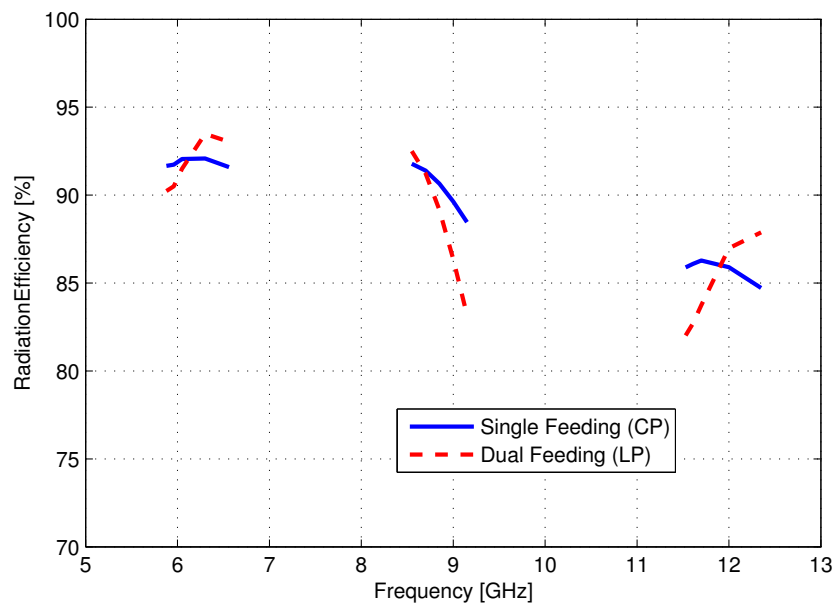


Figure 5.11: Simulated radiation efficiency over the three studied frequency bands. The blue curve corresponds to the single feeding (CP) and the red curve to the dual feeding (LP).

the two ports of the transmitting antenna transmit orthogonal polarisation modes, which allows the reception of both modes simultaneously at two different ports in the receiver when the same antenna is used.

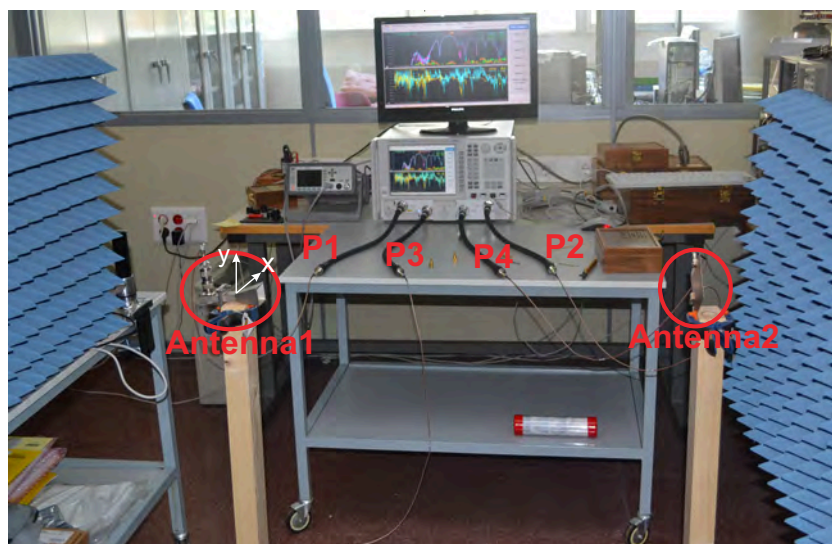


Figure 5.12: Measurement setup.

Therefore, the orthogonality in polarisation in the two ports can be used to transmit two channels at the same frequency, thus having self-diplexing behaviour with no additional cost or complexity. Nevertheless, this possibility will depend on the required cross-polarisation levels of the corresponding application. The self-diplexing capability

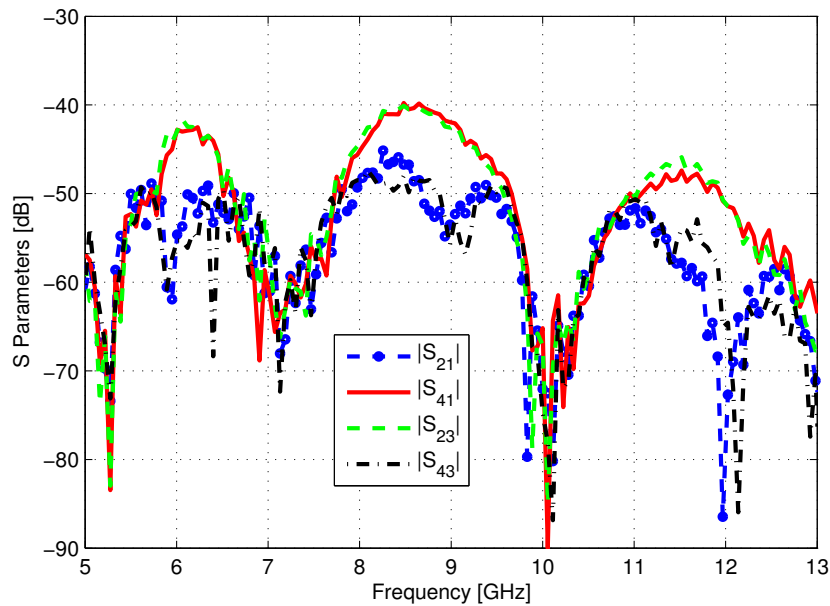


Figure 5.13: Transmission coefficients, when two identical proposed antennas are inserted in the setup of Fig. 5.12. P1 and P4 are the same port in the two different antennas, as well as P3 and P2.

of the antenna can be also used for transmitting through P1 with a polarisation sign and for receiving through P2 with the orthogonal polarisation.

Additionally, the multiband behaviour can be used to receive two signals at different frequencies with the same polarisation sign and diplex them through the two ports, as will be highlighted in Section 5.4. For example, in the proposed design, two signals with RHCP at 6 and 9 GHz could be received simultaneously, the first one at P1 and the other one at P2.

Fig. 5.14 plots the transmission coefficient between a horn antenna and the proposed ring antenna when the two ports P2 and P4 of the ring antenna are combined in-phase (common mode), in anti-phase (differential mode) and with single port excitation (P2 is excited and P4 is terminated by a matched load). In this case, the ring antenna is oriented with the x-axis of Fig. 5.1 in the vertical position, which is the polarisation direction of the horn antenna. The signal is received with maximum magnitude when P2 and P4 are combined in-phase and over the bands at which the single-fed proposed antenna radiates with CP (see Fig. 5.5). Minimum values are obtained when they are combined with a phase shift of 180° . In this case, the ring antenna orientation is the appropriate for receiving with VLP with common mode, according to Table 5.2. With single port signal, the ring antenna is working with CP and due to the polarisation loss factor it receives 3 dB less than in the common mode,

which can be observed in Fig. 5.14.

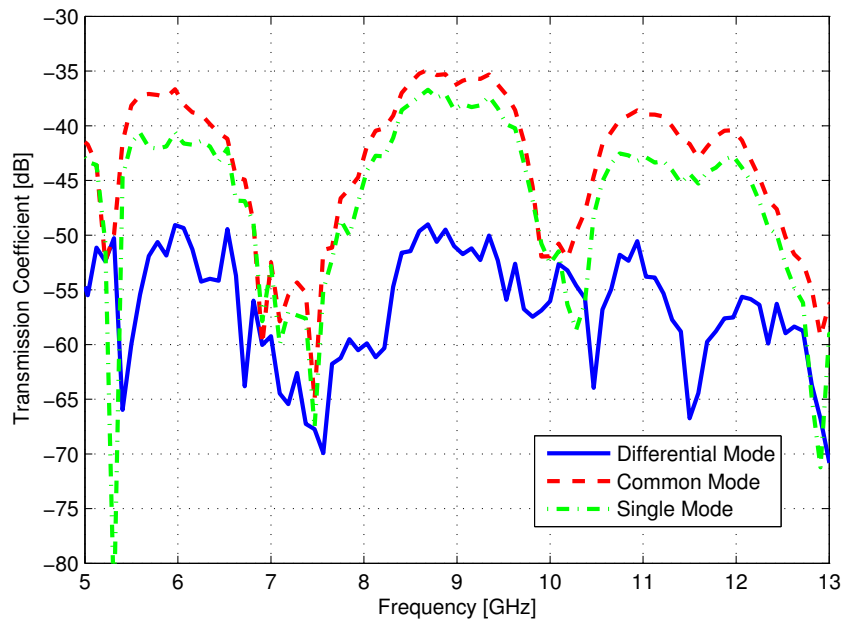


Figure 5.14: Transmission coefficients between the horn antenna and the proposed ring antenna when the two ports P2 and P4 of the ring antenna are combined in-phase (common mode), in anti-phase (differential mode) and not combined (signal at P2 when P4 is terminated by a matched load).

When the ring antenna is rotated 90° , the obtained transmission coefficients are those shown in Fig. 5.15. As expected, it is now the differential mode which receives the maximum signal level, because it generates VLP.

5.4 APPLICATION: A GNSS SELF-DIPLEXING DUAL-BAND ANTENNA

With the widespread use of the Global Positioning System (GPS) and the recent proliferation of other GNSS, the need for antennas capable of the simultaneous reception of satellite signals in the different working bands is increasing. Planar technology has proven to be the best candidate for GPS antennas, due to its compactness, light weight and low profile. However, since microstrip antennas are resonant in nature, the multiband behaviour requires additional complexity in the design, thus increasing the cost. However, the previous antenna concept can be used to design an antenna capable of simultaneously receiving two radionavigation bands: the E5 Galileo/L5 GPS band (1176-1207 MHz) and the L1 GPS/E1 Galileo band (1563-1587 MHz) and diplexing them in the two ports without the need for any other passive or active components.

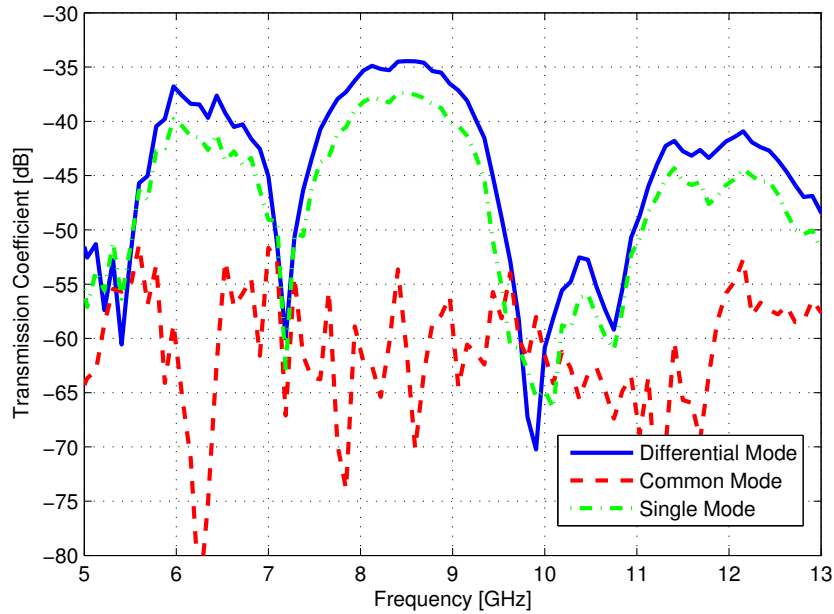


Figure 5.15: Transmission coefficients between the horn antenna and the proposed ring antenna rotated 90° with respect to Fig. 5.14, when the two ports P2 and P4 of the ring antenna are combined in-phase (common mode), in anti-phase (differential mode) and not combined (signal at P2 when P4 is terminated by a matched load).

For this purpose, the design consists in choosing a microstrip radius and element geometry in order to get a 90° phase shift between elements at the first central frequency ($f_1=1.19$ GHz) and 270° at the second one ($f_2=1.57$ GHz). Since both bands use RHCP, and a phase shift of 270° (instead of 90°) leads to a change in the sign of polarisation, the fact of having two ports allows the two bands to be diplexed: RHCP will be received through P1 at f_1 and through P2 at f_2 .

The GIL 1022 substrate was used for the design. The element geometry was chosen to have a slot length of $\frac{\lambda}{4}$ at 1.2 GHz and the required widths for a $50\ \Omega$ impedance level and for adjusting the phase shift in the second band. Finally, the chosen widths of the slot and strip were 1.50 and 1.51 mm, respectively, which achieved a phase shift between adjacent radiating elements of 90° for 1.19 GHz and 270° for 1.57 GHz with a circular microstrip line of radius 75.8 mm. The resulting lengths of the slot and strip were 99 and 84 mm, respectively. The manufactured prototype can be seen in Fig. 5.16. Although for the presented breadboard, the resulting size might be a constraint, it can be significantly reduced by choosing a substrate with higher permittivity (e.g., a ceramic substrate), as commonly done for GPS antennas.

The reflection coefficient at one port of the antenna has been measured when the other port was terminated in matched load. Fig. 5.17 shows good agreement between

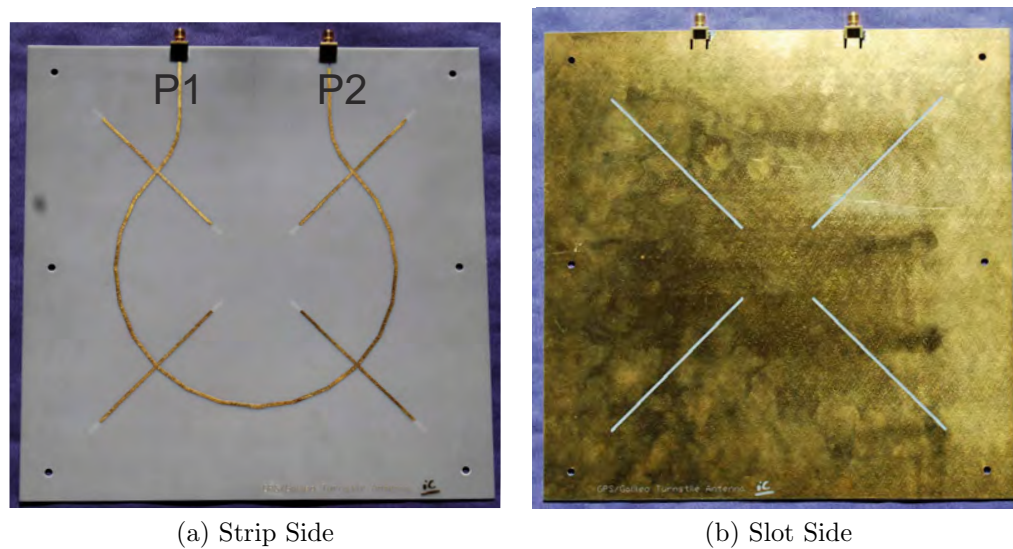


Figure 5.16: Photograph of the manufactured antenna.

the simulation and measurement and very good matching over the design bands.

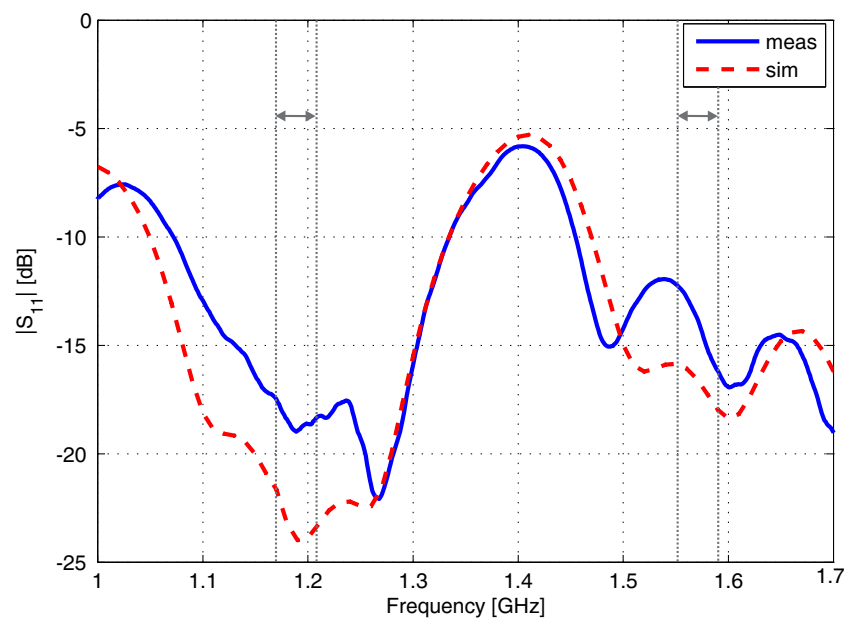


Figure 5.17: $|S_{11}|$ comparison between measurement and simulation.

Fig. 5.18 shows the simulated and measured² axial ratio at broadside (slot side, $\theta = 180^\circ$) over the two design bands. It can be observed that good CP purity is obtained, with worse behaviour at the limits of the bands. Since no optimisation in the design has been made, these values could be improved. The slight disagreement between the

²The radiation measurements were taken in the anechoic chamber of the Laboratorio de Ensayos y Homologación de Antenas, Universidad Politécnica de Madrid, Madrid (Spain).

measurements and simulations is mainly attributed to the anechoic chamber, which was used out of its recommended frequency range.

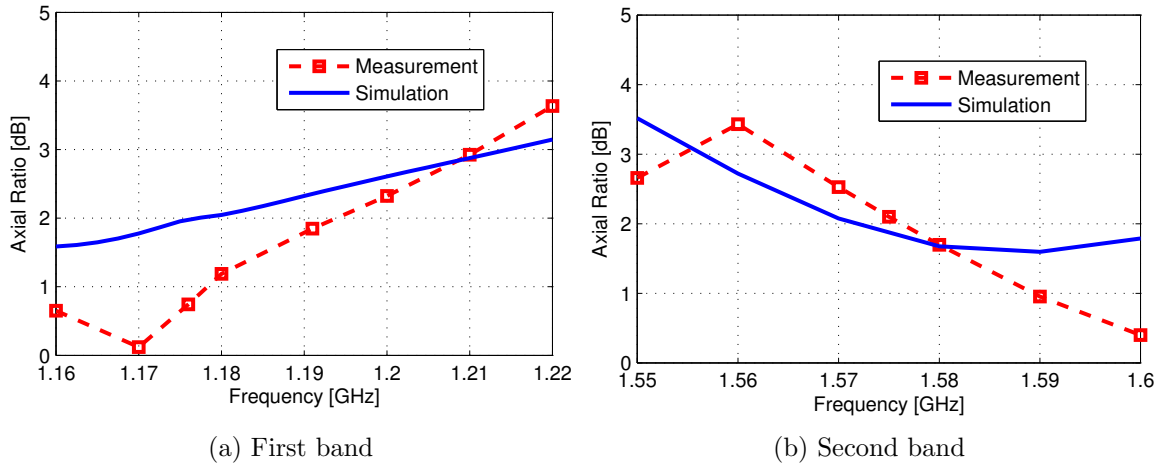


Figure 5.18: Axial ratio comparison between measurement and simulation at broadside for the two design bands.

Fig. 5.19 shows the simulated and measured radiation patterns (RHCP and LHCP) in a constant-azimuth plane ($\phi = 0$) at both central frequencies. It can be observed that, at the first central frequency, the slot half-space receives with RHCP while the strip half-space with LHCP, when P1 is used. The same occurs at the second central frequency when the reception is made by P2. This behaviour is in accordance with Table 5.1. In this design, the antenna works properly through the slot side, receiving both bands in different ports.

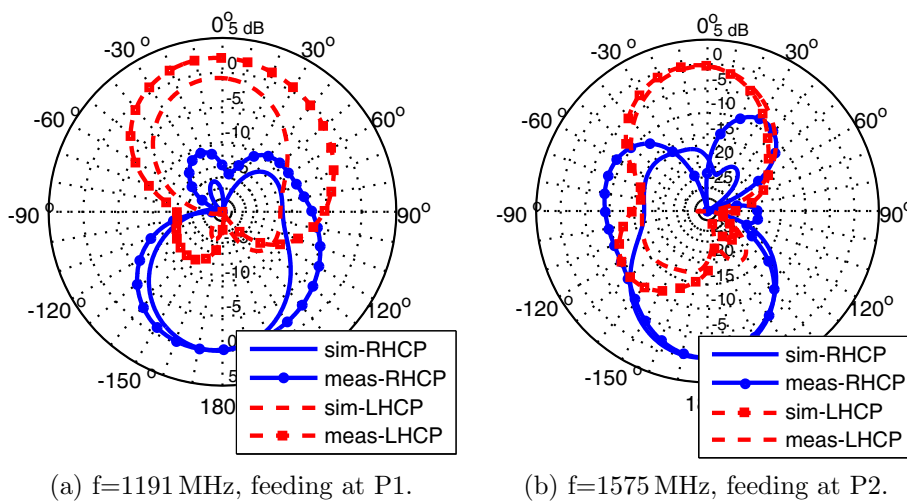


Figure 5.19: Simulated and measured radiation patterns ($\phi = 0$).

Finally, this antenna was connected to a single-band L1 GPS receiver, in substi-

tution of the commercial antenna, and placed outdoors, in order to check whether the satellite signals were received. With the use of a low-noise amplifier connected at the antenna port, between the antenna and the receiver, the satellite signals could be successfully received and the position of the receiver could be estimated.

5.5 CONCLUSIONS

A travelling-wave ring antenna with series feeding, based on the novel complementary strip-slot element has been proposed as a low-cost, single-substrate and low-profile antenna for polarisation reconfigurability with multiband behaviour. By applying the sequential rotation technique, both LP and CP can be generated with this linearly polarised element. The series feeding configuration allows the implementation of the required phase shifts between elements with just a microstrip line. Moreover, it allows a two-port antenna to be implemented, which is the key feature for polarisation agility. Multiple modes of operation regarding polarisation have been proven by just selecting the appropriate excitation of the two ports. Single excitation leads to CP, whereas dual excitation can generate LP, when the same signal is introduced by the two ports, or two orthogonal CP waves when different channels are desired to be transmitted.

A design methodology has been established and a design example has been manufactured as a proof of concept, obtaining very good results without the need of further optimisation. Therefore, it is expected that better performance is obtained with optimisation. The prototype has been characterised with simulation and experimental results for both single excitation (CP) and dual excitation (LP). Multiband behaviour is attained as a consequence of the periodicity of the phase shift between elements and the broad impedance bandwidth of the elements, which assures low reflection level when the condition of CP is fulfilled. Thus, very good matching has been obtained over the different bands with CP (around 6, 9 and 12 GHz). Therefore, the advantage of the use of the strip-slot element compared to a resonant element like a patch is that the operating frequency does not have to coincide with the resonance frequency of the element, which allows design flexibility, and multiband behaviour can be obtained. The phase of the element and the length of the transmission line sections allow certain flexibility to set the operating bands. Measurements of the radiation patterns for both CP and LP show that the antenna radiates broadside with low directivity and into both half-spaces, like the strip-slot element does. Moreover, low cross-polarisation levels are obtained around the broadside and radiation efficiency of more than 80% is achieved.

For single excitation (CP), axial ratios below 3 dB are achieved for the three operating bands, which indicate good polarisation purity.

The combination of the multiband behaviour and the two-port structure leads to very appealing applications. Since consecutive operating bands possess different signs of CP when excited at a single port, two bands with the same sign of CP can be diplexed through the two ports. This concept has been applied to build a self-diplexing antenna for GNSS.

A limitation of this antenna is the reception of the crosspolar component through the other antenna side. In the GNSS antenna, the multipath effect might be a handicap. Again, a solution would be placing a reflector plane at the proper distance from the antenna, with the undesired size increase.

Chapter 6: Conclusions and Outlook

This final chapter summarizes the research work developed in this thesis and stresses the most remarkable contributions. Lastly, it points out different perspectives of future work to carry on with this research.

6.1 SUMMARY AND CONCLUSIONS

A planar radiating structure based on the microstrip-slotline coupling has been studied in this Ph.D. thesis. It consists of a microstrip-fed slot with a symmetrically-arranged strip conductor superimposed on it. The achieved ultra broad impedance bandwidth (up to 16:1) lies in the resulting all-pass section that the strip and the slot make up. A theoretical study of the structure in terms of even and odd modes as well as a straightforward equivalent circuit based on a lattice network have been provided, which offer the required analytical tools to state the design methodology. Experimental and simulated results have confirmed that the strip acts as a mere matching element that does not alter the slot radiation characteristics practically.

Due to the series feeding of the element through the microstrip line, it is excellent for building planar series-fed arrays. Three array concepts have been thoroughly analysed and manufactured in order to prove that the availability of a broadly matched planar radiator can provide planar antennas with greater functionalities (e.g., multi-band behavior) than those obtained with classic resonant elements.

The first array concept to be studied has been a linear travelling-wave array built by loading the microstrip line with several equal strip-slot elements. Frequency scanning from backward to forward directions, according to the Floquet's theory, has been

achieved over different bands. The multiband behaviour is a consequence of the periodicity of the phase factor, but it is possible thanks to the broadband matching of the element. The low deterioration of the radiation efficiency and reflection coefficient in broadside has been improved by slightly misaligning the slots with respect to the strips. In order to be able to control the beam steering, this array concept has been extended to include varactor-based loaded-line phase shifters between the elements. Unlike previous works in the literature, the proposal achieves both electronic steering with a wide angle range and fixed beam over the design bandwidth, possible thanks to the non-resonant element on which the array is based. In addition, the circuitry can be added on the microstrip layer without modifying the antenna itself.

Another proposed antenna application for the complementary strip-slot element has been a log-periodic array. The slots follow the log-periodic progression while the strips are designed to guarantee impedance matching for each element. Since the basic element is not resonant, the design approach differs from the long-established design methodology of dipole log-periodic arrays. There is no need to add a phase shift of 180° between adjacent elements for achieving destructive interference in the reflections, as other log-periodic arrays need to do. Moreover, low scale factor (τ) with high radiation efficiency is possible, since the element radiation efficiency is not resonant, but high-pass, and size reduction can then be achieved. A prototype with a low τ (0.909) has proved the concept.

Finally, a ring array implementing the sequential rotation technique has been proposed for providing polarisation agility and multiband behavior with a very simple structure. The series feeding configuration allows the implementation of the required phase shifts between elements with just a microstrip line and the termination in two ports. Then, the polarisation can be configured (circular or linear and the sign) by controlling the excitations. In addition, since consecutive operating bands have different CP signs when single feeding, two bands with the same CP sign can be diplexed through the two ports. This latter feature has been used to design an antenna for GNSS capable of receiving two satellite navigation bands and diplexing them through the two ports without the need for any additional passive or active components.

Since the element has been completely characterised and antennas with appealing features have been designed, manufactured and measured, it can be said that the work has met all the initial objectives: this thesis has established a new perspective for planar antennas based on non-resonant elements. Although the structure was initially conceived as unit-cell for artificial transmission lines, its relevant applications have

been found in the field of antennas. However, it can be affirmed that metamaterials have once again served as an inspiration for finding novel structures.

6.2 ORIGINAL CONTRIBUTIONS

The main contribution of this thesis is the proposal of the complementary strip-slot as a microstrip-fed slot with ultra-broad impedance matching and the theoretical analysis to explain its behaviour and establish a design methodology. The proposed equivalent circuit deserves special mention, since it provides an excellent physical insight into the structure behaviour.

The work related to lattice networks is also noteworthy. A relevant property concerning power dissipation in this circuit topology has been extracted and has allowed the explanation of why the strip does not alter the radiation properties of the slot. Moreover, this circuit network has been more generally proposed for modelling symmetric TL discontinuities and components, with the advantage of the physical realizability of its components, which is not guaranteed when using T - or Π - networks.

In relation to the antenna applications of the complementary strip-slot, it must be said that, although the array topologies are classic, the resulting structures are innovative, since they are based on a novel broadly matched planar radiator, unlike the conventional planar arrays, based on resonant patches and/or slots. In the linear travelling-wave array, frequency scanning from backward to forward (including broad-side) over two bands is achieved. Moreover, when phase shifters are included in the array, the versatility of steering or maintaining the beam over a wide frequency band can be carried out without the need to modify the geometry of the radiating element thanks to the wide impedance bandwidth of the strip-slot. This is an important contribution to the state-of-the-art proposals. In the log-periodic array, the rethinking of the classic design methodology for wideband elements can be considered a significant contribution of this work and indicates that a size reduction (or broader bandwidths) is possible when using non-resonant elements. Finally, the combination of the series-fed two-port circular antenna with the wideband element in the sequentially rotated array allows both multiband behaviour and polarisation versatility without the need for additional passive or active components. As an example of application, a novel self-diplexing dual-band antenna for GNSS has been manufactured.

6.3 FUTURE WORK

Some brief ideas and guidelines are presented below as future work that can carry on from this dissertation:

- **Reduce/avoid back radiation**

Since back radiation is an inconvenience in the majority of antenna applications, it is important to ensure that the strip-slot radiates only into one half-space without losing radiation efficiency. Throughout the thesis, this problem has been solved with a reflector plane, properly located at the required distance. This is a possible solution; however, it increases the size of the element, which was a merit of the structure, and is frequency dependent. The idea to improve this matter in the future would be to incorporate a metallic layer close above the stub with such a geometry that it shields the microstrip line while avoiding the excitation of other modes over the broad bandwidth of the element. This is not a straightforward task, not only because the elimination of these generated undesired modes is not evident but also because attention must be paid to not modifying the slot and strip modes.

- **Arbitrarily-shaped strip-slot**

In this work, rectangular strips and slots have been used, as it was the simplest geometry to analyse the behaviour of the structure. However, its appealing properties are not unique to this geometry. The structure could adopt an arbitrary shape whenever the resulting even and odd modes fulfill the condition for good matching. This has been proven with dumbbell-shaped elements, but it could be extended to any other geometries, thus providing extra degrees of freedom in the design.

- **Modelling of the radiation losses**

The equivalent circuit based on a lattice network has proven to be a good tool for the analysis. The negligibility of the losses has resulted appropriate for establishing the design methodology for good matching. However, in the theoretical study of arrays, it is essential to consider the radiation losses. So far, they have been included in the equivalent circuit as an experimentally determined resistance in the series branch of the lattice. However, future work can be done to find a theoretical model.

- **Coupling between elements**

In the proposed arrays, the coupling effects can be considered negligible and the design of the arrays has been possible with the model of the isolated element. However, if for some applications the spacing between elements must be significantly reduced, it would be necessary to take into account this coupling. Therefore, proposed work for the future could be to include the mutual coupling in the element equivalent circuit.

- **Equivalent circuit for the misaligned strip-slot**

The misalignment between the strip and the slot introduces modifications in the element frequency response that have been used to avoid the worsening of the radiation properties at broadside in the uniform travelling-wave arrays. In order to have the proper design tools, the search for an equivalent circuit for the misaligned strip-slot can be an interesting line of research.

- **Lattice networks for the modelling of other structures**

Although some work has been carried out in the modelling of other structures with lattice networks, this topic of research has much more potential. For instance, the independence dissipation property that has been extracted for these topologies can be used to identify the origin of the losses in other structures, as has been done for the strip-slot.

- **Implementation of other array topologies**

Three array concepts have been carefully analysed in this work. However, research can be carried on by analysing other array topologies. Any series-fed array configuration built with planar resonators could be explored by replacing the radiator by the complementary strip-slot.

Appendix A: Artificial Transmission Lines Based on the Strip-Slot

The practical implementation of the CRLH TL consists of the repetition, an appropriate number of times, of series capacitors and shunt inductors loading a conventional TL [4]. After the introduction of the CRLH TL, artificial TLs with different topologies were proposed, like the ‘dual’ [70] or the ‘extended’ [71] CRLH. Even a derivation of artificial TLs of arbitrary order was presented in [72]. Thus, a specific dispersion diagram can be synthesized by simply cascading the necessary unit-cells.

As has been mentioned in Section 1.2, the artificial TLs based on ladder, T – or Π – networks have the disadvantage of the appearance of unavoidable stop-bands at the poles of the phase factor. Bongard *et al.* proved that these mismatching bands could be reduced by using a unit-cell based on a lattice network [6, 7]. Since the complementary strip-slot naturally behaves as a lattice network (see Chapter 2), this appendix analyses the feasibility of building artificial TLs with the proposed element and highlights the advantages of its use by means of a comparison between artificial TLs based on alternate stubs and slots (ladder version) and those built with the superimposed strip-slot (lattice version).

In both analysed structures, the slot and the stub provide the required series and shunt immittances, respectively, for building an artificial TL with LH behaviour. Fig. A.1a shows the layout of the unit-cell with alternate rectangular microstrip-fed stub and slot. Its lattice counterpart is detailed in Fig. A.1b, which is similar to the previous one, but with the superposition of the stub and slot.

For low coupling in the superimposed structure, it can be assumed that the immittances of the resultant networks in both cases of Fig. A.1 are provided by the same elements (the slot provides the series immittance and the stub, the parallel/cross one). Therefore, the design methodology for balanced condition (no gap between the LH

band and the RH band) would be the same: the immittances in each branch must present exactly the same singular frequencies (poles and zeros).

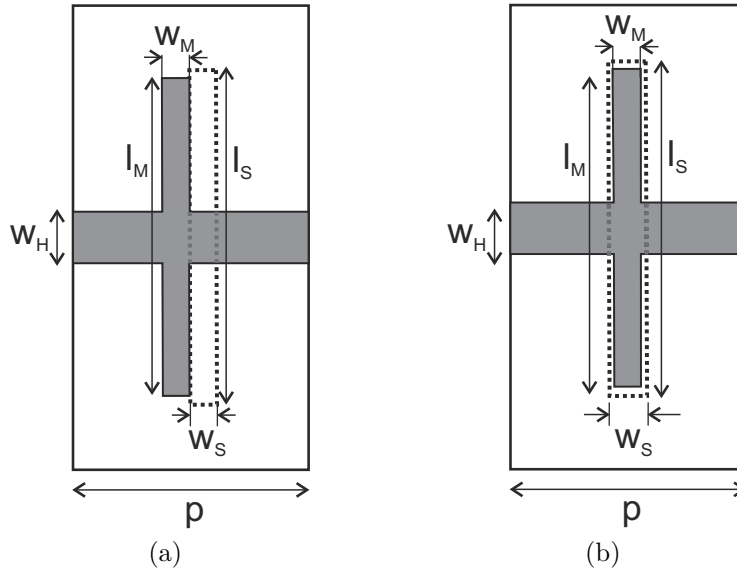


Figure A.1: Geometry of the unit-cells under comparison, where w_M , l_M , w_S and l_S stand for the widths and lengths of the stub and slot respectively, p is the cell size and w_H the width of the host TL. (a) corresponds to the unit-cell with alternate elements and (b) to the complementary strip-slot.

Since the conditions for balance behaviour of both structures of Fig. A.1 are the same, a common design of the stub and slot has been analysed with electromagnetic full-wave simulation. The chosen substrate was ARLON 1000 substrate with $\epsilon_r=10$ (high for reducing radiation) and $h=50$ mil. The resulting geometric parameters of the element were $w_S = w_M = 0.3$ mm, $l_S = 30$ mm, $l_M = 27.25$ mm and $w_H = 1.95$ mm (the characteristic impedance of the host TL is 39Ω).

Fig. A.2 and A.3 show a comparison of the S-parameters and the phase factor, respectively, between both unit-cells for a cell-size $p=10$ mm ($\approx \lambda/5$ at the first resonance frequency of the stub/slot). It can be observed that the superimposed structure does not have any stop-bands at the poles of the phase factor, achieving a good matching over the whole band. The phase factor remains practically the same in both cases, with alternate RH and LH bands. The first resonance frequency of the stub/slot was set to 2.4 GHz, which corresponds to the first pole of the phase factor. It must be clarified that the phase factor also includes the phase introduced by the accessing microstrip sections. For this reason, the poles in the phase factor are shifted downwards in frequency with respect to the resonances of the strip-slot.

Finally, Fig. A.4 shows a comparison of the resulting S-parameters of a three-cell

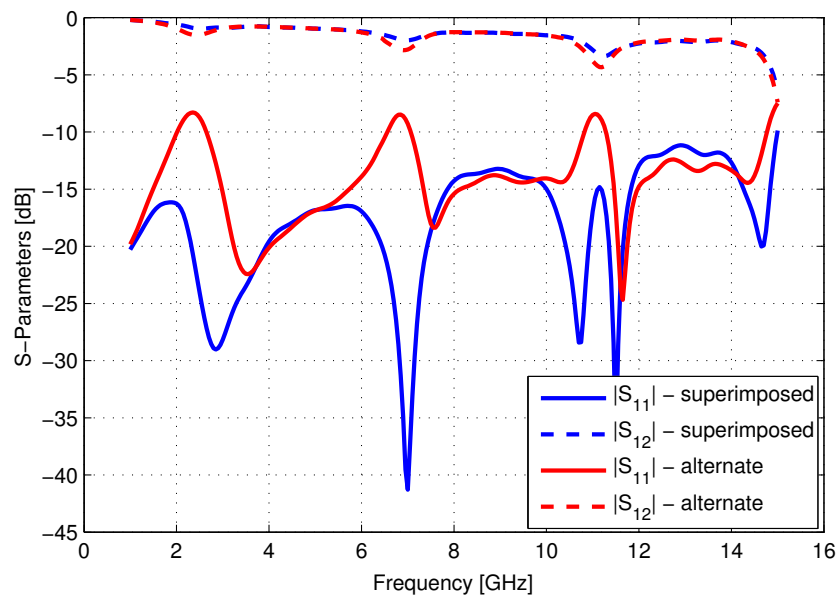


Figure A.2: S-Parameters comparison between the alternate and superimposed strip-slot unit-cells.

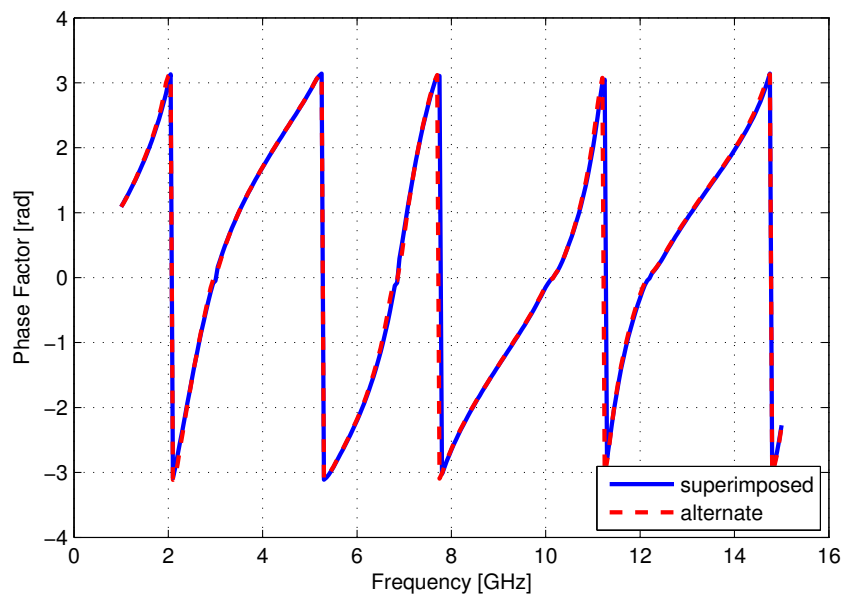


Figure A.3: Phase factor comparison between the alternate and superimposed strip-slot unit-cells.

structure with both ladder-based and lattice-based unit-cells. A significant improvement is achieved through the superposition of both the stub and the slot instead of using its alternate counterpart. It can be observed that stop-bands that are unavoidable in ladder, T- or II-topologies can now be suppressed. As well as its all-pass behaviour, other advantages of the proposed unit-cell are its easy manufacture, single layer and the no need for via-holes or air bridges.

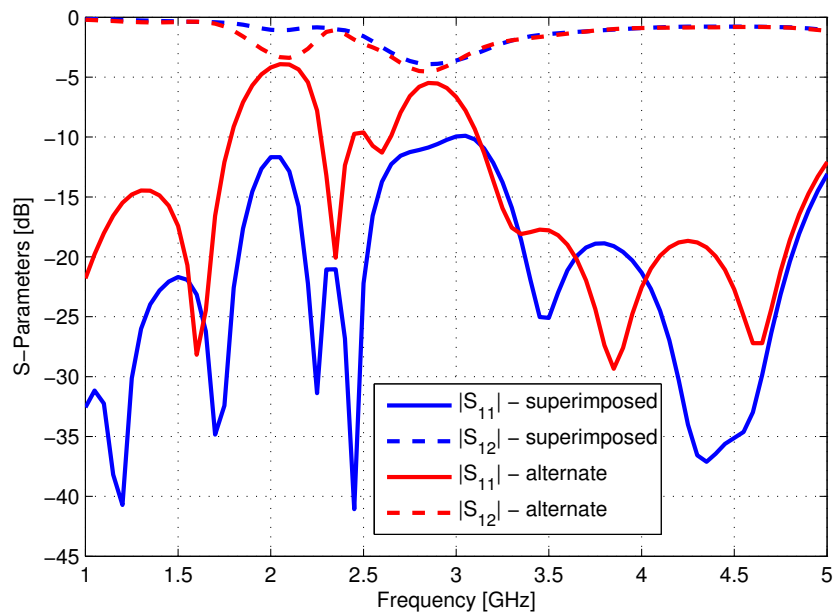


Figure A.4: S-Parameters comparison between a three-cells structure built with the alternate and the superimposed strip-slot unit-cells.

Appendix B: Lattice Networks

B.1 BASIC PROPERTIES

Lattice networks have been studied for many years and have long been used in communications circuits. A symmetrical lattice topology consists of two series-branch impedances, named Z_a , and two cross-branch impedances, called Z_b , according to Fig. B.1. Its basic properties can be found in classic books as in [18, 73]; however, for the sake of comprehension, a summary is provided here.

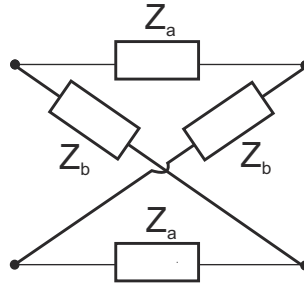


Figure B.1: General symmetrical lattice network.

The impedance matrix of a symmetrical lattice is given by

$$[Z] = \begin{bmatrix} \frac{Z_b + Z_a}{2} & \frac{Z_b - Z_a}{2} \\ \frac{Z_b - Z_a}{2} & \frac{Z_b + Z_a}{2} \end{bmatrix}. \quad (\text{B.1})$$

Therefore, the lattice impedances can be obtained from the impedance/admittance parameters as follows:

$$Z_a = Z_{11} - Z_{12} \quad (\text{B.2a})$$

$$Y_b = Y_{11} + Y_{12}, \quad (\text{B.2b})$$

and the resulting image impedance is given by [18]

$$Z_{im} = \sqrt{Z_a Z_b}. \quad (\text{B.3})$$

Consequently, under the balanced condition $Z_a Z_b = Z_0^2$ (complementary branch impedances), a lattice network can be an example of an all-pass equalizer. That is, it presents constant impedance behaviour and the relative phase between the input and the output varies with frequency, if the branches impedances do so, since the image propagation function of the lattice network is given by

$$\gamma = \cosh^{-1} \left(\frac{Z_b + Z_a}{Z_b - Z_a} \right). \quad (\text{B.4})$$

B.2 POWER DISSIPATION

If a symmetrical lattice network is considered (one with equal series arms and equal cross arms), the power dissipated in each branch of the network can be calculated by solving the circuit shown in Fig. B.2a. In order to perform the nodal analysis, it is customary to reorganize the lattice topology in the bridge form shown in Fig. B.2b.

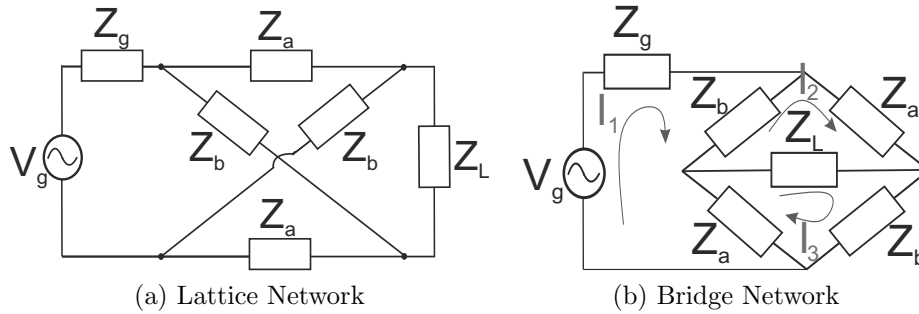


Figure B.2: Terminated symmetrical lattice network.

Therefore, the loop currents in Fig. B.2b can be calculated by solving the following equation system:

$$\begin{pmatrix} Z_{\Sigma_g} & -Z_b & -Z_a \\ -Z_b & Z_{\Sigma_L} & -Z_L \\ -Z_a & -Z_L & Z_{\Sigma_L} \end{pmatrix} \begin{pmatrix} I_1 \\ I_2 \\ I_3 \end{pmatrix} = \begin{pmatrix} V_g \\ 0 \\ 0 \end{pmatrix} \quad (\text{B.5})$$

where $Z_{\Sigma_g} = Z_g + Z_a + Z_b$ and $Z_{\Sigma_L} = Z_L + Z_a + Z_b$.

Then, the dissipated power in each branch of the lattice network can be obtained

from

$$P_a = \frac{1}{2}|I_2|^2 \operatorname{Re}[Z_a] \quad (\text{B.6a})$$

$$P_b = \frac{1}{2}|I_3|^2 \operatorname{Re}[Z_b]. \quad (\text{B.6b})$$

When $Z_L = Z_g = Z_0$, it can be derived that

$$I_2 = \frac{V_g}{2(Z_a + Z_0)} \quad (\text{B.7a})$$

$$I_3 = \frac{V_g}{2(Z_b + Z_0)} \quad (\text{B.7b})$$

and, consequently,

$$P_a = |V_g|^2 \frac{\operatorname{Re}[Z_a]}{8|Z_a + Z_0|^2} \quad (\text{B.8a})$$

$$P_b = |V_g|^2 \frac{\operatorname{Re}[Z_b]}{8|Z_b + Z_0|^2}, \quad (\text{B.8b})$$

which proves that, in a symmetrical lattice network with $Z_g = Z_L$, the currents and the dissipated power in the series branch only depends on the impedance value of the series branch and are independent of the cross branch, and viceversa.

This result is expected if the Barlett's bisection theorem is borne in mind [74]. Summarizing, it states that any two-port network with a plane of symmetry can be represented by a lattice network whose series branch impedance Z_a is the impedance obtained for the even-mode excitation (the same excitation voltage in both ports) and whose crossed branch impedance Z_b is the the impedance obtained for the odd-mode excitation (the same magnitude of excitation voltage in both ports but the opposite sign). Since both impedances Z_a and Z_b correspond to orthogonal modes of excitation, it is evident that the currents and voltages, and then the dissipated power along each branch of the lattice, are independent on the other branch. If this is applied to symmetrical electromagnetic structures, it means that the power dissipation in the total structure can be calculated as the sum of the power dissipated in the resulting impedances under even and odd excitations, since both are independent. Moreover, if the even and odd resulting impedances are identified with a part of the physical structure, the origin of the losses can be determined.

To the author's knowledge, this unique property of symmetrical lattice networks has never been stated in the literature nor applied to electromagnetic structures. How-

ever, it can be very interesting when applied to symmetrical structures modelled by lattice networks, like the complementary strip-slot element. In fact, this is an additional advantage in the modelling of symmetrical transmission line components and discontinuities using this topology with respect to those presented in Appendix C.

Appendix C: Advantages of the Modelling With Lattice Networks

This appendix deals with the advantages of lattice networks with respect to T- and Π -topologies for modelling symmetric TL discontinuities and components. The lattice network presents some important features, which make it a powerful tool for finding physically-realizable equivalent circuits. The limitations of the T- and Π -topologies and the validity of the lattice network in terms of realizability are highlighted here through two microstrip components: a dumbbell-shaped defected ground structure and a microstrip stepped-impedance hairpin resonator. Moreover, the lattice image impedance is proposed as a parameter that allows the determination of whether a branch of the network is predominant.

C.1 INTRODUCTION

TL components and discontinuities are mostly modelled using T- or Π -topologies. Three parameters are necessary to model a network with four terminals completely. However, many TL components and discontinuities present symmetry along an axis perpendicular to the axis of the TL. In this case, only two independent parameters are required for the network specification and the symmetric lattice topology arises as a convenient alternative.

Designers use the T- and Π -topologies as a tool in order to find appropriate equivalent circuits. For instance, when a Defected Ground Structure (DGS) is modelled, the equivalent T- or Π -network reveals that it behaves as a series immittance (if the reference planes are properly chosen), since the effect of the parallel branch is negligible. However, if we carefully analyse the resultant impedances of the equivalent T-section, some irregular behaviour can be observed: the real part of the parallel impedance

can present negative values, which physically make no sense. These anomalies might appear in the real parts of the parallel branch of the T-section as well as the series branch of the Π -topology. These effects are often attributed to simulation, measurement or numerical errors. However, its origin is more relevant: the equivalent T- and Π -sections do not guarantee the physical realizability of their branches. This problem can be overcome with the use of a lattice network, since the lattice equivalent of any two-port network is always physically realizable. That means that it is unnecessary to use negative lumped elements (inductances, capacitances or resistances) to build the equivalent circuit. This advantage has already been exploited for modelling lossy dielectric posts in a rectangular waveguide [75, 76] and, more recently, for coupled-line sections [17]. However, its use is still not very widespread.

The basic properties of lattice networks are summarised in Appendix B; however, it is important to mention here that the lattice impedances can be obtained from the impedance/admittance parameters as follows:

$$Z_a = Z_{11} - Z_{12} = Z_{1,T} \quad (\text{C.1a})$$

$$Y_b = Y_{11} + Y_{12} = Y_{2,\Pi}, \quad (\text{C.1b})$$

where $Z_{1,T}$ and $Y_{2,\Pi}$ are properly defined in Fig. C.1. Therefore, the lattice topology can be interpreted as a combination of both the T- and Π -sections.

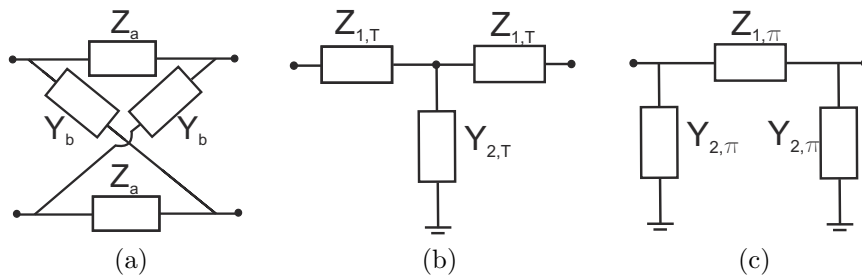


Figure C.1: Network topologies: (a) Lattice section, (b) T-section and (c) Π -section.

C.2 REALIZABILITY EVALUATION

In order to illustrate the limitations of the T- and Π -sections and stress the advantages of the lattice network in practice, two TL components are evaluated in this section. The following procedure consists of the comparison of the equivalent impedances in T- and Π -networks with those of the lattice section, specifically those different from the

lattice immittances: $Z_{1,\Pi}$ and $Y_{2,T}$. This is carried out through the conversion of the electromagnetic full-wave simulated S-parameters (using HFSS) to the impedances of the corresponding networks. The reference planes for the S-parameters are defined in each layout figure as T_1 and T_2 and both dissipative and radiation losses are considered. The first analysed component is a dumbbell DGS, which is an example of a circuit where one of the impedance branches can be considered negligible. As an example of a circuit in which the two branches are significant, we evaluate a microstrip hairpin resonator.

C.2.1 Dumbbell-Shaped DGS

The layout of the dumbbell DGS is shown in Fig. C.2. In order to evaluate a real design, we have picked the substrate and geometrical parameters from [77] ($w=5$ mm, $w_L=3.5$ mm and $g=0.2$ mm on Duroid 5880, with $\epsilon_r=2.2$ and $h=20$ mil).

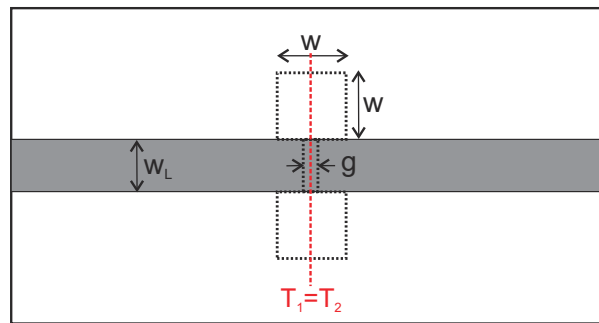


Figure C.2: Layout of the dumbbell-shaped DGS.

A DGS essentially presents a series impedance and therefore, the effect of the parallel branch of the T-, Π - or lattice topology is negligible. However, for the T-topology, some anomalies are found in the real part of $Y_{2,T}$. Although, as already mentioned, its effect is negligible, this fact highlights a limitation in the use of this kind of section. Fig. C.3 shows a comparison of the real part of the resulting parallel and cross branches for the T and lattice equivalent sections, respectively. It can be appreciated that both behave in a similar way up to 5 GHz, approximately. Then, there is a band in which the impedance of the T-topology takes negative values, which corresponds to the resonance frequency band of the DGS. Above this anomaly, it recovers the lattice behaviour. The Π -topology will not present this anomaly, since the parallel admittance is equal to the cross branch of the lattice, according to (C.1b). In this case, it is the series impedance which might lead to negative values in the real part. However, for this example, no anomalies have been found in the Π -section.

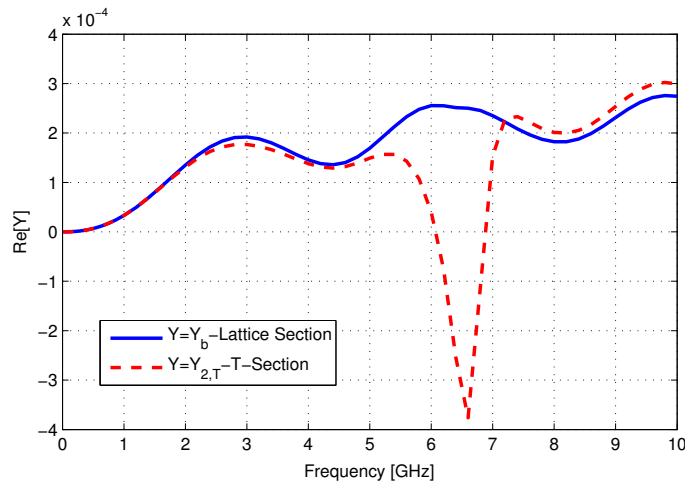


Figure C.3: Real part of the parallel admittance of the T- and lattice topologies for the dumbbell DGS.

C.2.2 Microstrip Stepped-Impedance Hairpin Resonator

The layout of the hairpin resonator is shown in Fig. C.4. The dimensions are based on a real design made in [78] on Duroid 6010, with $\epsilon_r=10.2$, $h=25$ mil, $w_L=0.56$ mm, $w_1=1.31$ mm, $w_2=0.3$ mm, $g=0.2$ mm, $l_1=4.5$ mm, $l_2=2.22$ mm and $l_3=4.85$ mm. It consists of a single transmission line and a pair of coupled-lines, both fed by a microstrip line.

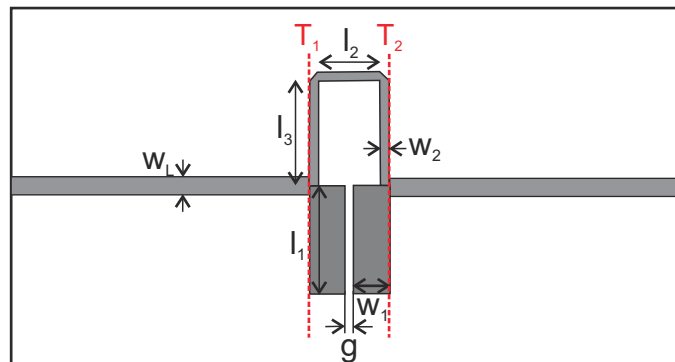


Figure C.4: Layout of the microstrip stepped-impedance hairpin resonator.

As pointed out in [78], the equivalent circuit of the hairpin resonator has series and parallel contributions. Fig. C.5 makes a comparison between the equivalent series impedance in a Π -topology and the series branch of the equivalent lattice. It is observed, that $Z_{1,\Pi}$ takes negative values in its resistive part and its imaginary part does not monotonically increase with frequency in some bands where the real part is negligible

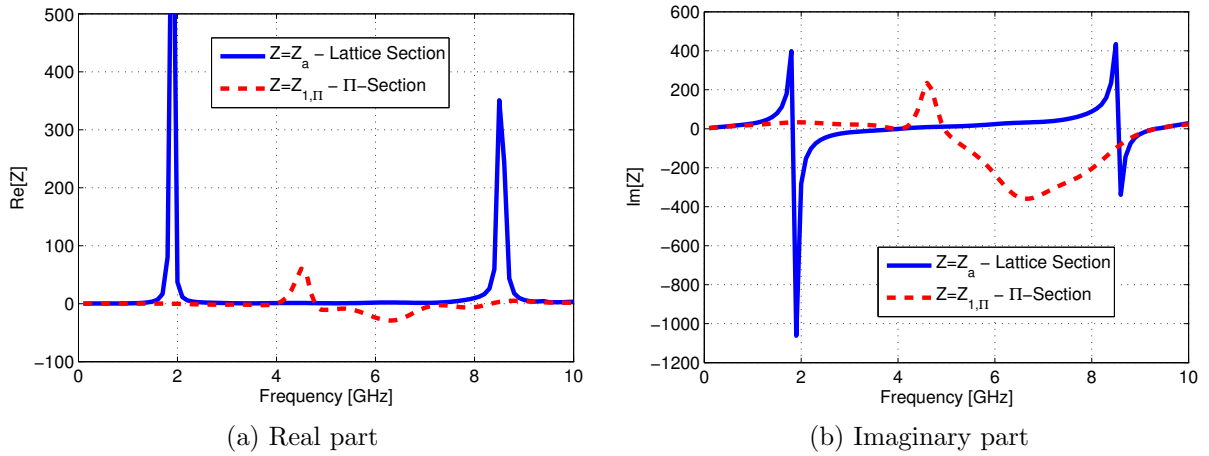


Figure C.5: Series impedance of the Π - and lattice topologies for the hairpin resonator.

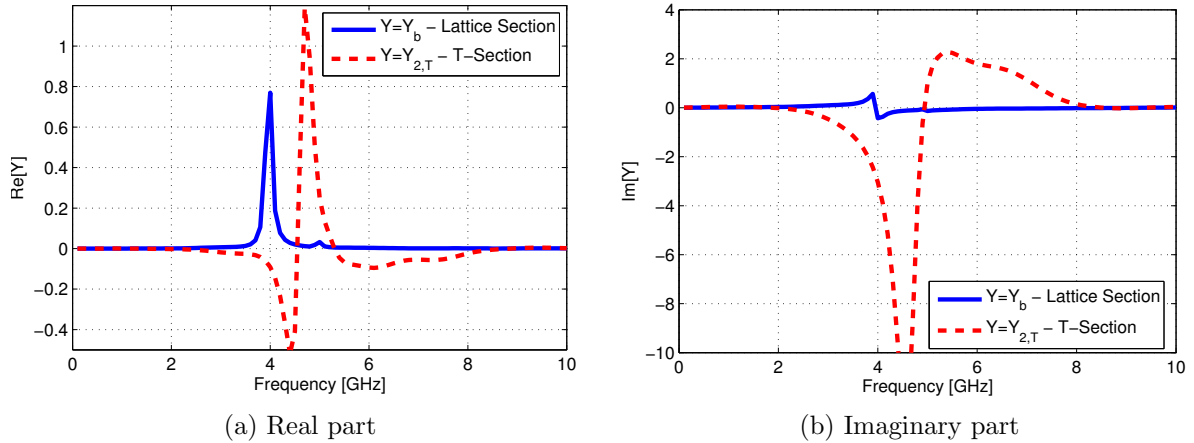


Figure C.6: Parallel admittances of the T- and lattice topologies for the hairpin resonator.

(e.g., 5-6 GHz), which is inconsistent with Foster's reactance theorem. This limitation is overcome with a lattice section. Likewise, the realizability of the resulting T-section has been analysed. Thus, Fig. C.6 demonstrates that the same limitations appear in the parallel admittance if a T-section is used.

C.3 USE OF THE IMAGE IMPEDANCE

The image impedance of a lattice network, defined in (B.3), can give a hint as to which branch (series or cross) would play a more significant role in the circuit description. When the component is a series element, Y_b will theoretically be 0, and as a result $|Z_{im}| \rightarrow \infty$. Likewise, when the element is parallel, Z_a should be close to 0 and then $|Z_{im}| \rightarrow 0$. In order to illustrate the usefulness of this parameter, Fig. C.7

shows the magnitude of the resulting image impedances for the dumbbell DGS and the hairpin resonator. Different axes have been used for a better representation. As expected, the magnitude of the image impedance is particularly high for the DGS over the whole band, thus indicating that it essentially corresponds to a series element. On the other hand, in the case of the hairpin resonator, the image impedance has a variable behaviour, which means that the importance of the two branches depends on frequency. Thus, we can identify the frequencies at which the series contribution is predominant (high value of $|Z_{im}|$), which occurs at 2 and 8.5 GHz, approximately, and those at which the element behaves as a parallel element, which is at 4 GHz. These conclusions agree with Figs. C.5 and C.6.

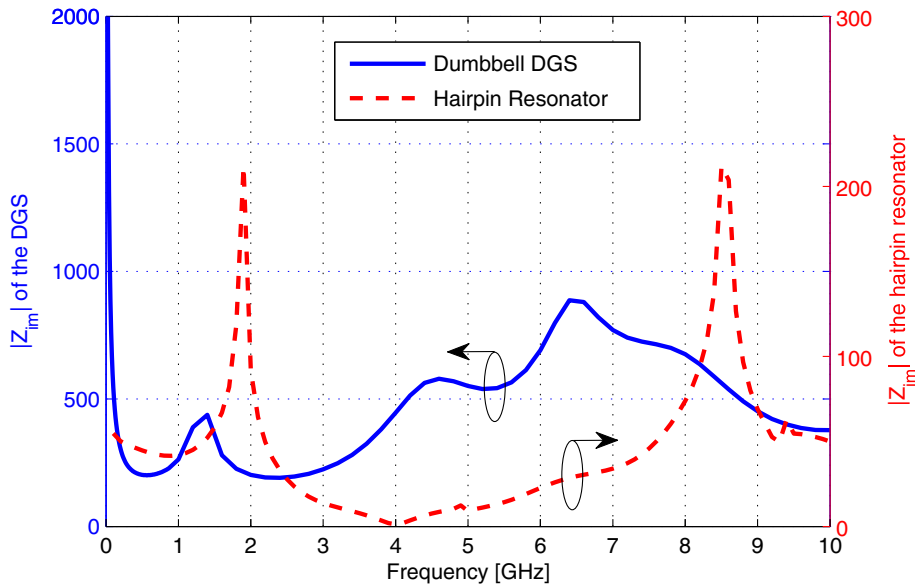


Figure C.7: Magnitude of the lattice image impedance for the dumbbell DGS and the hairpin resonator.

C.4 CONCLUSIONS

Lattice networks have been proposed for modelling symmetric TL components and discontinuities and have been compared to the widely-favoured T- and Π -sections in terms of realizability. In order to show the practical limitations of T- and Π -sections, two examples have been analysed: a dumbbell DGS and a microstrip stepped-impedance hairpin resonator. The results have highlighted that, for the DGS, which is essentially a series element, the series branch does not present realizability problems in any of the three topologies (T, Π and lattice), although anomalies have been detected for the parallel impedance in the case of the T-topology. Therefore, in this case, a good choice

of the topology, T or Π , might avoid negative resistances in the equivalent impedances. This is not necessary if the lattice network is used, since realizability is always guaranteed. For the hairpin resonator, which has both series and parallel contributions, not even a good choice of the topology, T or Π , can avoid the realizability problems and only the lattice section leads to wide-band realizable equivalent circuits. Finally, an easy recognition of the bands where the component behaves as a series or parallel element has been carried out for the two analysed examples by using the lattice image impedance.

Appendix D: Floquet's Theorem and Spatial Harmonic Expansion

Floquet's theorem describes the form of guided waves travelling along an axially periodic structure. With the axial direction denoted by z and the period by p , Floquet's theorem may be stated as follows [79]. A time harmonic electromagnetic field $\psi(x, y, z)$ of a normal mode guided along an axially periodic structure possesses the property

$$\psi(x, y, z + p) = e^{ik_{z0}p}\psi(x, y, z), \quad (\text{D.1})$$

where the Floquet wave number $k_{z0} = \beta_0 + i\alpha$ stands for the fundamental propagation constant, while β_0 and α represent the corresponding phase and attenuation constants, respectively.

If we consider

$$\psi(x, y, z) = e^{ik_{z0}z}P(x, y, z) \quad (\text{D.2})$$

it can be concluded from (D.1) that P is a periodic vector function of z with the period p , that is,

$$P(x, y, z + p) = P(x, y, z). \quad (\text{D.3})$$

The form (D.2), together with (D.3), is often referred to as Bloch wave, and a single period of width p is sometimes called a unit-cell.

According to Floquet's theorem, the cross-sectional complex field distribution of a periodic structure remains unchanged under an axial translation of the observation point through a period p , while the mode amplitude multiplies itself by a complex constant $e^{ik_{z0}p}$. Therefore, from the knowledge of the field distribution within a single period, the guided-wave field at any point on an infinite periodic structure can be determined.

The periodic vector function $P(x, y, z)$ may be expanded in a Fourier series

$$P(x, y, z) = \sum_{m=-\infty}^{\infty} a_m(x, y) e^{i(2\pi/p)mz} \quad (\text{D.4})$$

which when substituted into D.2 results in

$$\psi(x, y, z) = \sum_{m=-\infty}^{\infty} a_m(x, y) e^{ik_m z} \quad (\text{D.5})$$

where

$$k_{zm} = k_{z0} + \frac{2\pi}{p}m \quad m = 0, \pm 1, \pm 2, \dots \quad (\text{D.6a})$$

$$k_{zm} = \beta_m + i\alpha = \beta_0 + \frac{2\pi}{p}m + i\alpha. \quad (\text{D.6b})$$

The Fourier series expansion (D.5) highlights that the field of a normal mode of an axially periodic structure can be expressed in terms of an infinite number of travelling waves of the form $a_m(x, y)e^{ik_{zm}z}$, called *spatial harmonics*, where the wave numbers k_{zm} are the spatial harmonic propagation constants and $a_m(x, y)$, the spatial harmonic amplitudes. Thus, the periodic structure will be able to radiate whenever any of its spatial harmonics is within the fast wave region.

Appendix E: Publications Derived From This Thesis

JOURNALS

- [1] E. Abdo-Sánchez, D. Palacios-Campos, C. Frías-Heras, F.Y. Ng-Molina, T.M. Martín-Guerrero, and C. Camacho-Peñalosa “Electronically Steerable and Fixed-Beam Frequency-Tunable Planar Traveling-Wave Array,” submitted for publication.
- [2] E. Abdo-Sánchez, T.M. Martín-Guerrero, J. Esteban, and C. Camacho-Peñalosa, “On the Radiation Properties of the Complementary Strip-Slot Element,” accepted for publication in the *IEEE Antennas and Wireless Propagation Letters*.
- [3] E. Abdo-Sánchez, C. Camacho-Peñalosa, J. Esteban, and T.M. Martín-Guerrero, “Planar multiband sequentially-rotated array with polarisation agility based on the complementary strip-slot element,” accepted for publication in the *Journal of Electromagnetic Waves and Applications*.
- [4] E. Abdo-Sánchez, J. Esteban, T.M. Martín-Guerrero, C. Camacho-Peñalosa, and P.S. Hall, “A novel planar log-periodic array based on the wideband complementary strip-slot element,” *IEEE Transactions on Antennas and Propagation*, vol. 62, no. 11, pp. 5572–5580, Nov. 2014.
- [5] E. Abdo-Sánchez, T.M. Martín-Guerrero, J.E. Page, J. Esteban, and C. Camacho-Peñalosa, “On the feasibility of the complementary strip-slot element to build planar series-fed arrays,” *International Journal of Microwave and Optical Technology*, vol. 9, no. 1, pp. 24–28, Jan. 2014.

- [6] E. Abdo-Sánchez, J. Esteban, T.M. Martín-Guerrero, J.E. Page, and C. Camacho-Peñalosa, “The use of lattice networks for modelling symmetric transmission line components and discontinuities,” *Microwave and Optical Technology Letters*, vol. 55, no. 3, pp. 636–639, Jan. 2013.
- [7] E. Abdo-Sánchez, J.E. Page, T.M. Martín-Guerrero, J. Esteban, and C. Camacho-Peñalosa, “Planar broadband slot radiating element based on microstrip-slot coupling for series-fed arrays,” *IEEE Transactions on Antennas and Propagation*, vol. 60, no. 12, pp. 6037–6042, Dec. 2012.
- [8] E. Abdo-Sánchez, T.M. Martín-Guerrero, and C. Camacho-Peñalosa, “Multiband slot- and stub-based dual composite right-/left-handed transmission line,” *Advanced Electromagnetics*, vol. 1, no. 3, Oct. 2012.

CONFERENCES

- [1] E. Abdo-Sánchez, T.M. Martín-Guerrero, J. Esteban, and C. Camacho-Peñalosa, “A Self-Diplexing Dual-Band Planar Array for GNSS Applications,” to be presented at the *IEEE Antennas and Propagation Symposium (AP-S)*, Vancouver, Jul. 2015.
- [2] E. Abdo-Sánchez, T.M. Martín-Guerrero, J. Esteban, and C. Camacho-Peñalosa, “On the Phase Response and Radiation Efficiency of the Complementary Strip-Slot as an Array Element,” to be presented at the *9th European Conference on Antennas and Propagation (EuCAP)*, Lisbon, Apr. 2015.
- [3] E. Abdo-Sánchez, J. Esteban, T.M. Martín-Guerrero, J.E. Page, and C. Camacho-Peñalosa, “The complementary strip-slot: From the unit-cell of artificial transmission lines to the basic element of novel antennas,” in *Proceedings of the XXIX Simposium Nacional de la Unión Científica de Radio (URSI 2014)*, Valencia, Sep. 2014. *Received the *URSI Young Researchers Award*.
- [4] E. Abdo-Sánchez, T.M. Martín-Guerrero, J.E. Page, J. Esteban, and C. Camacho-Peñalosa, “On the feasibility of the complementary strip-slot element to build planar series-fed arrays,” in *Proceedings of the 14th International Symposium on Microwave and Optical Technology (ISMOT-2013)*, Kuala Lumpur, Oct. 2013.
- [5] E. Abdo-Sánchez, C. Camacho-Peñalosa, T.M. Martín-Guerrero, J. Esteban, and

- J.E. Page, “Multiband circularly-polarized planar array based on the complementary strip-slot element,” in *Proceedings of the European Microwave Conference (EuMC)*, Nuremberg, Oct. 2013, pp. 652–655.
- [6] E. Abdo-Sánchez, T.M. Martín-Guerrero, J.E. Page, J. Esteban, and C. Camacho-Peñalosa, “Arrays planares basados en el elemento strip-slot complementario,” in *Proceedings of the XXVIII Simposium Nacional de la Unión Científica de Radio (URSI 2013)*, Santiago de Compostela, Sep. 2013.
- [7] E. Abdo-Sánchez, J.E. Page, T.M. Martín-Guerrero, J. Esteban, and C. Camacho-Peñalosa, “The complementary strip-slot as a broadband planar array element,” in *Proceedings of the Encuentro Ibérico de Electromagnetismo Computacional*, Denia, May 2013.
- [8] E. Abdo-Sánchez, J. Esteban, T.M. Martín-Guerrero, J.E. Page, and C. Camacho-Peñalosa, “Microstrip series-fed array based on the strip-slot element,” in *Proceedings of the 7th European Conference on Antennas and Propagation (EuCAP)*, Apr. Gothenburg, 2013, pp. 1447–1450.
- [9] E. Abdo-Sánchez, T. Martín-Guerrero, C. Camacho-Peñalosa, J. Page, and J. Esteban, “All-pass slot-based artificial transmission line unit-cell,” in *Proceedings of the 6th International Congress on Advanced Electromagnetic Materials in Microwaves and Optics (Metamaterials’2012)*, St. Petersburg, Sep. 2012.
- [10] E. Abdo-Sánchez, T.M. Martín-Guerrero, and C. Camacho-Peñalosa, “Multiband slot-based dual composite right/left-handed transmission line,” in *Proceedings of the 3rd Young International Conference on Metamaterials, Photonic Crystals and Plasmonics*, Paris, Apr. 2012.
- [11] E. Abdo-Sánchez, T.M. Martín-Guerrero, C. Camacho-Peñalosa, J.E. Page, and J. Esteban, “Bandwidth enhancement of microstrip-fed slot radiating element using its complementary stub,” in *Proceedings of the 5th European Conference on Antennas and Propagation (EuCAP)*, Rome, Apr. 2011, pp. 1125–1128.
- [12] E. Abdo-Sánchez, J. Fernández-Segovia, T.M. Martín-Guerrero, and C. Camacho-Peñalosa, “Triband dual CRLH transmission line using dumbbell-shaped DGS and stub,” in *4th Young Scientist Meeting on Metamaterials*, Valencia, Feb. 2011.

Appendix F: Summary in Spanish

F.1 INTRODUCCIÓN

F.1.1 Marco contextual

Es indudable que, en los últimos años, el mundo ha experimentado numerosos cambios que han alterado nuestra forma de vida y la manera en que los seres humanos nos comunicamos. En gran medida, estos avances son causa del rápido desarrollo de las nuevas tecnologías de comunicación, en especial de las denominadas “wireless”. A pesar de la acelerada evolución en este campo, siguen existiendo retos pendientes relativos a los nuevos servicios emergentes de banda ancha que requieren el esfuerzo de la comunidad científica.

Concretamente, el diseño de la antena en este tipo de sistemas de comunicaciones es uno de los desafíos al que se enfrentan los ingenieros de telecomunicación. Aunque pueda parecer un problema clásico, los servicios que han aparecido recientemente requieren nuevas funcionalidades, mayores anchos de banda, mejor eficiencia y directividad, así como bajo coste en la fabricación.

Las antenas planares han sido unas de las más usadas y estudiadas en las últimas décadas y unas de las mejores candidatas para los nuevos servicios de telecomunicación. Sus ventajas son claras: poco peso, bajo coste y perfil, compatibilidad con la circuitería integrada, pequeño tamaño y reducido coste de fabricación. Sin embargo, su éxito se ha visto limitado por el escaso ancho de banda que presentan. Debido a la naturaleza resonante de la ranura y el parche alimentados por microstrip, sus anchos de banda en impedancia son insuficientes para la mayoría de los servicios de comunicaciones actuales. La mejora de este parámetro ha sido objeto de numerosas investigaciones; sin embargo, este problema sigue sin estar resuelto definitivamente.

Las técnicas que más éxito han tenido para aumentar el ancho de banda de impedancia en los elementos radiantes en tecnología microstrip han sido el uso de redes de adaptación de impedancias y la introducción de múltiples resonancias [1, 2]. Ambos métodos presentan inconvenientes, ya que, o bien, se aumenta el área de la superficie, haciéndolo inapropiado como elemento de un array, o bien, se requieren estructuras multicapa, con el consiguiente aumento de coste, complejidad y tamaño. Por tanto, la mejora del ancho de banda de impedancia sin el incremento indeseado de estos factores resulta una línea importante de investigación en antenas planares.

Otra limitación de las antenas microstrip es la baja eficiencia de radiación comparada con otras antenas, que se supera combinando varios elementos para formar arrays. Una posibilidad para excitar el array es la alimentación en serie, que tiene las ventajas de simplicidad, menor espacio sobre el sustrato, pérdidas de atenuación más bajas y menor radiación espúrea, comparada con la alimentación corporativa. Además, si el array se configura como array de onda progresiva, una aplicación interesante es la posibilidad de apuntar el haz fuera de la dirección de broadside. De hecho, la aparición de las líneas de transmisión (LT) artificiales “diestra/zurda” (CRLH) [4], inspiradas en los metamateriales, encontró una aplicación importante en el diseño de antenas de onda progresiva y reavivó el interés en ellas. Una LT artificial es una estructura periódica, construida como la repetición espacial de una celda unitaria que sintetiza las características de dicha LT. El comportamiento distinto de las LTs CRLH con respecto a las convencionales permitió mejorar las funcionalidades de los circuitos y las antenas en el ámbito de las microondas.

El mayor reto en la construcción de una LT artificial consiste en encontrar una celda unitaria apropiada para las exigencias de la aplicación concreta. Por este motivo, un tema de investigación atractivo para la comunidad de antenas ha sido la búsqueda de celdas unitarias novedosas que permitan la implementación de antenas planares con funcionalidades mejoradas, teniendo en cuenta los requerimientos de los servicios emergentes (por ejemplo, gran ancho de banda).

F.1.2 Génesis

En la búsqueda de una celda unitaria para construir LT artificiales en tecnología planar, se hicieron distintos experimentos cargando periódicamente una línea microstrip con ranuras (slots) en el plano de masa alternadas con stubs terminados en abierto. Con

esta celda formada por una microstrip alimentando en serie a una ranura en el plano de masa y un stub en la capa de la microstrip, se obtuvo el esperado comportamiento diestro/zurdo en el factor de fase de la LT resultante con las bandas de rechazo usuales entre la frontera del comportamiento diestro con zurdo.

Buscando la distancia óptima entre la ranura y el stub, se descubrió que cuando se superponían completamente, el ancho de banda en impedancia resultante mejoraba sustancialmente con respecto a cuando la ranura y el stub se colocaban de forma alternada. Sorprendentemente, las bandas eliminadas desaparecían. Este inusual fenómeno no tuvo una explicación inmediata y ha dado paso a esta tesis doctoral.

Dado que las ranuras radiaban considerablemente, la idea de construir medios de transmisión con la estructura encontrada fue sustituida por su aplicación en el mundo de las antenas. Como resultado, esta tesis doctoral se centra en el análisis y las aplicaciones como elemento de array de esta estructura, a la que hemos denominado el *strip-slot complementario*, debido a que adaptación de banda ancha reside en la complementariedad entre el stub (strip) y la ranura (slot). Las ventajas de este elemento son destacadas: está implementado en tecnología microstrip, con un único sustrato y sin requerir el uso de vías, lo que implica bajos coste y complejidad de fabricación. Además, es una estructura radiante que supera la limitación de las antenas microstrip: su estrecho ancho de banda. Asimismo, su alimentación en serie y su factor de fase no lineal le hacen especialmente apropiado para la construcción de arrays de onda progresiva.

F.1.3 Objetivos

El primer objetivo de esta tesis fue el análisis pormenorizado de la estructura para proporcionar una explicación sólida, basada en la teoría electromagnética, sobre su comportamiento, así como encontrar un circuito equivalente para su sencillo modelado. Basándonos en la teoría desarrollada, se debía establecer una metodología de diseño para adaptación en banda ancha.

Una vez caracterizado completamente el elemento, la finalidad era explorar distintas configuraciones de arrays alimentados en serie y explotar las características especiales de este elemento para crear antenas con funcionalidades novedosas o mejoradas.

Un requisito autoimpuesto importante fue la verificación de las conclusiones extraídas de la teoría y las simulaciones electromagnéticas mediante la fabricación de

prototipos en cada fase de la investigación.

El objetivo final de este trabajo de investigación ha sido poner de manifiesto el potencial del elemento strip-slot complementario como un elemento radiante no resonante en tecnología microstrip y su capacidad para crear antenas innovadoras.

F.1.4 Estructura de los contenidos

El Capítulo 2 contiene el análisis completo del elemento strip-slot complementario: estudio electromagnético, propuesta del circuito equivalente y metodología de diseño. Además, se muestran resultados experimentales de dos prototipos y se estudia la influencia de los parámetros geométricos en el comportamiento de la estructura.

Una vez caracterizado el elemento, se exploran distintas configuraciones de arrays de onda progresiva. El Capítulo 3 contiene el estudio del primer, y más inmediato, concepto de array, que consiste en cargar la línea microstrip con varios elementos strip-slot idénticos. Con un sencillo prototipo, se analiza la capacidad de escaneo en frecuencia del array, utilizando la teoría de armónicos espaciales. Además, se diseña y construye un prototipo más sofisticado, que incluye desfasadores entre los elementos, con el objetivo de controlar el ángulo de apuntamiento de forma electrónica.

El Capítulo 4 estudia el concepto de un array log-periódico basado en el elemento strip-slot. Para ello, es necesario adaptar la metodología de diseño, concebida para elementos resonantes, y trasladarla al caso de elementos de banda ancha. La idea es comprobar si el hecho de utilizar un elemento adaptado en banda ancha introduce alguna mejora en el funcionamiento del array.

El Capítulo 5 aborda el diseño de un array que implementa la técnica de rotación secuencial con los elementos strip-slot para proporcionar agilidad en polarización. Además, como aplicación del concepto, se incluye la propuesta de una antena con capacidad diplexora para la recepción simultánea de dos bandas de navegación por satélite.

Finalmente, el Capítulo 6 resume los resultados más importantes y destaca las contribuciones más significativas derivadas de la tesis. Concluye con una propuesta de líneas futuras para continuar con este trabajo de investigación.

Adicionalmente se incluyen otros apéndices que completan los contenidos de la tesis. El Apéndice A recoge los resultados iniciales obtenidos cuando se empleó el elemento

strip-slot para construir LTs artificiales. El Apéndice B revisa las principales características de las redes en celosía y extrae una propiedad relevante sobre la independencia de la disipación de potencia en sus ramas. El Apéndice C incluye algunos resultados notables sobre las ventajas del modelado de discontinuidades y componentes de LT simétricos mediante redes en celosía. El Apéndice D incluye una breve descripción del teorema de Floquet y la expansión de armónicos espaciales. Finalmente, las publicaciones derivadas de este trabajo están enumeradas en el Apéndice E.

F.2 EL ELEMENTO STRIP-SLOT COMPLEMENTARIO

Se propone el elemento strip-slot complementario como una ranura alimentada por microstrip que consigue adaptación en banda muy ancha. Su geometría puede verse en la Fig. 2.1. Consiste en una sección acoplada strip-slot alimentada en serie por una línea microstrip terminada en carga adaptada. Dicha sección acoplada está compuesta por una tira de conductor (strip) y una ranura (slot) grabada en el plano de masa y colocada simétricamente a la tira. El plano de simetría que corta a la estructura longitudinalmente a la microstrip de alimentación divide el strip-slot en dos subsecciones acopladas idénticas. Cada una de ellas puede verse como una combinación microstrip-slotline, en la cual la slotline está terminada en cortocircuito y la microstrip, en circuito abierto. Por tanto, la estructura puede considerarse una ranura alimentada por microstrip convencional, a la que se le incorpora una strip o stub superpuesto a la ranura.

Las principales ventajas de la estructura son su simplicidad, que posee un único sustrato y que no necesita vías, lo que se traduce en bajo coste. Además, su alimentación en serie la hace muy apropiada para construir arrays de onda progresiva.

Si nos centramos en la subsección acoplada que hemos mencionado anteriormente, se puede observar que tiene tres conductores y un plano de simetría a lo largo de dicha sección. Por tanto, se propagan dos modos cuasi-TEM: el modo par y el modo impar. La distribución del campo eléctrico de ambos modos se muestra en la Fig. 2.2. Se concluye que el modo impar es similar al modo de la microstrip y, por tanto, viene determinado principalmente por la geometría del stub y el modo impar, es casi idéntico al modo de la slotline y depende de la geometría de la ranura. Además, se puede identificar la subsección acoplada strip-slot con la topología de líneas acopladas

dibujada en la Fig. 2.5. Esto permite obtener su matriz de impedancias y la impedancia imagen viene dada por la siguiente expresión:

$$Z_{im} = \sqrt{Z_e Z_o} = \sqrt{Z_{0e} Z_{0o} \cot \theta_e \tan \theta_o}, \quad (\text{F.1})$$

donde Z_{0e} y Z_{0o} son las impedancias características y θ_e y θ_o , las longitudes eléctricas de los modos par e impar, respectivamente. Resulta evidente que cuando $\theta_e = \theta_o$ la impedancia imagen se hace independiente de la frecuencia y, controlando el nivel de $\sqrt{Z_{0e} Z_{0o}}$, se obtendría adaptación en banda ancha.

El circuito equivalente propuesto para la subsección acoplada se muestra en la Fig. 2.7. Se trata de una red en celosía, en la que la rama serie viene determinada por el modo impar y la cruzada, por el par. Si se tienen en cuenta las relaciones de los modos par e impar con los de la strip y la ranura, respectivamente, el circuito equivalente que resulta para el elemento strip-slot (con planos de referencia coincidentes) es el que se muestra en la tercera columna de la Fig. 2.8. Se observa que la superposición del strip-slot se traduce en una combinación de sus circuitos equivalentes por separado formando una celosía: la rama serie presenta la impedancia de la ranura y la rama cruzada, la de la strip.

En cuanto a la radiación del elemento, se concluye que la strip no radia apreciablemente y que la radiación de la estructura proviene mayoritariamente de la ranura. Además, dicha radiación no se ve alterada por la presencia de la strip, por lo que el elemento se comporta en términos de radiación similar a una ranura convencional alimentada por microstrip. Cabe resaltar que el circuito equivalente en celosía también es capaz de explicar por qué la strip no afecta a las propiedades radiantes de la ranura: la potencia disipada en cada una de las ramas de una celosía simétrica (terminada en carga adaptada) es independiente de la impedancia que presente la otra rama.

Una vez analizado el elemento, la metodología de diseño para adaptación en banda ancha es inmediata. Se debe cumplir que las longitudes eléctricas de la ranura y del stub sean iguales y ajustar el nivel de impedancia a la impedancia de la microstrip de alimentación (Z_0):

$$\sqrt{\epsilon_{eff,M}} \cdot l_M = \sqrt{\epsilon_{eff,S}} \cdot l_S \quad (\text{F.2a})$$

$$\frac{1}{2} \sqrt{Z_M Z_S} = Z_0, \quad (\text{F.2b})$$

donde $\epsilon_{eff,M}$ y $\epsilon_{eff,S}$ representan las permitividades efectivas y Z_M y Z_S , las impedan-

cias características, de la strip y la ranura, respectivamente. Por tanto, la condición (F.2a) implica que la ranura y la strip deben ser complementarias (presentar la misma frecuencia de resonancia).

Se han construido dos prototipos en distintos sustratos para verificar la metodología de diseño (Figs. 2.10 y 2.11). Los resultados muestran que, efectivamente, esta estructura consigue eliminar el comportamiento resonante de la ranura (las Figs. 2.14 y 2.18 muestran las pérdidas de retorno para cada prototipo y la comparan con la correspondiente ranura sin el stub) y consigue un ancho de banda de impedancia de hasta 16:1. Además, se verifica que el circuito equivalente propuesto permite modelar la estructura de forma apropiada: en las Figs. 2.13 y 2.17 se representan las ramas del circuito equivalente para cada uno de los prototipos comparando las extraídas de la simulación y medidas con las teóricas. Asimismo, se corrobora que el diagrama de radiación del elemento strip-slot es prácticamente idéntico al de la ranura sin la strip (Fig. 2.22).

Finalmente, se ha realizado un estudio paramétrico para analizar cómo afectan los anchos de la strip y de la ranura en los parámetros de los modos par e impar, y, por tanto, en el comportamiento de la estructura. Se comparan cuatro diseños de adaptación en banda ancha con distintos anchos pero la mismas longitudes eléctricas. Se concluye que existen grados de libertad adicionales en la geometría, después de garantizar la adaptación, que pueden utilizarse para controlar la eficiencia de radiación del elemento (elementos radiantes más anchos radian mayor cantidad de potencia) o la no-linealidad del factor de fase. Por tanto, se pone de manifiesto la flexibilidad que permite la estructura propuesta a la hora de diseñar arrays sin comprometer el ancho de banda.

F.3 ARRAYS DE ONDA PROGRESIVA LINEALES BASADOS EN EL ELEMENTO STRIP-SLOT

Dada la alimentación en serie del strip-slot complementario, es inmediato construir un array de onda progresiva cargando la línea microstrip con varios elementos. La Fig. 3.1 muestra un prototipo fabricado con cinco elementos idénticos. De acuerdo a la teoría de armónicos espaciales, el array es capaz de hacer un escaneo en frecuencia desde atrás hacia adelante en dos bandas distintas. Los resultados corroboran esta predicción (Fig. 3.6), aunque también ponen de manifiesto una pequeña caída en la eficiencia de

radiación (Fig. 3.4) y una desadaptación (Fig. 3.5) en las frecuencias en las que la estructura radia en dirección broadside. Este fenómeno se conoce como *open-stopband* y es un problema clásico en este tipo de estructuras. No obstante, gracias a la buena adaptación del elemento, no resulta tan crítico en este caso. Además, se propone emplear el elemento ligeramente desalineado entre la strip y la ranura para mejorar el funcionamiento en broadside. En la Fig. 3.15 se presenta la comparación del $|S_{11}|$ medido del array con elementos alineados perfectamente y ligeramente desalineados, donde se observa que, con la versión desalineada, las desadaptaciones en broadside desaparecen. Por tanto, se consigue un array capaz de hacer escaneo del haz en frecuencia desde atrás hacia adelante, pasando por broadside, y en dos bandas distintas.

Con el objetivo de controlar electrónicamente el ángulo de apuntamiento, se realiza otro diseño de array lineal de onda progresiva incorporando desfasadores entre los elementos radiantes. Los desfasadores se implementan como tramos de LT cargados con varactores. El esquema de la antena se muestra en la Fig. 3.18. Se realiza un diseño que persigue cubrir una de las bandas de LTE (1.71-2.17 GHz) con el mayor rango de escaneo angular en todo el ancho de banda. Para conseguir este objetivo, se realiza una cuidadosa y razonada elección de las variables de diseño: distancia entre los elementos, número de celdas que forman el desfasador, geometría del elemento, etc. Finalmente, el prototipo resultante es el que se muestra en la Fig. 3.23. A diferencia de otras propuestas en la literatura, esta sencilla estructura es capaz de desempeñar dos funcionalidades distintas: apuntamiento electrónico con un amplio rango angular y mantenimiento del haz fijo en frecuencia. La Fig. 3.26 ilustra la funcionalidad del haz fijo en frecuencia, en la que las tensiones de los varactores se ajustan para que a cada frecuencia el haz apunte a -30° . Por otro lado, en la Fig. 3.27 se muestra el escaneo electrónico a la frecuencia de 2 GHz, donde se observa el amplio rango angular que es capaz de cubrir la estructura. Gracias a que el elemento del array no es resonante, la geometría de éste no ha de ser reconfigurada en frecuencia, lo que implica una ventaja sustancial con respecto a otros trabajos de la bibliografía. Además, dada la implementación en tecnología microstrip y la alimentación en serie, permite situar todos los componentes integrados en la misma capa y controlarlos a través de una señal de DC introducida por el puerto de RF.

F.4 ARRAY LOG-PERIÓDICO BASADO EN EL ELEMENTO STRIP-SLOT

Los arrays log-periódicos son antenas de banda ancha construidas a partir de elementos resonantes que siguen una progresión geométrica logarítmico-periódica (ver esquema en la Fig. 4.1). Aunque tradicionalmente se construían con dipolos, pronto se propusieron versiones planares que presentaban ventajas destacadas: menor coste de fabricación, facilidad de alimentación a través de una línea microstrip, etc. Sin embargo, puesto que los elementos radiantes planares son resonantes, la metodología de diseño empleada para estos arrays era la misma que para los arrays log-periódicos con dipolos. Sin embargo, el elemento complementario strip-slot es propio para construir este tipo de arrays de forma sencilla y además presenta adaptación de banda ancha, por lo que su uso en este tipo de antenas resulta de interés.

Teniendo en cuenta la naturaleza no-resonante del elemento strip-slot complementario, se ha reconsiderado la metodología de diseño para este tipo de arrays. Puesto que, además de estar adaptado en todo el ancho de banda, su eficiencia de radiación no es resonante, sino paso alto, el factor de escala entre elementos adyacentes puede ser más bajo que en los arrays clásicos. Esto implica que se puede cubrir el mismo ancho de banda con menos elementos, lo cual se puede traducir en una reducción de la longitud del array. En los arrays log-periódicos convencionales, este factor de escala tiene que ser muy próximo a la unidad para que el número de elementos que estén próximos a su frecuencia de resonancia (y, por tanto, capaces de radiar) sea el suficiente para garantizar buena eficiencia de radiación. Sin embargo, al utilizar elementos con eficiencias de radiación paso-alto, esto no plantea un problema. Además, la adaptación del array en banda ancha está asegurada, puesto que todos los elementos están adaptados en todo el ancho de banda de diseño. Esto no ocurre en los arrays clásicos, en los cuales es necesario introducir un desfase adicional de 180° entre elementos, para conseguir la cancelación de las reflexiones provenientes de los elementos que no están próximos a su frecuencia de resonancia y, por tanto, no están adaptados.

Para verificar las conclusiones extraídas anteriormente, se ha realizado un diseño con 15 elementos y un factor de escala bajo (0.909). El elemento más largo se ha elegido para que su ranura resuene a 2.3 GHz y el elemento más corto, a 8.6 GHz. Las ranuras siguen la progresión log-periódica mientras que las strips están diseñadas individualmente para que cada elemento esté adaptado en banda ancha. El prototipo resultante se muestra

en la Fig. 4.3. En la Fig. 4.4 se representa el coeficiente de onda estacionaria (VSWR) y se compara el medido y simulado cuando se termina el array en circuito abierto con respecto al obtenido cuando se termina en carga adaptada. Se observa que el array presenta buena adaptación en el ancho de banda de diseño y no se aprecian diferencias con respecto a la terminación en dicha banda de frecuencias, lo que indica que el array presenta una eficiencia de radiación alta y no llega prácticamente potencia a la carga. La Fig. 4.6 muestra los diagramas de radiación a distintas frecuencias. Se observa que el array mantiene razonablemente el apuntamiento en el ancho de banda de diseño. Los arrays log-periódicos de dipolos radian en dirección *backfire*; sin embargo, dado que el elemento presenta un nulo de radiación en esta dirección (debido al plano de masa), el array radia hacia atrás pero con un ángulo entorno a los -45° . Puesto que el elemento strip-slot radia hacia los dos semiespacios, se obtienen dos lóbulos. Uno de ellos se puede suprimir colocando un plano reflector inclinado a la distancia apropiada en una de las caras, como muestra la Fig. 4.12. Finalmente, se demuestra también que es posible estimar de forma teórica el diagrama de radiación utilizando el circuito equivalente del elemento y escalando debidamente las pérdidas de un elemento a otro, lo cual resulta interesante para reducir los costes computacionales a la hora del diseño.

F.5 ARRAY ROTADO SECUENCIALMENTE BASADO EN EL ELEMENTO STRIP-SLOT

El último concepto de antena que se analiza en esta tesis consiste en un array en forma de anillo que implementa la técnica de rotación secuencial [58] para obtener polarización circular con el elemento complementario strip-slot, el cual está linealmente polarizado. Esta técnica consiste en introducir un desfase entre elementos igual al ángulo de rotación geométrica: $\frac{360^\circ}{N}$, donde N es el número de elementos que forman el array. La alimentación en serie del elemento strip-slot permite implementarla de una forma muy sencilla mediante una línea microstrip circular, que, además, se puede terminar en dos puertos (Fig. 5.1). Esta última característica es importante, puesto que posibilita la generación de polarización tanto circular como lineal (cuando se alimenta el array simultáneamente por los dos puertos). Asimismo, la adaptación en banda ancha del elemento permite comportamiento multibanda, lo cual, añadido a la versatilidad en polarización y simplicidad, lo convierte en un array muy atractivo y competitivo, dada la dificultad de combinar ambas características en un único array pasivo.

El diseño se realiza con el objetivo de conseguir polarización circular (CP) en la/s banda/s deseada/s. Esto se lleva a cabo controlando el desfase entre elementos con el radio de la microstrip de alimentación y la geometría del strip-slot. Para un array de cuatro elementos, la condición para CP es la siguiente:

$$\phi_{total} = \phi_{\mu strip} + \phi_{elemento} = (2n + 1) \frac{\pi}{2}. \quad (F.3)$$

donde ϕ_{total} es el desfase entre elementos; $\phi_{\mu strip}$, el desfase introducido por los tramos de interconexión de línea microstrip; y $\phi_{elemento}$, el introducido por el elemento strip-slot con los planos de referencia coincidentes. Por tanto, todas las frecuencias en las que se cumpla la condición (F.3) son operativas, siempre que el elemento esté adaptado en dicha banda. Es por este motivo por el que el comportamiento multibanda es posible con el elemento strip-slot, dado su gran ancho de banda en impedancia.

Suponiendo tres bandas de funcionamiento, los modos de operación del array propuesto se muestran en las Tablas 5.1 y 5.2. Cuando la alimentación es por un solo puerto se obtiene CP con signo, a izquierdas (LHCP) o a derechas (RHCP), alternado entre bandas consecutivas. Además, por la cara de las ranuras se obtiene el signo de polarización contrario a la cara de las strips. Lo mismo ocurre cuando alimentamos por el otro puerto, que obtenemos las polarizaciones ortogonales. Cuando la alimentación es simultánea por los dos puertos, se consigue generar polarización lineal (LP). Dependiendo del desfase entre las excitaciones, la dirección de la polarización cambia. Por tanto, se pone de manifiesto la versatilidad en cuanto a polarización de este array.

Con el objetivo de demostrar el concepto, se ha diseñado y construido un prototipo (Fig. 5.3) que, de acuerdo a la teoría mencionada, debe operar alrededor de 6.2, 8.6 y 11.7 GHz. Se ha caracterizado tanto para CP (alimentación por un puerto) como para LP (alimentación simultánea por los dos puertos). Los resultados indican que se consigue una excelente adaptación en las bandas de operación (Fig. 5.4), una relación axial por debajo de 3 dB para CP (Fig. 5.5) y buena discriminación de polarización cruzada para LP (Fig 5.6). Además, se han medido los diagramas de radiación para ambas polarizaciones, corroborando que el array radia hacia la dirección de broadside con baja directividad (Figs. 5.7 y 5.10).

Dadas las numerosas posibilidades del array propuesto, se ha querido poner de manifiesto su potencial a través de una aplicación concreta. Con este propósito, se ha diseñado un nuevo prototipo (Fig. 5.16) para la recepción doble-banda de señales de sistemas globales de navegación por satélite (GNSS). El array resultante

es capaz de recibir dos bandas de radionavegación (1176-1207 MHz y 1563-1587 MHz) simultáneamente y diplexar ambas señales a través de sus dos puertos, sin necesidad de emplear componentes pasivos o activos adicionales.

F.6 CONCLUSIONES Y LÍNEAS FUTURAS

En esta tesis doctoral se ha estudiado una estructura planar radiante basada en el acoplamiento microstrip-slotline, que consigue un gran ancho de banda (hasta 16:1), a diferencia de los elementos radiantes en esta tecnología, cuya naturaleza resonante les hace ser de banda estrecha. Se trata de una ranura alimentada en serie por una línea microstrip, que se modifica introduciendo una strip superpuesta a la ranura y en la cara de la microstrip. Con esta sencilla modificación, se crea una sección acoplada que puede diseñarse para presentar un comportamiento paso-todo.

La alimentación en serie del elemento resulta excelente para construir arrays planares alimentados en serie, como los arrays de onda progresiva. Se han analizado en detalle tres conceptos de arrays que demuestran que la disponibilidad de un elemento radiante planar de banda ancha puede proporcionar funcionalidades mejoradas (por ejemplo, comportamiento multibanda) a las antenas en esta tecnología, con respecto a aquellas obtenidas con elementos clásicos resonantes.

Puesto que se ha caracterizado completamente el elemento strip-slot complementario y se han diseñado, fabricado y medido antenas basadas en este elemento con características atractivas que contribuyen al estado del arte, se puede afirmar que los objetivos marcados al inicio se han alcanzado con éxito: esta tesis ofrece una perspectiva nueva para las antenas planares, basadas en elementos no-resonantes. Aunque el strip-slot complementario se concibió inicialmente como celda unitaria para construir LTs artificiales, su aplicación más relevante se ha encontrado en el ámbito de las antenas. No obstante, se puede decir que los metamateriales han servido una vez más como fuente de inspiración para encontrar estructuras innovadoras.

F.6.1 Contribuciones originales

La contribución más importante de esta tesis es la propuesta del elemento strip-slot complementario como una ranura alimentada por microstrip de banda ancha, así como las herramientas teóricas que permiten explicar sus propiedades y establecer una meto-

dología de diseño. Especial mención merece también el circuito equivalente propuesto, puesto que ofrece una excelente comprensión del comportamiento físico de la estructura.

Es reseñable el trabajo relacionado con las redes en celosía. Se ha extraído una propiedad relevante sobre la independencia de las potencias disipadas en esta topología de circuito, que ha permitido explicar por qué la strip no altera las propiedades radiantes de la ranura. Además, esta red circuital se ha propuesto de una forma más general para el modelado de discontinuidades y componentes de LT simétricos, con la ventaja de garantizar la realizabilidad física de sus componentes, a diferencia de las ampliamente usadas redes en T o en Π .

En relación a las aplicaciones de antenas del elemento strip-slot complementario, cabe señalar que, si bien las topologías de array que se han explorado son clásicas, las estructuras resultantes son innovadoras, ya que están basadas en un elemento radiante planar novedoso adaptado en banda ancha, a diferencia de los arrays planares convencionales, que utilizan parches y/o ranuras, ambas resonantes. En el array de onda progresiva lineal se ha conseguido escaneo en frecuencia de atrás hacia delante (incluyendo broadside) en dos bandas distintas. Además, la incorporación de desfases entre los elementos ha puesto de manifiesto la capacidad de conseguir dos funcionalidades distintas en la misma estructura: variación del apuntamiento y mantenimiento del haz fijo, sobre una banda ancha de frecuencias, sin necesidad de modificar la geometría del elemento radiante gracias a su gran ancho de banda. Esta antena representa una contribución importante a las propuestas del estado del arte. En el array log-periódico, la reconsideración de la metodología de diseño clásica para elementos de banda ancha puede considerarse una aportación significativa, puesto que indica la posibilidad de reducción de tamaño (o anchos de banda mayores) cuando se utilizan elementos no-resonantes. Finalmente, la combinación de la antena circular de dos puertos y alimentación en serie con el elemento de banda ancha, en el array rotado secuencialmente, permite tanto agilidad en la polarización como comportamiento multibanda, sin la necesidad de componentes activos o pasivos adicionales. Como ejemplo de aplicación, se ha fabricado una antena novedosa para GNSS con capacidad diplexora y de doble banda.

F.6.2 Líneas futuras

Para continuar con este trabajo de investigación, se proponen las siguientes líneas de trabajo:

- **Reducir/evitar la radiación trasera**

Puesto que la radiación trasera representa un inconveniente para la mayoría de las aplicaciones de antenas, es importante conseguir que el elemento strip-slot radie sólo hacia un semiespacio sin perder eficiencia de radiación. A lo largo de la tesis, este problema se ha resuelto con la colocación de un plano reflector a la distancia apropiada. A pesar de que ésta es una posible solución, aumenta el tamaño de la estructura y es dependiente en frecuencia. La idea para mejorar esta limitación en el futuro consistiría en incorporar una capa metálica que apantallara la microstrip sin excitar otros modos indeseados, sobre todo el ancho de banda del elemento, lo cual no resulta trivial.

- **Strip-slot de formas arbitrarias**

En este trabajo se han empleado la strip y la ranura con forma rectangular porque era la geometría más simple para estudiar el comportamiento de la estructura. Sin embargo, sus atractivas propiedades no son únicas de esta geometría y se pueden explorar otras formas, que pueden proporcionar grados de libertad extra en el diseño.

- **Modelado de las pérdidas de radiación**

Para establecer la metodología de diseño del elemento strip-slot complementario, se han podido despreciar las pérdidas en el circuito equivalente. Sin embargo, en el estudio teórico de arrays, es esencial considerar las pérdidas por radiación. En la tesis, se han incluido en el circuito equivalente de una forma empírica, por lo que la búsqueda de un modelo teórico para las pérdidas requiere trabajo futuro.

- **Acoplamiento entre elementos**

Los efectos de acoplamiento entre elementos se han podido despreciar en los arrays propuestos y el diseño se ha realizado empleando el modelo de un elemento aislado. No obstante, si se desea reducir el espaciado entre elementos, será necesario incluir en el circuito equivalente el acoplamiento mutuo.

- **Circuito equivalente para el elemento strip-slot desalineado**

El desalineamiento entre la strip y la ranura introduce modificaciones en la

respuesta en frecuencia del elemento, que se han aprovechado para evitar el deterioro de las propiedades de radiación en broadside en los arrays lineales de onda progresiva. Para disponer de las herramientas de diseño apropiadas, sería interesante encontrar un circuito equivalente adecuado para el elemento strip-slot desalineado.

- **Modelado de otras estructuras mediante redes en celosía**

Aunque, en esta tesis, se ha investigado el modelado de otras estructuras con las redes en celosía, esta línea de trabajo tiene mucho más recorrido. Por ejemplo, la propiedad de la independencia de la potencia disipada se podría utilizar para identificar el origen de las pérdidas en otras estructuras, tal como se ha hecho con el strip-slot.

- **Implementación de otras topologías de arrays**

En este trabajo, se han analizado en detalle tres conceptos de arrays. No obstante, una línea de investigación posible puede centrarse en explorar otras topologías de arrays con el elemento strip-slot complementario.

BIBLIOGRAPHY

- [1] G. Kumar and K. P. Ray, *Broadband Microstrip Antennas*. Boston: Artech House, 2002.
- [2] W. K. L., *Compact and Broadband Microstrip Antennas*. New York: John Wiley & Sons, 2003.
- [3] V. Veselago, “The electrodynamics of substances with simultaneously negative values of ϵ and μ ,” *Soviet Physics Uspekhi*, vol. 10, no. 4, pp. 509 – 514, Jan. -Feb. 1968.
- [4] C. Caloz and T. Itoh, *Electromagnetic Metamaterials: Transmission Line Theory and Microwave Applications*. Hoboken, NJ: Wiley and IEEE Press, 2006.
- [5] L. Liu, C. Caloz, and T. Itoh, “Dominant mode leaky-wave antenna with backfire-to-endfire scanning capability,” *Electronics Letters*, vol. 38, no. 23, pp. 1414 – 1416, Nov. 2002.
- [6] F. Bongard and J. Mosig, “A novel composite right/left-handed unit cell and potential antenna applications,” in *IEEE Antennas and Propagation Society International Symposium*, Jul. 2008, pp. 1 –4.
- [7] F. Bongard, J. Perruisseau-Carrier, and J. Mosig, “Enhanced crlh transmission line performances using a lattice network unit cell,” *IEEE Microwave and Wireless Components Letters*, vol. 19, no. 7, pp. 431–433, July 2009.
- [8] M. Kahrizi, T. Sarkar, and Z. Maricevic, “Analysis of a wide radiating slot in the ground plane of a microstrip line,” *IEEE Transactions on Microwave Theory and Techniques*, vol. 41, no. 1, pp. 29 –37, Jan. 1993.
- [9] L. Zhu, R. Fu, and K.-L. Wu, “A novel broadband microstrip-fed wide slot antenna with double rejection zeros,” *IEEE Antennas and Wireless Propagation Letters*, vol. 2, no. 1, pp. 194 –196, 2003.

- [10] N. Behdad and K. Sarabandi, "A wide-band slot antenna design employing a fictitious short circuit concept," *IEEE Transactions on Antennas and Propagation*, vol. 53, no. 1, pp. 475 – 482, Jan. 2005.
- [11] A. Tulintseff, "Series-fed-type linear arrays of dipole and slot elements transversely coupled to a microstrip line," in *Antennas and Propagation Society International Symposium, 1993. AP-S. Digest*, 28 Jun.- 2 Jul. 1993, pp. 128 –131 vol.1.
- [12] M. A. Hanging, Q.-X. Chu, and Z. Qiuyi, "Novel shaped-beam microstrip slot array series fed by stepped-impedance line," *Microwave and Optical Technology Letters*, vol. 50, no. 9, pp. 2434 – 2437, Sep. 2008.
- [13] G. Elazar and M. Kisiuk, "Microstrip linear slot array antenna for X-band," *IEEE Transactions on Antennas and Propagation*, vol. 36, no. 8, pp. 1144 –1147, Aug. 1988.
- [14] H. Ogawa and M. Aikawa, "Analysis of coupled microstrip-slot lines," in *The Transactions of the IECE of Japan*, vol. E 62, no. 4, Apr. 1979, pp. 269 –270.
- [15] R. Hoffmann and J. Siegl, "Microstrip-slot coupler design-part i: S-parameters of uncompensated and compensated couplers," *IEEE Transactions on Microwave Theory and Techniques*, vol. 30, no. 8, pp. 1205 –1210, Aug. 1982.
- [16] E. Jones and J. T. Bolljahn, "Coupled-strip-transmission-line filters and directional couplers," *IRE Transactions on Microwave Theory and Techniques*, vol. 4, no. 2, pp. 75 –81, Apr. 1956.
- [17] J. E. Page, J. Esteban, and C. Camacho-Peñalosa, "Lattice equivalent circuits of transmission-line and coupled-line sections," *IEEE Transactions on Microwave Theory and Techniques*, vol. 59, no. 10, pp. 2422 –2430, Oct. 2011.
- [18] M. E. V. Valkenburg, *Introduction to Modern Network Synthesis*. New York: John Wiley & Sons, Inc., 1960.
- [19] A. Axelrod, M. Kisiuk, and J. Maoz, "Broadband microstrip-fed slot radiator," *Microwave Journal*, vol. 32, pp. 81 –94, Jun. 1989.
- [20] M. Himdi and J. Daniel, "Analysis of printed linear slot antenna using lossy transmission line model," *Electronics Letters*, vol. 28, no. 6, pp. 598–601, March 1992.

- [21] J. Ruyle and J. Bernhard, "A wideband transmission line model for a slot antenna," *IEEE Transactions on Antennas and Propagation*, vol. 61, no. 3, pp. 1407–1410, March 2013.
- [22] *High Frequency Structure Simulator (HFSS), version 12.1.2.*, ANSYS Inc., 2010.
- [23] *CST Studio Suite 2011.00*, Computer Simulation Technologies, 2011.
- [24] W. Menzel, "A new travelling wave antenna in microstrip," in *8th European Microwave Conference*, 1978, pp. 302–306.
- [25] A. Oliner and K. Lee, "Microstrip leaky wave strip antennas," in *Antennas and Propagation Society International Symposium*, vol. 24, June 1986, pp. 443–446.
- [26] A. Hessel, "Travelling-wave antennas," in *Antenna Theory*, R. E. Collin and F. J. Zucker, Eds. New York: McGraw-Hill, 1969, ch. 19.
- [27] D. Jackson, C. Caloz, and T. Itoh, "Leaky-wave antennas," *Proceedings of the IEEE*, vol. 100, no. 7, pp. 2194–2206, July 2012.
- [28] S. Paulotto, P. Baccarelli, F. Frezza, and D. Jackson, "A Novel Technique for Open-Stopband Suppression in 1-D Periodic Printed Leaky-Wave Antennas," *IEEE Transactions on Antennas and Propagation*, vol. 57, no. 7, pp. 1894–1906, July 2009.
- [29] S. Otto, A. Rennings, K. Solbach, and C. Caloz, "Transmission line modeling and asymptotic formulas for periodic leaky-wave antennas scanning through broadside," *IEEE Transactions on Antennas and Propagation*, vol. 59, no. 10, pp. 3695–3709, Oct 2011.
- [30] S. Otto, A. Al-Bassam, A. Rennings, K. Solbach, and C. Caloz, "Transversal asymmetry in periodic leaky-wave antennas for bloch impedance and radiation efficiency equalization through broadside," *IEEE Transactions on Antennas and Propagation*, vol. 62, no. 10, pp. 5037–5054, Oct 2014.
- [31] R. Miura, T. Tanaka, A. Horie, and Y. Karasawa, "A DBF self-beam steering array antenna for mobile satellite applications using beam-space maximal-ratio combination," *IEEE Transactions on Vehicular Technology*, vol. 48, no. 3, pp. 665–675, May 1999.

- [32] M. Ali, A. T. M. Sayem, and V. Kunda, "A Reconfigurable Stacked Microstrip Patch Antenna for Satellite and Terrestrial Links," *IEEE Transactions on Vehicular Technology*, vol. 56, no. 2, pp. 426–435, Mar. 2007.
- [33] A. Kulkarni and S. Sharma, "Frequency Reconfigurable Microstrip Loop Antenna Covering LTE Bands With MIMO Implementation and Wideband Microstrip Slot Antenna all for Portable Wireless DTV Media Player," *IEEE Transactions on Antennas and Propagation*, vol. 61, no. 2, pp. 964–968, Feb. 2013.
- [34] S.-J. Ha and C.-W. Jung, "Reconfigurable Beam Steering Using a Microstrip Patch Antenna With a U-Slot for Wearable Fabric Applications," *IEEE Antennas and Wireless Propagation Letters*, vol. 10, pp. 1228–1231, 2011.
- [35] E. Ojefors, S. Cheng, K. From, I. Skarin, P. Hallbjorner, and A. Rydberg, "Electrically Steerable Single-Layer Microstrip Traveling Wave Antenna With Varactor Diode Based Phase Shifters," *IEEE Transactions on Antennas and Propagation*, vol. 55, no. 9, pp. 2451–2460, Sep. 2007.
- [36] M. Abdalla, K. Phang, and G. Eleftheriades, "A Planar Electronically Steerable Patch Array Using Tunable PRI/NRI Phase Shifters," *IEEE Transactions on Microwave Theory and Techniques*, vol. 57, no. 3, pp. 531–541, Mar. 2009.
- [37] Y. Li, M. Iskander, Z. Zhang, and Z. Feng, "A New Low Cost Leaky Wave Coplanar Waveguide Continuous Transverse Stub Antenna Array Using Metamaterial-Based Phase Shifters for Beam Steering," *IEEE Transactions on Antennas and Propagation*, vol. 61, no. 7, pp. 3511–3518, Jul. 2013.
- [38] N. Yang, C. Caloz, and K. Wu, "Fixed-beam frequency-tunable phase-reversal coplanar stripline antenna array," *IEEE Transactions on Antennas and Propagation*, vol. 57, no. 3, pp. 671–681, Mar. 2009.
- [39] A. Nagra and R. York, "Distributed analog phase shifters with low insertion loss," *IEEE Transactions on Microwave Theory and Techniques*, vol. 47, no. 9, pp. 1705–1711, Sep. 1999.
- [40] D. M. Pozar, *Microwave Engineering (4th Edition)*. Wiley, 2011.
- [41] C. A. Balanis, *Antenna Theory: Analysis and Design, 3rd Ed.* John Wiley & Sons, Inc., 2005.

- [42] C. Yu, W. Hong, L. Chiu, G. Zhai, C. Yu, W. Qin, and Z. Kuai, "Ultrawideband printed log-periodic dipole antenna with multiple notched bands," *IEEE Transactions on Antennas and Propagation*, vol. 59, no. 3, pp. 725–732, March 2011.
- [43] M. Hamid, P. Hall, and P. Gardner, "Frequency reconfigurable log periodic patch array," *Electronics Letters*, vol. 46, no. 25, pp. 1648–1650, December 2010.
- [44] G. Zhai, Y. Cheng, D. Min, S. Zhu, and J. Gao, "Wideband simplified feed for printed log-periodic dipole array antenna," *Electronics Letters*, vol. 49, no. 23, pp. 1430–1432, Nov 2013.
- [45] H. Pues, J. Bogaers, R. Pieck, and A. van de Capelle, "Wideband quasi-log-periodic microstrip antenna," *Microwaves, Optics and Antennas, IEE Proceedings H*, vol. 128, no. 3, pp. 159–163, June 1981.
- [46] H. Smith and P. Mayes, "Log-periodic array of dual-feed microstrip patch antennas," *IEEE Transactions on Antennas and Propagation*, vol. 39, no. 12, pp. 1659–1664, Dec 1991.
- [47] H. Ozeki, S. Hayashi, N. Kikuma, and N. Inagaki, "Quasi-log-periodic microstrip antenna with closely coupled elements," *Electrical Engineering in Japan*, vol. 132, no. 2, pp. 58–64, 2000.
- [48] R. Carrel, "The design of log-periodic dipole antennas," in *IRE International Convention Record*, vol. 9, March 1961, pp. 61–75.
- [49] Q. Wu, R. Jin, and J. Geng, "A single-layer ultrawideband microstrip antenna," *IEEE Transactions on Antennas and Propagation*, vol. 58, no. 1, pp. 211–214, Jan 2010.
- [50] P. Hall, "New wideband microstrip antenna using log-periodic technique," *Electronics Letters*, vol. 16, no. 4, pp. 127–128, February 1980.
- [51] C. Balanis, *Antenna Theory: Analysis and Design. 3rd Edition*. New Jersey: John Wiley & Sons, Inc., 2005.
- [52] D. Isbell, "Log periodic dipole arrays," *IRE Transactions on Antennas and Propagation*, vol. 8, no. 3, pp. 260–267, May 1960.
- [53] R. Carrel, "Backward-wave radiation from periodic structures and application to the design of frequency independent antennas," in *Proceedings of IRE*, vol. 49, May 1961, pp. 962–963.

- [54] J. Yang and P.-S. Kildal, "Optimization of reflection coefficient of large log-periodic array by computing only a small part of it," *IEEE Transactions on Antennas and Propagation*, vol. 59, no. 6, pp. 1790–1797, June 2011.
- [55] A. Roederer, "A log-periodic cavity-backed slot array," *IEEE Transactions on Antennas and Propagation*, vol. 16, no. 6, pp. 756–758, Nov 1968.
- [56] S. Gao, A. Sambell, and S.-S. Zhong, "Polarization-agile antennas," *IEEE Antennas and Propagation Magazine*, vol. 48, no. 3, pp. 28–37, Jun. 2006.
- [57] D. Schaubert, F. Farrar, A. Sindoris, and S. Hayes, "Microstrip antennas with frequency agility and polarization diversity," *IEEE Transactions on Antennas and Propagation*, vol. 29, no. 1, pp. 118–123, Jan. 1981.
- [58] J. Huang, "A technique for an array to generate circular polarization with linearly polarized elements," *IEEE Transactions on Antennas and Propagation*, vol. 34, no. 9, pp. 1113–1124, Sep. 1986.
- [59] X. Zhao, L. Zhao, K. Huang, and C. Liu, "A circularly polarized array composed of linear polarized microstrip patches fed by metamaterial transmission line," *Journal of Electromagnetic Waves and Applications*, vol. 25, no. 11-12, pp. 1545–1553, 2011.
- [60] K. Bales and C. Meagher, "A planar reconfigurable polarization antenna," in *Antennas and Propagation Society International Symposium (APSURSI), 2013 IEEE*, Jul. 2013, pp. 1644–1645.
- [61] A. Abeygunasekera, M. Henry, and C. Free, "A novel radiation enhanced active antenna with switched dual circular polarization," in *European Microwave Conference, 2008*, Oct 2008, pp. 250–253.
- [62] A. Abeygunasekera and C. Free, "Active compact multilayer microstrip quadruple polarized antenna," in *Microwave Conference Proceedings (APMC), 2010 Asia-Pacific*, Dec. 2010, pp. 2068–2071.
- [63] P. H. Rao and V. Fusco, "Polarisation synthesis and beam tilting using a dual port circularly polarised travelling wave antenna array," *IEE Proceedings - Microwaves, Antennas and Propagation*, vol. 150, no. 5, pp. 321–324, Oct. 2003.

- [64] K.-F. Tong and J. Huang, “New Proximity Coupled Feeding Method for Reconfigurable Circularly Polarized Microstrip Ring Antennas,” *IEEE Transactions on Antennas and Propagation*, vol. 56, no. 7, pp. 1860–1866, Jul. 2008.
- [65] S.-S. Zhong, X.-X. Yang, and S.-C. Gao, “Polarization-agile microstrip antenna array using a single phase-shift circuit,” *IEEE Transactions on Antennas and Propagation*, vol. 52, no. 1, pp. 84–87, Jan 2004.
- [66] K. M. Lum, C. Laohapensaeng, and C. Free, “A novel traveling-wave feed technique for circularly polarized planar antennas,” *IEEE Microwave and Wireless Components Letters*, vol. 15, no. 3, pp. 180–182, Mar. 2005.
- [67] K. M. Lum, T. Tick, C. Free, and H. Jantunen, “Design and measurement data for a microwave dual-CP antenna using a new traveling-wave feed concept,” *IEEE Transactions on Microwave Theory and Techniques*, vol. 54, no. 6, pp. 2880–2886, Jun. 2006.
- [68] P.-Y. Qin, Y. Guo, and C. Ding, “A Dual-Band Polarization Reconfigurable Antenna for WLAN Systems,” *IEEE Transactions on Antennas and Propagation*, vol. 61, no. 11, pp. 5706–5713, Nov. 2013.
- [69] N. Jin, F. Yang, and Y. Rahmat-Samii, “A novel patch antenna with switchable slot (PASS): dual-frequency operation with reversed circular polarizations,” *IEEE Transactions on Antennas and Propagation*, vol. 54, no. 3, pp. 1031–1034, Mar. 2006.
- [70] C. Caloz, “Dual Composite Right/Left-Handed (D-CRLH) Transmission Line Metamaterial,” *IEEE Microwave and Wireless Components Letters*, vol. 16, no. 11, pp. 585–587, Nov. 2006.
- [71] A. Rennings, S. Otto, J. Mosig, C. Caloz, and I. Wolff, “Extended composite right/left-handed (E-CRLH) metamaterial and its application as quadband quarter-wavelength transmission line,” in *Asia-Pacific Microwave Conference. APMC 2006.*, Dec. 2006, pp. 1405–1408.
- [72] C. Camacho-Peñalosa, T. M. Martín-Guerrero, J. E. Page, and J. Esteban, “Derivation and General Properties of Artificial Lossless Balanced Composite Right/Left-Handed Transmission Lines of Arbitrary Order,” *Progress In Electromagnetics Research B*, vol. 13, pp. 151–169, 2009.

- [73] C. G. Montgomery, R. H. Dicke, and E. M. Purcell, *Principles of microwave circuits / edited by C.G. Montgomery, R.H. Dicke, E.M. Purcell*. Peter Peregrinus on behalf of the Institution of Electrical Engineers, London, U.K., 1987.
- [74] A. Barlett, *Theory of Electrical Artificial Lines and Filters*. John Wiley & Sons, 1930.
- [75] C.-I. Hsu and H. Auda, “On the realizability of the impedance matrix for lossy dielectric posts in a rectangular waveguide,” *IEEE Transactions on Microwave Theory and Techniques*, vol. 36, no. 4, pp. 763–765, April 1988.
- [76] K. Ise and M. Koshiha, “Equivalent circuits for dielectric posts in a rectangular waveguide,” *IEEE Transactions on Microwave Theory and Techniques*, vol. 37, no. 11, pp. 1823–1825, Nov 1989.
- [77] W.-H. Tu and K. Chang, “Microstrip elliptic-function low-pass filters using distributed elements or slotted ground structure,” *IEEE Transactions on Microwave Theory and Techniques*, vol. 54, no. 10, pp. 3786–3792, Oct 2006.
- [78] L.-H. Hsieh and K. Chang, “Compact elliptic-function low-pass filters using microstrip stepped-impedance hairpin resonators,” *IEEE Transactions on Microwave Theory and Techniques*, vol. 51, no. 1, pp. 193–199, Jan 2003.
- [79] R. E. Collin and F. J. Zucker, *Antenna Theory*. New York: McGraw-Hill, 1969.